

**This item is the archived peer-reviewed author-version of:**

Restructuring of titanium oxide overlayers over nickel nanoparticles during catalysis

**Reference:**

Monai Matteo, Jenkinson Kellie, Melcherts Angela E.M., Louwen Jaap N., Arslan Irmak Ece, Van Aert Sandra, Altantzis Thomas, Vogt Charlotte, van der Stam Ward, Duchon Tomas, ....- Restructuring of titanium oxide overlayers over nickel nanoparticles during catalysis  
Science / American Association for the Advancement of Science [Washington, D.C.]- ISSN 1095-9203 - 380:6645(2023), p. 644-651  
Full text (Publisher's DOI): <https://doi.org/10.1126/SCIENCE.ADF6984>  
To cite this reference: <https://hdl.handle.net/10067/1974320151162165141>

## **Title: Restructuring of titanium oxide overlayers over nickel nanoparticles during catalysis**

**Authors:** Matteo Monai<sup>1,†</sup>, Kellie Jenkinson<sup>2,†</sup>, Angela E. M. Melcherts<sup>1,†</sup>, Jaap N. Louwen<sup>1</sup>, Ece A. Irmak<sup>2</sup>, Sandra Van Aert<sup>2</sup>, Thomas Altantzis<sup>3</sup>, Charlotte Vogt<sup>1,‡</sup>, Ward van der Stam<sup>1</sup>, Tomáš Duchoň<sup>4</sup>, Břetislav Šmíd<sup>5</sup>, Esther Groeneveld<sup>6</sup>, Peter Berben<sup>6</sup>, Sara Bals<sup>2,\*</sup> and Bert M. Weckhuysen<sup>1,\*</sup>

### **Affiliations:**

<sup>1</sup>Inorganic Chemistry and Catalysis group, Institute for Sustainable and Circular Chemistry and Debye Institute for Nanomaterials Science, Utrecht University, Universiteitsweg 99, 3584 CG Utrecht, The Netherlands.

<sup>2</sup> EMAT and NANOLab Center of Excellence, University of Antwerp, 2020 Antwerp, Belgium

<sup>3</sup> ELCAT, University of Antwerp, 2610 Wilrijk, Belgium

<sup>4</sup>Peter-Grünberg-Institut 6, Forschungszentrum Jülich GmbH, 52425 Jülich, Germany

<sup>5</sup>Department of Surface and Plasma Science, Faculty of Mathematics and Physics, Charles University, V Holešovičkách 2, Prague 180 00, Czech Republic

<sup>6</sup>BASF Nederland B.V., Strijkviertel 61, 3454 PK De Meern, The Netherlands

<sup>†</sup> These authors contributed equally

<sup>‡</sup>Present address: *Schulich Faculty of Chemistry, Technion, Israel Institute of Technology, Technion City, Haifa 32000, Israel*

\*Corresponding authors: email: [Sara.Bals@uantwerpen.be](mailto:Sara.Bals@uantwerpen.be), [B.M.Weckhuysen@uu.nl](mailto:B.M.Weckhuysen@uu.nl)

**Abstract:** Reducible supports can affect the performance of metal catalysts by the formation of suboxide overlayers upon reduction, which is referred to as strong metal–support interaction (SMSI). A combination of operando electron microscopy and vibrational spectroscopy revealed that thin TiO<sub>x</sub> overlayers, formed on Ni/TiO<sub>2</sub> catalysts during 400 °Celsius reduction, were completely removed under CO<sub>2</sub> hydrogenation conditions. On the other hand, after 600 °Celsius reduction, exposure to CO<sub>2</sub> hydrogenation reaction conditions led to only partial re-exposure of Ni, forming interfacial sites in contact with TiO<sub>x</sub> and favoring carbon-carbon coupling by providing a carbon species reservoir. Our findings challenge the conventional understanding of SMSI, and call for more detailed operando investigations of nanocatalysts at single-particle level to revisit static models of structure-activity relationships.

**One-Sentence Summary:** Using multiscale operando techniques, we reveal that strong metal-support interaction in Ni/TiO<sub>2</sub> restructures under CO<sub>2</sub> hydrogenation conditions, leading to (partial) re-exposure and modification of active sites, and a performance that strongly depends on the reduction temperature.

**Main Text:**

Supported metal catalysts respond to pretreatment and reaction conditions by restructuring (1), phase changes (2), and chemical and structural oscillations (3), which can lead to catalyst activation, deactivation, or changes in selectivity. A striking example of catalyst restructuring is the so-called strong metal–support interaction (SMSI), in which metal nanoparticles (NPs) are encapsulated by overlayers of reducible supports, such as TiO<sub>2</sub>, after high-temperature reduction (4) or oxidation (5). SMSI can result in a drastic change in product selectivity (6), and has been correlated with high activity of mixed metal oxides in the oxygen evolution reaction (OER) (7), and with activation of industrial Cu/ZnO<sub>x</sub>/Al<sub>2</sub>O<sub>3</sub> catalysts (8).

Whereas there is substantial evidence for overlayer formation during catalyst pretreatments (9–11), including atomic resolution in-situ electron microscopy studies of overlayer formation under H<sub>2</sub> (10, 12–14), O<sub>2</sub> (5), and CO<sub>2</sub> environments (14), very little is known about the structure of the overlayer under reaction conditions. Recently, the complete removal of a TiO<sub>x</sub> ( $x \leq 2$ ) overlayer was shown for Pt/TiO<sub>2</sub> using in-situ transmission electron microscopy (TEM) under O<sub>2</sub>/H<sub>2</sub> mixtures at 600 °C (12). This result raises the question of whether overlayers persist during reaction conditions, or if the pretreatments used to induce SMSI are only indirectly affecting the catalyst performance, for example, by particle growth or phase changes, given that the geometric and electronic structure of pre-reduced catalysts can change dramatically under reaction conditions (15, 16). Multiscale operando methodologies (from single nanoparticle to ensemble level) are crucial to develop meaningful structure–performance relations for supported metal NPs. Recent advances in high-resolution

transmission electron microscopy methods allow to observe materials under operando conditions, at ambient pressure and high temperatures relevant to catalysis (*17–19*).

Here, we unravel the evolution of TiO<sub>x</sub> overlayers on industrially relevant Ni/TiO<sub>2</sub> catalysts during catalysis, for the CO and CO<sub>2</sub> hydrogenation reaction, after low (400 °C) and high (600 °C) temperature reduction. We combine quantitative operando scanning transmission electron microscopy (STEM) and infrared (IR) spectroscopy, near-ambient pressure x-ray photoelectron spectroscopy (NAP-XPS) and density functional theory (DFT) calculations to observe and understand overlayer restructuring and its effect on catalysis. The combination of both nano- and bulk-scale operando analytical techniques reveals information with unprecedented resolution on the single-atom level and also provides new insights into the properties of the ensemble of supported metal nanoparticles.

We show that TiO<sub>x</sub> overlayers, formed during reduction, restructure in CO<sub>2</sub>:H<sub>2</sub> mixtures at a temperature as low as 200 °C, (partially) re-exposing the Ni surface and introducing interfacial sites responsible for higher C–C coupling activity. We tailored suboxide overlayers to be stable under reaction conditions using different reduction pretreatment temperatures. This capability adds a parameter for catalyst optimization. These results could enable an understanding of the performance of a number of supported metals in reactions for sustainable technologies, such as biomass upgrading (*20*) and CO<sub>2</sub> valorization (*21, 22*).

Nickel partial encapsulation during 400 °C reduction

To induce oxide overlayer coverage by SMSI, and investigate its role in CO<sub>2</sub> hydrogenation, we reduced 6 wt.% Ni/TiO<sub>2</sub> catalysts at 400 °C (400-Ni/TiO<sub>2</sub>). The formation of TiO<sub>x</sub> overlayers upon the supported Ni nanoparticles (NPs) was investigated on a single-particle level by in-situ electron microscopy experiments in a windowed gas cell (climate G+, gas supply system, DENSsolutions) (Fig. 1A, and SI for experimental details). In-situ reduction of Ni/TiO<sub>2</sub> at 400 °C yielded supported metallic Ni NPs with an average diameter of 7.4 nm, and a size distribution of  $\pm 1.5$  nm standard deviation (Fig. 1B, Figs. S4 and S5) that were consistent with STEM and XRD observations after ex-situ reduction (Figs. S8 and S9 and Tables S1 and S2). The metallic state of the Ni NPs was confirmed by the Fourier transforms derived from the atomic-resolution high-angle annular dark-field scanning transmission electron microscopy (HAADF-STEM) images (Figs. S10 and S11).

A TiO<sub>x</sub> overlayer was detected on Ni NPs by in-situ HAADF-STEM imaging for 400-Ni/TiO<sub>2</sub> that corresponded to a partially encapsulating bilayer (Fig. 1 C, Figs. S12 and S13). This bilayer formed preferentially over (111) Ni surfaces for each of the five Ni NPs observed in a crystallographic zone axis, with no evidence of overlayer formation on other Ni facets (Figs. S12 and S13). As we aimed to investigate the catalyst dynamics in H<sub>2</sub> and during CO/CO<sub>2</sub> methanation conditions, it is important that structural changes observed are not an artefact of the electron beam. Therefore, we acquired multiple frames of the encapsulated Ni NP with low screen currents and fast image acquisition parameters to minimize potential electron beam induced artefacts(23). After applying neural network restoration of the HAADF-STEM data and frame averaging, we could estimate the positions of the atomic columns with high

accuracy and precision. We applied statistical parameter estimation theory to determine and refine the atomic column positions in the Ni NP and in the two atomic layers of Ti (illustrated in Fig. 1 D, Figs. S14-S16)(24). In addition, we applied the more advanced maximum a posteriori (MAP) probability rule to detect the Ti overlayer atomic columns that yield low contrast-to-noise ratio(25, 26).

Next, the displacements of all atomic columns with respect to the ideal atomic column positions in the Ni lattice were determined, from which we calculated a strain map (Fig. 1 D, Figs. S15 and S16). This quantitative analysis revealed an increase in tensile strain at the exposed (100) surface facet as expected from the increased mobility of surface adatoms. In contrast, both (111) facets covered by a TiO<sub>x</sub> bilayer displayed a small negative (compressive) strain over the surface and the second atomic subsurface layer as Ni accommodated the Ni-Ti interface. A compressive strain of Ni atoms at the TiO<sub>x</sub>/Ni(111) interface was also predicted by density functional theory (DFT) calculations for different TiO<sub>x</sub>/Ni models (Tables S3 and S4).

The interatomic Ti-Ti and Ni-Ti distances were measured using the atomic positions deduced by our statistics-based approaches and found to be  $2.95 \pm 0.01$  Å and  $2.93 \pm 0.09$  Å, respectively. Interestingly, the Ti-Ti distances showed a range of 2.77 to 2.95 Å for several measured particles using this technique (Fig. S17) and of the possible TiO<sub>x</sub> polymorphs, our measurements are in line with a compressed rutile (110) *d*-spacing (Fig. 1D, Fig. S10). This Ti-Ti distance is also consistent with continuous TiO<sub>x</sub> overlayers previously reported (13) and we anticipate that the observed compression is partially due to the discrete and minimal secondary

layer of Ti atoms that is too small to arrange perfectly as one expects for a bulk phase idealized crystal structure. The identity of the  $\text{TiO}_x$  overlayer was further distinguished from a  $\text{NiO}_x$  overlayer through in-situ electron energy-loss spectroscopy (EELS) analysis (Fig. S18). Interestingly, similar observations were made regardless of which crystal structure (rutile or anatase) the nickel nanoparticle resided on (Fig. S19).

To better understand our finding of the selective coverage of Ni(111) facets by bilayers of  $\text{TiO}_2$  rutile (110), we calculated the relative stability of  $\text{TiO}_2$  overlayers on the most observed Ni facets using DFT (Figs. S20 and S21). Based on the quantitative structural analysis of the atomic resolution in-situ HAADF-STEM data, we built  $\text{TiO}_2/\text{Ni}$  models using a Ni slab of 4 atomic layers oriented along the (111), (100), and (110) facets, covered by 2 monolayers of rutile (110) (see “Computational Details” in the SI for details). The lattice mismatch between the  $\text{TiO}_2$  rutile structure and the Ni surfaces would induce strain. After energy minimization, we found the strain energies for the Ni(111) and Ni(100) surfaces to be 0.5 and 3.1 kJ/(mole of  $\text{TiO}_2$ ), respectively. This difference was consistent with the distortion and irregularity of the modeled  $\text{TiO}_2$  overlayer on Ni(100) (Fig. 1E, Fig. S20). The lower energy toll calculated for the formation of  $\text{TiO}_2$  overlayers on Ni(111) thus explains the experimentally observed facet-selective coverage of Ni NPs.

To further investigate the structure of the  $\text{TiO}_x/\text{Ni}(111)$  interface, we used different configurations as input for computational calculations, varying the type and number of atoms between the interfacial Ni and  $\text{TiO}_x$  layers (Figs. S20 and S21). When the Ni surface was

covered with a TiO<sub>2</sub> rutile (110), the computed Ni–Ti interlayer distance was 3.20 Å, which is larger than what was experimentally observed (2.80–3.00 Å, Fig. 1E, top). On the other hand, a Ni–Ti distance of 2.79 Å was calculated for a partially reduced overlayer, where interfacial oxygen atoms were replaced by H atoms, and H<sup>+</sup> atoms were adsorbed on the Ni surface. Based on these calculations, the overlayers are most likely a suboxide phase.

Because in-situ HAADF-STEM imaging provided only local information on single NPs, we performed H<sub>2</sub> chemisorption to estimate the bulk, average percentage of exposed Ni surface for the ensemble of Ni NPs after the reduction of Ni/TiO<sub>2</sub> (Fig. S23). The amount of chemisorbed H<sub>2</sub> for 400-Ni/TiO<sub>2</sub> was 32 μmol/g, which corresponds to 6.7 % of the total amount of Ni atoms, or an apparent average NP size of 15 nm, assuming a 1:1 H:Ni stoichiometry. The apparent Ni NP size calculated from H<sub>2</sub> chemisorption was substantially larger than that measured with TEM (5.3 to 7.5 nm, Fig. 1B, Figs. S4, S5, and S7), indicating that part of the surface of Ni was blocked and not accessible to the gas phase. If no chemisorption took place on the TiO<sub>x</sub> overlayers, then there was a 25 to 46 % surface coverage of Ni by TiO<sub>x</sub> in 400-Ni/TiO<sub>2</sub>. This value is in agreement with the fraction of (111) Ni surface sites (35 to 57 %) predicted for Wulff-constructed Ni NPs of such sizes,<sup>(27)</sup> as well as with the in-situ HAADF-STEM evidence of selective encapsulation of (111) Ni facets.

#### Nickel re-exposure during CO<sub>2</sub> hydrogenation for Ni/TiO<sub>2</sub> after 400 °C reduction

We have followed changes in the TiO<sub>x</sub> overlayer under CO<sub>2</sub> hydrogenation reaction conditions by tracking a single Ni NP with HAADF-STEM while switching from H<sub>2</sub> to CO<sub>2</sub>:H<sub>2</sub>



at 400 °C and atmospheric pressure. Reactant and product gases from the windowed gas cell were tracked in real time during the reaction using mass spectrometry (MS) (Fig. 1H, Fig. S24). Upon introduction of the CO<sub>2</sub>:H<sub>2</sub> mixture, there was detectable formation of CH<sub>4</sub>, confirming that the catalyst actively performed CO<sub>2</sub> hydrogenation during observation within the electron microscope. As observed for other NPs (Figs. S12 and S13), the Ni NP in Fig. 1C developed a TiO<sub>x</sub> overlayer that selectively occupied Ni's (111) surface facets before hydrogenation.

Upon CO<sub>2</sub> exposure at 400 °C, the same Ni NP restructured and lost a large proportion of its highly faceted surface with only a small percentage of the (100) facet remaining, and exhibited an overall rounded morphology and retained its Ni metallic phase (Fig. 1F and Figs. S25 and S26). Comparative strain maps calculated for the same NP during CO<sub>2</sub> hydrogenation showed an increase in tensile strain over the entire NP surface in both x- and y- directions and a loss in compressive strain (Fig. 1G). We attributed these changes to the loss of the Ni-Ti interface during hydrogenation, which resulted in lower atomic coordination and higher mobility of surface atoms compared to its TiO<sub>2</sub>-encapsulated counterpart (400-Ni/TiO<sub>2</sub>, Fig. 1, C and D). The supported Ni catalyst dynamically evolved to express its more active facets during CO/CO<sub>2</sub> hydrogenation.<sup>(28)</sup> Thermodynamic calculations by the Gibbs free energy minimization method showed that TiO<sub>x</sub> became unstable under CO<sub>2</sub> hydrogenation conditions (Table S6, details in SI), which suggests that the removal of the TiO<sub>x</sub> overlayer was induced by changes in chemical potential, and not by the Ni NP restructuring.

To show that such removal of  $\text{TiO}_x$  overlayer upon exposure to  $\text{CO}_2$  hydrogenation conditions is representative of the bulk of the sample, we measured the attenuation of Ni 2p signal relatively to Ti 2p signals in NAP-XPS, which provided indirect evidence for encapsulation (Fig. S27). A fresh Ni/ $\text{TiO}_2$  catalyst was reduced at 400 °C in situ at 0.3 mbar  $\text{H}_2$ , and then exposed to cycles of 0.3 mbar  $\text{H}_2$  + 0.3 mbar  $\text{CO}_2$  and pure  $\text{H}_2$ . This sequence resulted in a reversible change of the Ni/Ti signal ratio that was consistent with the exposure and coverage of Ni under  $\text{CO}_2$  hydrogenation reaction conditions and  $\text{H}_2$ , respectively (Fig. S29, and SI for details).

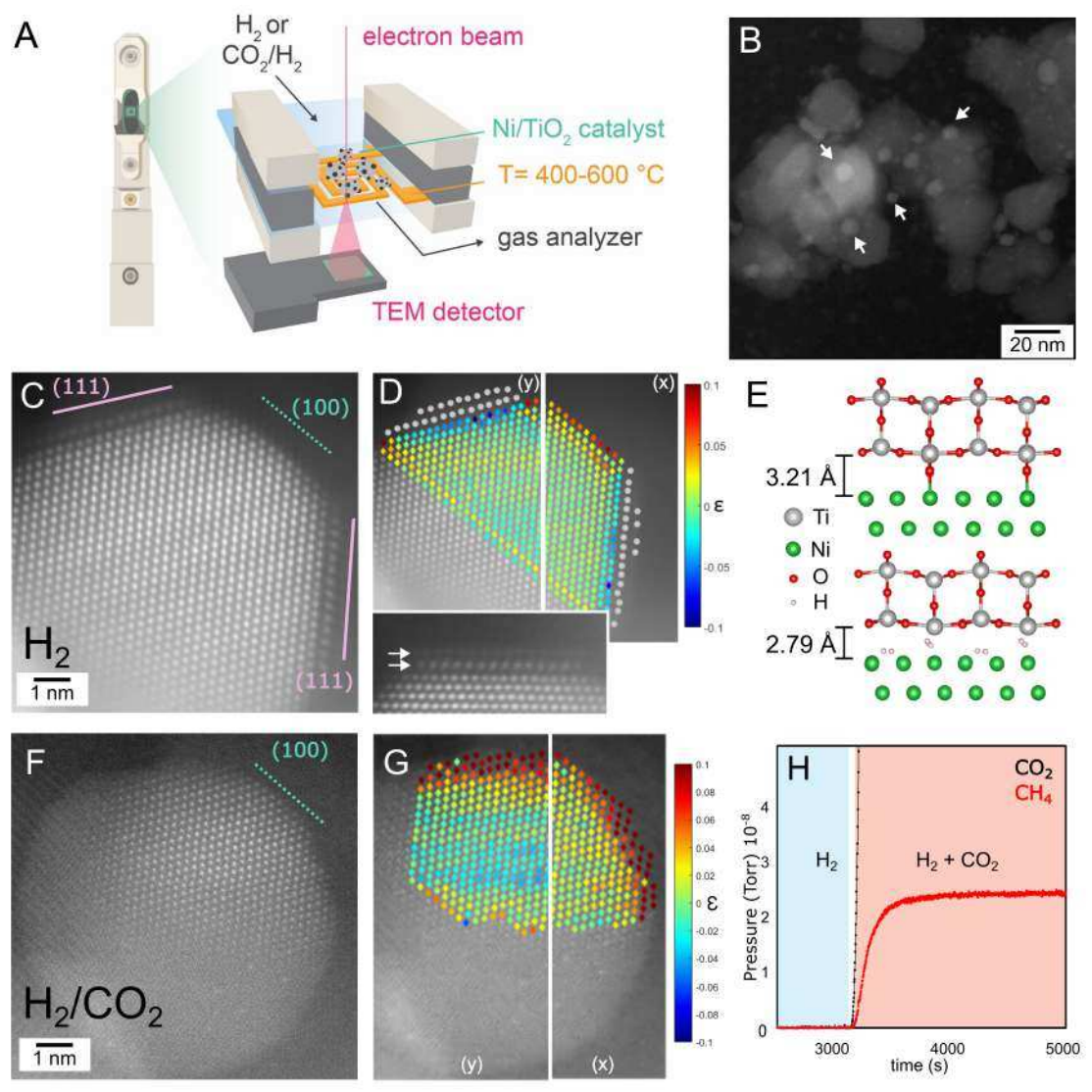


**Fig. 1. TiO<sub>x</sub> overlayer formation by low-temperature H<sub>2</sub> reduction and its restructuring during CO<sub>2</sub> methanation on a Ni/TiO<sub>2</sub> hydrogenation catalyst.** (A) Schematic of the operando electron microscopy setup and windowed gas cell (climate G+, DENSsolutions) used in this study. (B) High-angle annular dark-field scanning transmission electron microscopy (HAADF-STEM) overview image of a Ni/TiO<sub>2</sub> catalyst prepared in situ at 400 °C (400-Ni/TiO<sub>2</sub>), where white arrows highlight the Ni NPs upon the TiO<sub>2</sub> support. (C) A representative atomic resolution HAADF-STEM image of a Ni NP in a Ni/TiO<sub>2</sub> catalyst in H<sub>2</sub> at 400 °C. Solid lines indicate TiO<sub>x</sub>-covered Ni atomic planes and dashed lines indicate unoccupied facets. (111) and (100) facets are indicated by pink and green respectively. (D) Estimated positions of Ti (gray) and Ni (color scale) atomic columns. Ni atomic columns were identified through statistical parameter estimation theory and neural network image restoration whereas Ti atomic positions were identified using a combination of statistical parameter estimation theory and maximum a posteriori (MAP) probability rule due to Ti's limited visibility (25, 26). Strain maps (resulting from the displacements with respect to the ideal atomic column positions) in x and y directions. (inset) Close-up of the TiO<sub>x</sub> bilayer, where white arrows highlight each Ti layer. (E) Model of rutile TiO<sub>2</sub> (110) overlayer on a (111) Ni slab with oxygen (top) or hydrogen (bottom) atoms occupying the Ni – Ti interface calculated by density functional theory (DFT), suggesting that the titania overlayer is partially reduced at the interface. (F) HAADF-STEM image of the same particle as in (D) upon exposure to a CO<sub>2</sub>:H<sub>2</sub> (0.25 bar: 0.75 bar) mixture at 400 °C showing complete

re-exposure of Ni and NP restructuring. (G) Estimated atomic column positions of Ni (from the same particle shown in (F)) identified through statistical parameter estimation theory and neural network image restoration. Strain maps in x and y directions resulting from the displacements with respect to the ideal atomic column positions. (H) Mass spectrometry data measuring the partial pressure of CO<sub>2</sub> (black) and CH<sub>4</sub> (red) for the Ni/TiO<sub>2</sub> catalysts at 400°C. Regions highlighted in light blue and pink correspond to H<sub>2</sub> and CO<sub>2</sub>:H<sub>2</sub> environments, respectively.

### TiO<sub>x</sub> overlayer formation and restructuring for 600 °C reduced Ni/TiO<sub>2</sub>

With the aim to form a more stable TiO<sub>x</sub> overlayer, which would survive CO<sub>2</sub> hydrogenation conditions, we reduced the 6 wt.% Ni/TiO<sub>2</sub> catalyst in situ at 600 °C (600-Ni/TiO<sub>2</sub>). In comparison to the Ni/TiO<sub>2</sub> catalyst prepared at 400 °C (400-Ni/TiO<sub>2</sub>), the NP diameter approximately doubled to 14.0 nm ( $\pm$  4.0 nm size distribution) for the 600-Ni/TiO<sub>2</sub> (Fig. 2A and Figs. S6 and S7). The larger NP diameter is the result of the higher reduction temperature and is consistent with TEM and XRD observations after ex-situ reduction (Tables S1 and S2, Figs. S6-8). 600-Ni/TiO<sub>2</sub> displayed a completely encapsulating and relatively thick (1 to 2 nm) TiO<sub>x</sub> overlayer (Fig. 2B and Fig. S30). The greater degree of encapsulation occurred with the higher temperature treatment because the partial reduction of TiO<sub>2</sub> that is needed to form the TiO<sub>x</sub> overlayers is favored at higher temperatures (Figs. S2 and S3). Because of the lack of a single crystalline layer, atomic resolution HAADF-STEM was not applicable. Therefore, the formation of a TiO<sub>x</sub> overlayer was corroborated by in-situ EELS analysis, which showed a Ti L<sub>2,3</sub> ionization edge signal throughout the entire Ni NP (Fig. 2B-E and Figs. S31-33). Consistent with the complete encapsulation by TiO<sub>x</sub> observed by electron microscopy, H<sub>2</sub> chemisorption was almost completely suppressed for the 600-Ni/TiO<sub>2</sub> catalysts (Fig. S23).

After reduction, the in-situ prepared 600-Ni/TiO<sub>2</sub> catalyst was exposed to CO<sub>2</sub> hydrogenation reaction conditions at 400 °C. Similar to the 400-Ni/TiO<sub>2</sub>, CO<sub>2</sub> methanation was confirmed by tracking reactant and product gases by MS (Fig. 2F). Fig. 2G-I show the same Ni NP under H<sub>2</sub> (G) and under a CO<sub>2</sub>:H<sub>2</sub> mixture (H-I) at atmospheric pressure. The TiO<sub>x</sub>-suboxide overlayer was still visible but became more inhomogeneous after CO<sub>2</sub> exposure when compared to the pristine catalyst, indicating its partial degradation. Shell thickness measurements in Fig. 2, G to I, show the regions in which most changes in coverage were observed, with a circle identifying an area of the Ni surface that no longer appeared to be encapsulated by the overlayer (Fig. S34, see SI for experimental details).

Such overlayers survived even exposure to pure CO<sub>2</sub> at 400 °C (Fig. S34), in contrast to the easily removed TiO<sub>x</sub> bilayer observed for 400-Ni/TiO<sub>2</sub> catalysts. We hypothesize that the different stability is caused by the greater thickness of the shell, which contained sufficient Ti atoms to form stable patches of TiO<sub>x</sub> on Ni. Despite the extended encapsulation, the catalyst was active for the CO<sub>2</sub> hydrogenation reaction to methane, as shown by online MS analysis (Fig. 2F, Fig. S24).

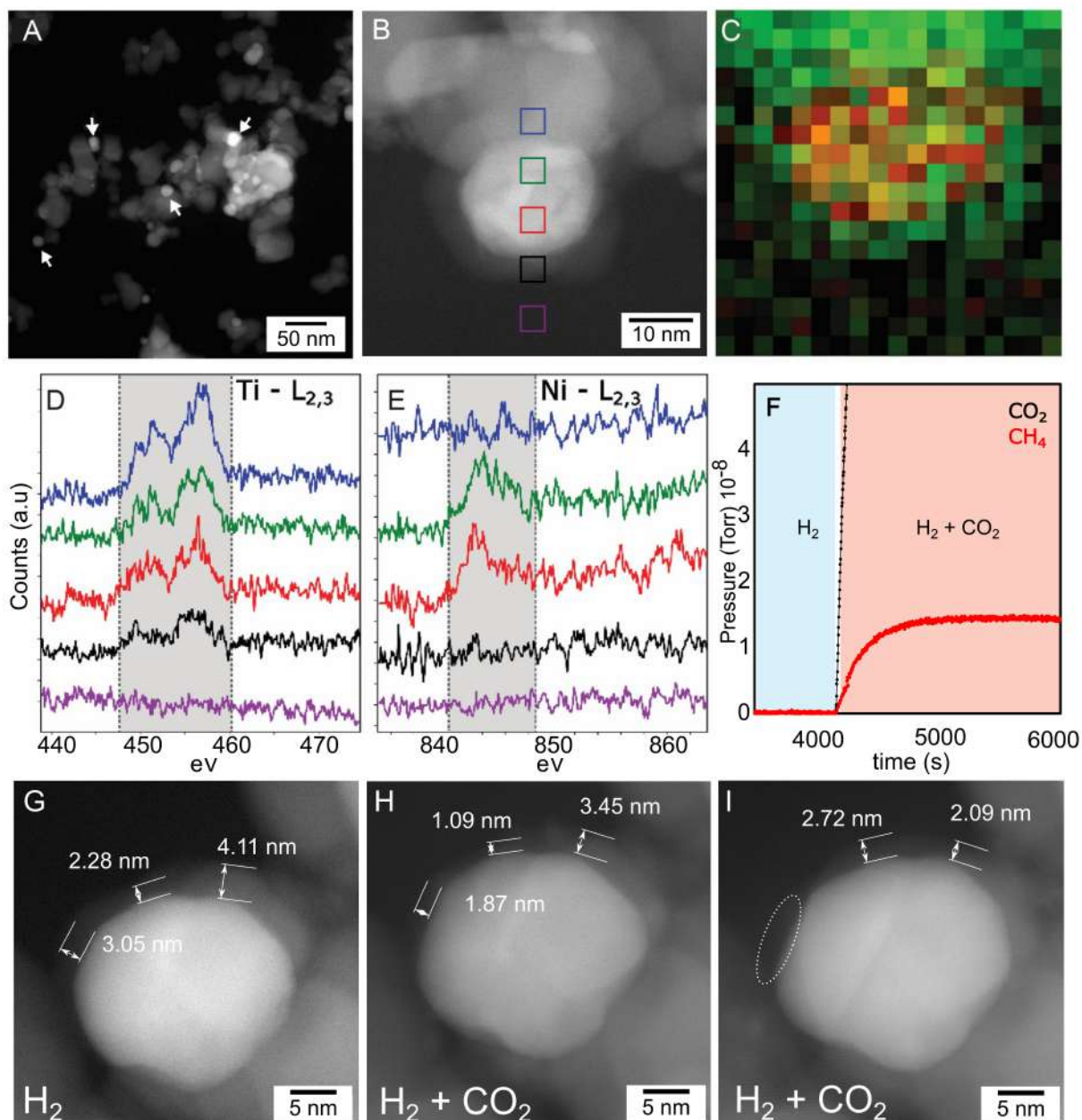


**Fig. 2. Formation of stable  $\text{TiO}_x/\text{Ni}$  overlayers during  $\text{CO}_2$  methanation on a  $\text{Ni}/\text{TiO}_2$  hydrogenation catalyst, first reduced at high temperature.** (A) HAADF-STEM overview images of  $\text{Ni}/\text{TiO}_2$  catalyst prepared in situ at  $600\text{ }^\circ\text{C}$  ( $600\text{-Ni}/\text{TiO}_2$ ), where white arrows highlight the Ni NPs upon the  $\text{TiO}_2$  support. (B) High-resolution HAADF-STEM image of  $\text{Ni}/\text{TiO}_2$  catalyst in  $\text{H}_2$  at  $600\text{ }^\circ\text{C}$ , showing a Ni NP encapsulated in a thick  $\text{TiO}_x$  shell. Colored squares correspond to the location where EELS spectra in panels D and E were acquired. (C) Core loss electron energy-loss spectroscopy (EELS) map of Ti  $L_{2,3}$  (green) and Ni  $L_{2,3}$  (red) ionization edges. (D) Core loss Ti  $L_{2,3}$  and (E) Ni  $L_{2,3}$  EELS spectra showing several regions of interests (ROIs) within the encapsulated NP, where spectrum color indicates the location of pixels shown in (B). (F) Mass spectrometry data acquired at  $400\text{ }^\circ\text{C}$ , showing the partial pressure of  $\text{CO}_2$  (black) and  $\text{CH}_4$  (red) for  $\text{Ni}/\text{TiO}_2$  catalysts prepared at  $600\text{ }^\circ\text{C}$ , with the regions highlighted in light blue and pink corresponding to  $\text{H}_2$  and  $\text{CO}_2:\text{H}_2$  environments, respectively. (G) High-resolution HAADF-STEM image of an individual Ni NP in  $\text{H}_2$  at  $600\text{ }^\circ\text{C}$  before  $\text{CO}_2$  hydrogenation. (H) High-resolution HAADF-STEM image of the same particle as in (G) upon exposure to a  $\text{CO}_2:\text{H}_2$  (0.25 bar  $\text{CO}_2$ : 0.75 bar  $\text{H}_2$ ) mixture at  $400\text{ }^\circ\text{C}$ .

°C showing only partial restructuring of the thick TiO<sub>x</sub> shell. (I) HAADF-STEM image of the same particle as G and H upon longer exposure to a CO<sub>2</sub>:H<sub>2</sub> (0.25 bar CO<sub>2</sub>: 0.75 bar H<sub>2</sub>) mixture at 400 °C, showing further restructuring of the thick TiO<sub>x</sub> shell and re-exposure of the Ni surface, highlighted by the white circle.

Our operando STEM results suggest that 600-Ni/TiO<sub>2</sub> remained predominantly encapsulated by TiO<sub>x</sub> under CO<sub>2</sub> hydrogenation reaction conditions. Therefore, we expected to observe an almost complete loss of activity for such catalyst in reactions promoted by Ni. However, both 400- and 600-Ni/TiO<sub>2</sub> catalysts were active for CO<sub>2</sub> hydrogenation during operando STEM experiments (Fig. 1H and 2F).

#### Comparison of catalytic performance

To investigate the effect of the residual TiO<sub>x</sub> overlayer on the catalytic CO/CO<sub>2</sub> hydrogenation performance of Ni/TiO<sub>2</sub> catalysts, we performed catalytic tests on 20 mg catalysts in operando FT-IR spectroscopy experiments under CO<sub>2</sub> hydrogenation conditions. These showed that both catalysts were active for CO<sub>2</sub> hydrogenation at 200 °C to 400 °C and 5 bar (Fig. 3A, Fig. S35-38), in agreement with operando TEM MS measurements. Compared to 400-Ni/TiO<sub>2</sub>, 600-Ni/TiO<sub>2</sub> showed a decrease in overall catalytic activity per g Ni, but a higher stability (Fig. 3A), and higher C<sub>2+</sub> selectivity (Figs. S36 and S37). All operando FT-IR spectroscopy and catalytic results reported herein were repeated on two separate batches of Ni/TiO<sub>2</sub> catalysts, showing comparable figures and trends (Figs. S45-S50).

The enhancement in C<sub>2+</sub> selectivity for the 600-Ni/TiO<sub>2</sub> catalyst became even more evident in CO/CO<sub>2</sub> co-hydrogenation experiments, with a C<sub>2+</sub> selectivity of 28 and 9 % for 600- and 400-Ni/TiO<sub>2</sub> catalysts respectively, at 300 °C and 5 bar pressure (Fig. 3, A to C). These results further

indicate that, under reaction conditions, the Ni surface in 600-Ni/TiO<sub>2</sub> was partially re-exposed, and that this affected the product selectivity of the reaction. Accordingly, ex-situ Ni 2p XPS spectra of the used 600-Ni/TiO<sub>2</sub> samples (after one reaction cycle, as in Fig. 3A), showed a higher Ni intensity than the reduced 600-Ni/TiO<sub>2</sub>, further supporting Ni re-exposure under reaction conditions (Fig. S27).

To provide direct evidence for the re-exposure of the Ni surface under reaction conditions and quantify the amount of exposed sites, we performed operando FT-IR spectroscopy experiments during CO/CO<sub>2</sub> co-hydrogenation (Fig. 3, D and E) and CO<sub>2</sub> hydrogenation (Fig. S38). The 400- and 600-Ni/TiO<sub>2</sub> catalysts showed similar CO<sub>x</sub> hydrogenation intermediate signals, with different relative intensities: CO<sub>(g)</sub> bands were observed in the region 2250-2100 cm<sup>-1</sup>, followed by relatively sharp bands at 2078 to 2062 cm<sup>-1</sup> (peak positions depended on temperature, see Figs. S40 and S41), which were ascribed to adsorbed sub-carbonyl Ni(CO)<sub>x</sub> (with x = 2,3) species (29-31). Ni(CO)<sub>4</sub> formation under the conditions of this study was ruled out by thermodynamic calculations (Table S7). A component corresponding to Ni-CO<sub>top</sub> was observed in the spectral region between 2060 and 2032 cm<sup>-1</sup>, while bridged CO (CO<sub>br.</sub>) adsorbed on Ni was observed in the spectral region between 1920 and 1940 cm<sup>-1</sup>. A series of bands at lower wavenumbers were ascribed to adsorbates on TiO<sub>2</sub>, as they are also present over the pure support (Fig. S42: adsorbed water peaks at 1616 cm<sup>-1</sup> (δ(OH))); formate (HCOO<sup>-</sup>) peaks at 1580 and 1375 cm<sup>-1</sup>; and carbonates (CO<sub>3</sub><sup>2-</sup>) peak at 1433 cm<sup>-1</sup> (32).



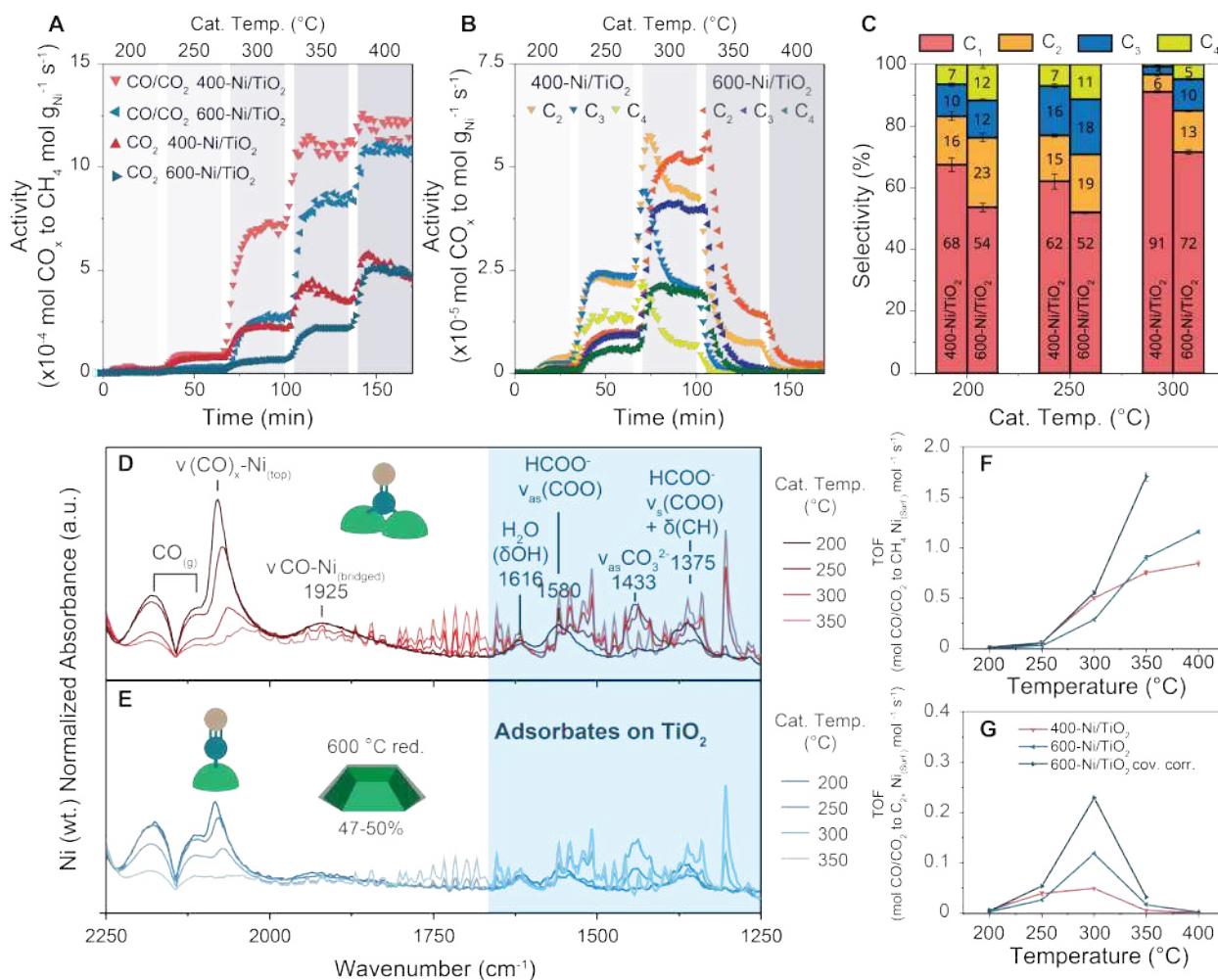


**Fig. 3. Ni/TiO<sub>2</sub> re-exposure under CO and CO<sub>2</sub> hydrogenation conditions revealed by operando vibrational spectroscopy.** (A) Catalytic activity of 400-Ni/TiO<sub>2</sub> (red) and 600-Ni/TiO<sub>2</sub> (blue), normalized per Ni g, for CO<sub>2</sub> (dark shade) and CO/CO<sub>2</sub> methanation (light shade). (B) C–C coupling activity of 400-Ni/TiO<sub>2</sub> and 600-Ni/TiO<sub>2</sub>, normalized per Ni g, during CO/CO<sub>2</sub> hydrogenation. (C) Selectivity to hydrocarbons in the CO/CO<sub>2</sub> hydrogenation reaction over 400-Ni/TiO<sub>2</sub> and 600-Ni/TiO<sub>2</sub>. (D and E) Operando FT-IR spectra collected at 200° to 300 °C under CO/CO<sub>2</sub> hydrogenation conditions over (D) 400-Ni/TiO<sub>2</sub> and (E) 600-Ni/TiO<sub>2</sub>, showing Ni exposure in both catalysts. The estimate for Ni coverage for 600-Ni/TiO<sub>2</sub> and the majority CO<sub>ads</sub> species at 300 °C is schematically depicted for the two catalysts (see SI for details). (F,G) Turnover frequency (TOF) for (F) methane production and (G) C–C coupling products over 400-Ni/TiO<sub>2</sub> (red) and 600-Ni/TiO<sub>2</sub> (light blue). The dashed dark blue line shows the TOF corrected for the most conservative estimate of exposed Ni surface in 600-Ni/TiO<sub>2</sub> (see SI for details). Conditions for CO<sub>2</sub> methanation: CO<sub>2</sub>:H<sub>2</sub>:He = 1:4:5, 5 bar, GHSV=80,000 h<sup>-1</sup>. Conditions for CO/CO<sub>2</sub> methanation: CO<sub>2</sub>:CO:H<sub>2</sub>:He = 3:1:7:9, 5 bar, GHSV=80,000 h<sup>-1</sup>.

Because the bands of adsorbed CO species (2078–1750 cm<sup>-1</sup>) were absent over pure TiO<sub>2</sub> under the same reaction conditions (Fig. S42), these spectral features were taken as a measure of the extent of Ni surface exposure under reaction conditions. Assuming complete re-exposure of 400-Ni/TiO<sub>2</sub> under reaction conditions, as evidenced by TEM (Fig. 1F, Fig. S26), the integration

of the CO bands for 400- and 600-Ni/TiO<sub>2</sub> reveals a TiO<sub>x</sub> coverage of ~ 50% for 600-Ni/TiO<sub>2</sub>, decreasing with increasing reaction temperature (Table S5). These results, combined with the STEM results shown in Fig. 2, G to I, provided evidence for a re-exposed Ni surface, partially covered by TiO<sub>x</sub> agglomerates that remained on the Ni NP surfaces.

Taking into account such a fraction of exposed Ni surface derived by operando FT-IR spectroscopy, we calculated an exposure-corrected turnover frequency (TOF) for methanation and C–C coupling (Fig. 3, F and G, Figs. S43 and S44, and TOF calculation subsection for details). Although the geometrical (i.e., not corrected by coverage) TOFs of 400- and 600-Ni/TiO<sub>2</sub> were comparable, the exposure-corrected TOFs of 600-Ni/TiO<sub>2</sub> were higher, indicating that the re-exposed Ni sites had a higher specific activity for both methanation and C–C coupling.

#### Mechanistic insights and structure sensitivity

Based on our results, we propose a model of the restructured Ni/TiO<sub>2</sub> catalysts under reaction conditions, to explain changes in surface chemistry, and, ultimately, in catalyst performance. The higher methanation TOF for 600-Ni/TiO<sub>2</sub> may be explained by a change in the majority of CO<sub>ads</sub> species, from less active, bridged CO<sub>ads</sub> for the 400-Ni/TiO<sub>2</sub> (Fig. 4, A and B) to more active, linear CO<sub>ads</sub> for 600-Ni/TiO<sub>2</sub> (Fig. 4, C and D, and Fig. S40B) (28). Because Ni NPs were larger in the 600-Ni/TiO<sub>2</sub> catalyst, and more extended Ni surfaces should result in more bridged CO<sub>ads</sub> (33), this observation can best be explained by the formation of a patchy TiO<sub>x</sub> overlayer that increased the extent of the Ni–TiO<sub>x</sub> interface and led to fewer available

sites for CO<sub>bridge</sub> formation, even on extended surfaces. Similarly, the enhancement in CO hydrogenation TOF on Pt/TiO<sub>2</sub> catalysts was explained by cooperative adsorption of CO at the interface, with the C atom coordinated to Pt and oxygen on the oxygen-deficient TiO<sub>x</sub>. (34). The formation of such structures was shown by the combination of operando FT-IR spectroscopy and HAADF-STEM results (Figs. 2 and 3). In the case of the 400-Ni/TiO<sub>2</sub>, the interface between Ni, TiO<sub>2</sub> and the gas phase is instead limited to the perimeter of the NP in contact with the support, because of the complete removal of the TiO<sub>x</sub> overlayers under reaction conditions.

The higher C–C coupling TOF for 600-Ni/TiO<sub>2</sub> was also in contrast with previous observations on Ni/SiO<sub>2</sub> catalysts, where C–C coupling was anticorrelated with methanation activity, because limited by the high hydrogenation rate of CH<sub>x</sub>\* (x=0–3) adsorbates on Ni. Both C–C coupling and methanation having higher TOF for 600-Ni/TiO<sub>2</sub> suggested that an alternative pathway was available for C–C coupling in the presence of a patchy TiO<sub>x</sub> overlayer. We propose that the increased Ni–TiO<sub>x</sub> interface aided C–C coupling by providing a reservoir of carbon species in close contact with adsorbates on Ni, and by stabilizing intermediates and transition states (Fig. 4D). Accordingly, calculations on TiO<sub>x</sub>/Ni catalysts showed that CO activation and CH–CH coupling were both more favorable at the interfacial Ni–TiO<sub>x</sub> sites (35). An alternative explanation for enhanced C–C coupling would involve reverse H-spillover from Ni to TiO<sub>x</sub>, hindering hydrogenation of CH<sub>x</sub>\* adsorbates by H\*. However, this mechanism is not consistent with the observed higher methanation TOF, which requires H\*. Ex-situ XRD showed no extended TiO<sub>2</sub> phase transformation, such as from anatase to rutile, at 600 °C (Fig.

S9), that could have affected the catalytic activity (36), although further studies are required to substantiate this explanation.

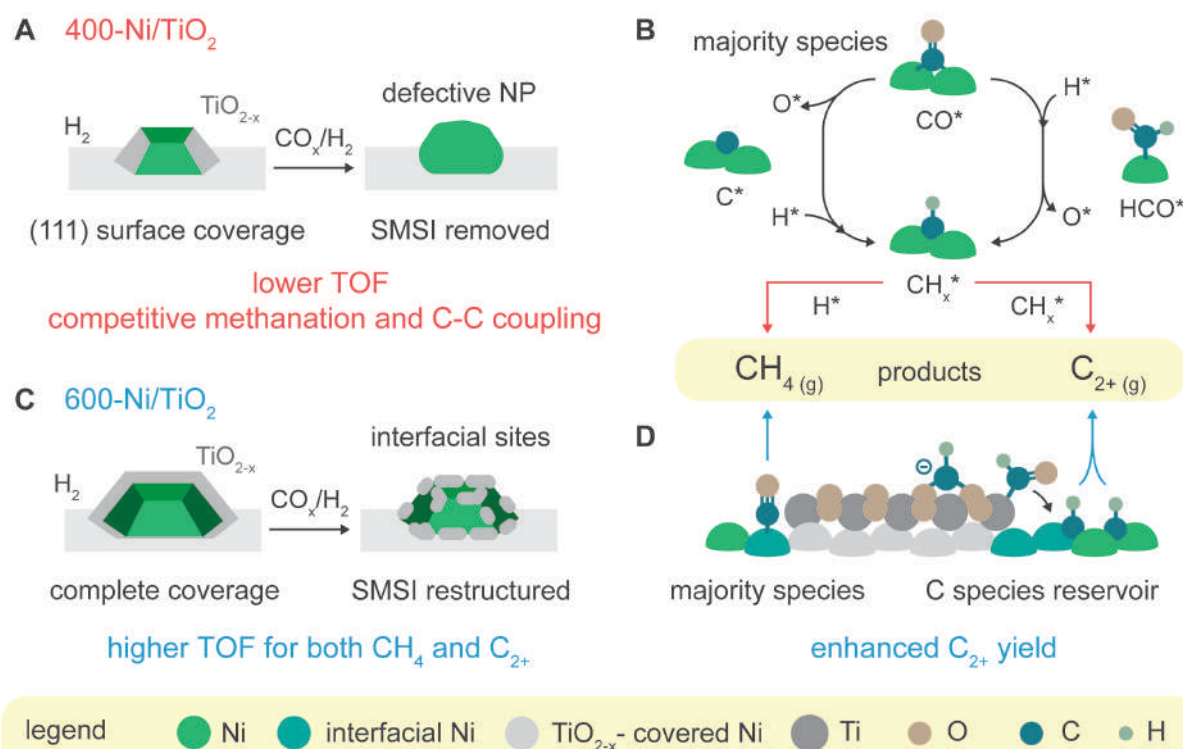


**Fig. 4. New understanding of Ni/TiO<sub>2</sub> catalyst performance and evolution during reduction and reaction.** Model for TiO<sub>x</sub> overlayer formation after 400 and 600 °C reduction and restructuring under reaction conditions, which explains the observed catalytic and spectroscopic results. (A) 400 °C reduction leads to the formation of a TiO<sub>x</sub> bilayer which is completely removed under reaction conditions, resulting in a defective particle. (B) For these particles, CO can adsorb on bridge sites (majority species). The adsorbed CO\* is converted to CH<sub>x</sub>\* via either HCO\* (H-assisted dissociation) or C\* (direct dissociation). This species is in turn converted to methane by hydrogenation (reaction with H\*) or to C-C coupling products (C<sub>2+</sub>) by reaction with CH<sub>x</sub>\* adsorbates. (C) 600 °C reduction leads to complete Ni coverage by TiO<sub>x</sub>, which restructures under reaction conditions. (D) On these particles, interfacial Ni-TiO<sub>x</sub> sites form upon which carbon species from the support are brought in contact with carbon species on Ni, favoring C-C coupling. Furthermore, CO is preferentially bound linearly, which explains the higher turnover frequency (TOF) per active site in the catalytic methanation of CO and CO<sub>2</sub>.

## Discussion

The observed restructuring of TiO<sub>x</sub> overlayer under reaction conditions was consistent with recent observations on Pt/TiO<sub>2</sub> by in-situ TEM during ROR cycles at 600 °C, in which

oxidative treatments cause amorphous TiO<sub>2</sub> islands to form, re-exposing part of the metal surface (10). Notably, CO/CO<sub>2</sub> hydrogenation conditions were sufficiently oxidative to shift the thermodynamic equilibrium to TiO<sub>2</sub> (Table S6). Our results show that, kinetically, a (partial) removal and restructuring of TiO<sub>x</sub> overlayers could occur even at temperatures as low as 200 °C, re-exposing the active Ni surface.

Both CO and CO<sub>2</sub> hydrogenations are structure sensitive reactions (33, 37), meaning that the TOF in the reactions changes as a function of NP size (38). Nonetheless, structure sensitivity only resulted in lower TOF for NPs with diameters below 2 to 4 nm, well below the range considered in this study (28, 37). Conversely, NPs with larger sizes have been reported to have similar, or even smaller, TOF, which would make the effect of SMSI in TOF enhancement even greater (33). Finally, C–C coupling was not strongly structure sensitive, according to theoretical calculations on Ni surfaces (28). Thus, the current observations that the TOF of both methanation and C–C coupling increase with Ni NP size could not possibly be explained by classical structure sensitivity concept, that is, only accounting for Ni surface sites variation with NP size (39). Similar deviations from classical structure sensitivity were observed for Co-based catalysts in CO<sub>2</sub> hydrogenation, where partially reduced cobalt oxide covered with metallic clusters of a few cobalt atoms showed substantially higher intrinsic activity due to interfacial effects (40).

In summary, we here directly observed for the first time the restructuring of metal oxide overlayers under operating conditions and rationalized their effects on the activity and

selectivity of Ni in CO-CO<sub>2</sub> hydrogenation reactions, depending on the reduction temperature. A similar, even if rudimentary, model of highly active interfacial sites was proposed by Burch et al. in the 1980s to explain the higher activity of Ni/TiO<sub>2</sub> when compared to Ni/SiO<sub>2</sub>, based on chemisorption results alone (41). Evidence that overlayers may be stabilized under reaction conditions was reported for Rh/TiO<sub>2</sub> catalysts, where pretreatments in CO<sub>2</sub>-rich atmospheres lead to the formation of a more persistent, “adsorbate-induced” SMSI (14). Recently, the enhancement of activity in methanol steam reforming reaction was also correlated with the amount of Cu-ZnO<sub>x</sub> interfacial sites (albeit observed ex situ), exhibiting faster kinetics for CH<sub>3</sub>O dehydrogenation and H<sub>2</sub>O dissociation (8). We now provide operando evidence for the formation of Ni-TiO<sub>x</sub> interfacial sites and show their effect on catalytic performance. A similar operando approach could be applied to understand many other chemical reactions in which the proximity of the active phase and support or promoters was found to be essential for higher activity or better selectivity, such as olefins production over Fe-based catalysts promoted by K (42), CO oxidation over Pd/CeO<sub>2</sub> (43) or propane dehydrogenation over Pt/Sn/CeO<sub>2</sub> (44). Crucial in this endeavor will be the simultaneous measurement of catalytic performance and the monitoring and control of the support, such as, crystal phase, porosity and exposed facets, and of the supported active phase nanostructure, such as NPs size, shape and composition.

## References and Notes

1. C. Vogt, F. Meirer, M. Monai, E. Groeneveld, D. Ferri, R. A. van Santen, M. Nachtegaal, R. R. Unocic, A. I. Frenkel, B. M. Weckhuysen, Dynamic restructuring of supported metal nanoparticles and its implications for structure insensitive catalysis. *Nat. Commun.* **12**, 7096 (2021). <https://doi.org/10.1038/s41467-021-27474-3>
2. A. V Puga, On the nature of active phases and sites in CO and CO<sub>2</sub> hydrogenation catalysts. *Catal. Sci. Technol.* **8**, 5681–5707 (2018). <https://doi.org/10.1039/C8CY01216D>

3. S. B. Vendelbo, C. F. Elkjær, H. Falsig, I. Puspitasari, P. Dona, L. Mele, B. Morana, B. J. Nelissen, R. Van Rijn, J. F. Creemer, P. J. Kooyman, S. Helveg, Visualization of oscillatory behaviour of Pt nanoparticles catalysing CO oxidation. *Nat. Mater.* **13**, 884–890 (2014). <https://doi.org/10.1038/nmat4033>
4. S. J. Tauster, S. C. Fung, R. L. Garten, Strong Metal-Support Interactions. Group 8 Noble Metals Supported on TiO<sub>2</sub>. *J. Am. Chem. Soc.* **100**, 170–175 (1978). <https://doi.org/10.1021/ja00469a029>
5. M. Tang, S. Li, S. Chen, Y. Ou, M. Hiroaki, W. Yuan, B. Zhu, H. Yang, Y. Gao, Z. Zhang, Y. Wang, Facet-Dependent Oxidative Strong Metal-Support Interactions of Palladium–TiO<sub>2</sub> Determined by In Situ Transmission Electron Microscopy. *Angew. Chem. Int. Ed.* **60**, 22339–22344 (2021). <https://doi.org/10.1002/anie.202106805>
6. C. Wu, L. Lin, J. Liu, J. Zhang, F. Zhang, T. Zhou, N. Rui, S. Yao, Y. Deng, F. Yang, W. Xu, J. Luo, Y. Zhao, B. Yan, X.-D. Wen, J. A. Rodriguez, D. Ma, Inverse ZrO<sub>2</sub>/Cu as a highly efficient methanol synthesis catalyst from CO<sub>2</sub> hydrogenation. *Nat. Commun.* **11**, 5767 (2020). <https://doi.org/10.1038/s41467-020-19634-8>
7. S. Samira, J. Hong, J. C. A. Camayang, K. Sun, A. S. Hoffman, S. R. Bare, E. Nikolla, Dynamic Surface Reconstruction Unifies the Electrocatalytic Oxygen Evolution Performance of Nonstoichiometric Mixed Metal Oxides. *JACS Au* **1**, 2224–2241 (2021). <https://doi.org/10.1021/jacsau.1c00359>
8. D. Li, F. Xu, X. Tang, S. Dai, T. Pu, X. Liu, P. Tian, F. Xuan, Z. Xu, I. E. Wachs, M. Zhu, Induced activation of the commercial Cu/ZnO/Al<sub>2</sub>O<sub>3</sub> catalyst for the steam reforming of methanol. *Nat Catal.* **5**, 99–108 (2022). <https://doi.org/10.1038/s41929-021-00729-4>
9. M. Macino, A. J. Barnes, S. M. Althahban, R. Qu, E. K. Gibson, D. J. Morgan, S. J. Freakley, N. Dimitratos, C. J. Kiely, X. Gao, A. M. Beale, D. Bethell, Q. He, M. Sankar, G. J. Hutchings, Tuning of catalytic sites in Pt/TiO<sub>2</sub> catalysts for the chemoselective hydrogenation of 3-nitrostyrene. *Nat. Catal.* **2**, 873–881 (2019). <https://doi.org/10.1038/s41929-019-0334-3>
10. A. Beck, X. Huang, L. Artiglia, M. Zabilskiy, X. Wang, P. Rzepka, D. Palagin, M. G. Willinger, J. A. van Bokhoven, The dynamics of overlayer formation on catalyst nanoparticles and strong metal-support interaction. *Nat. Commun.* **11**, 3220 (2020). <https://doi.org/10.1038/s41467-020-17070-2>
11. C. Hernández Mejía, T. W. van Deelen, K. P. de Jong, Activity enhancement of cobalt catalysts by tuning metal-support interactions. *Nat. Commun.* **9**, 4459 (2018). <https://doi.org/10.1038/s41467-018-06903-w>
12. H. Frey, A. Beck, X. Huang, J. A. van Bokhoven, M. G. Willinger, Dynamic interplay between metal nanoparticles and oxide support under redox conditions. *Science* **376**, 982–987 (2022). [10.1126/science.abm3371](https://doi.org/10.1126/science.abm3371)
13. S. Zhang, P. N. Plessow, J. J. Willis, S. Dai, M. Xu, G. W. Graham, M. Cargnello, F. Abild-Pedersen, X. Pan, Dynamical Observation and Detailed Description of Catalysts under Strong Metal–Support Interaction. *Nano Lett.* **16**, 4528–4534 (2016). <https://doi.org/10.1021/acs.nanolett.6b01769>
14. J. C. Matsubu, S. Zhang, L. DeRita, N. S. Marinkovic, J. G. Chen, G. W. Graham, X. Pan, P. Christopher, Adsorbate-mediated strong metal-support interactions in oxide-supported

- Rh catalysts. *Nat. Chem.* **9**, 120–127 (2017). <https://doi.org/10.1038/nchem.2607>
15. A. Bergmann, B. Roldan Cuenya, Operando Insights into Nanoparticle Transformations during Catalysis. *ACS Catal.* **9**, 10020–10043 (2019). <https://doi.org/10.1021/acscatal.9b01831>
  16. X. Zhang, S. Han, B. Zhu, G. Zhang, X. Li, Y. Gao, Z. Wu, B. Yang, Y. Liu, W. Baaziz, O. Ersen, M. Gu, J. T. Miller, W. Liu, Reversible loss of core–shell structure for Ni–Au bimetallic nanoparticles during CO<sub>2</sub> hydrogenation. *Nat. Catal.* **3**, 411–417 (2020). <https://doi.org/10.1038/s41929-020-0440-2>
  17. S. W. Chee, T. Lunkenbein, R. Schlögl, B. R. Cuenya, In situ and operando electron microscopy in heterogeneous catalysis—insights into multi-scale chemical dynamics. *J. Phys. Condens. Matter.* **33**, 153001 (2021). <https://doi.org/10.1088/1361-648X/abddfd>
  18. A. S. Kashin, V. P. Ananikov, Monitoring chemical reactions in liquid media using electron microscopy. *Nat. Rev. Chem.* **3**, 624–637 (2019). <https://doi.org/10.1038/s41570-019-0133-z>
  19. S. Hwang, X. Chen, G. Zhou, D. Su, In Situ Transmission Electron Microscopy on Energy-Related Catalysis. *Adv. Energy Mater.* **10**, 1902105 (2020). <https://doi.org/10.1002/aenm.201902105>
  20. X. Zhang, P. Yan, B. Zhao, K. Liu, M. C. Kung, H. H. Kung, S. Chen, Z. C. Zhang, Selective Hydrodeoxygenation of Guaiacol to Phenolics by Ni/Anatase TiO<sub>2</sub> Catalyst Formed by Cross-Surface Migration of Ni and TiO<sub>2</sub>. *ACS Catal.* **9**, 3551–3563 (2019). <https://doi.org/10.1021/acscatal.9b00400>
  21. A. Dokania, A. Ramirez, A. Bavykina, J. Gascon, Heterogeneous Catalysis for the Valorization of CO<sub>2</sub>: Role of Bifunctional Processes in the Production of Chemicals. *ACS Energy Lett.* **4**, 167–176 (2019). <https://doi.org/10.1021/acsenerylett.8b01910>
  22. M. Li, T. H. M. Pham, E. Oveisi, Y. Ko, W. Luo, A. Züttel, Revealing the Surface Chemistry for CO<sub>2</sub> Hydrogenation on Cu/CeO<sub>2-x</sub> Using Near-Ambient-Pressure X-ray Photoelectron Spectroscopy. *ACS Appl. Energy Mater.* **4**, 12326–12335 (2021). <https://doi.org/10.1021/acsaem.1c02146>
  23. T. Altantzis, I. Lobato, A. De Backer, A. Béché, Y. Zhang, S. Basak, M. Porcu, Q. Xu, A. Sánchez-Iglesias, L. M. Liz-Marzán, G. Van Tendeloo, S. Van Aert, S. Bals, Three-Dimensional Quantification of the Facet Evolution of Pt Nanoparticles in a Variable Gaseous Environment. *Nano Lett.* **19**, 477–481 (2019). <https://doi.org/10.1021/acs.nanolett.8b04303>
  24. A. De Backer, G. T. Martinez, A. Rosenauer, S. Van Aert, Atom counting in HAADF STEM using a statistical model-based approach: Methodology, possibilities, and inherent limitations. *Ultramicroscopy* **134**, 23–33 (2013). <https://doi.org/10.1016/j.ultramic.2013.05.003>
  25. J. Fatermans, S. Van Aert, A. J. den Dekker, The maximum a posteriori probability rule for atom column detection from HAADF STEM images. *Ultramicroscopy* **201**, 81–91 (2019). <https://doi.org/10.1016/j.ultramic.2019.02.003>
  26. J. Fatermans, A. J. den Dekker, K. Müller-Caspary, I. Lobato, C. M. O’Leary, P. D. Nellist, S. Van Aert, Single Atom Detection from Low Contrast-to-Noise Ratio Electron



- Microscopy Images. *Phys. Rev. Lett.* **121**, 056101 (2018).  
<https://doi.org/10.1103/PhysRevLett.121.056101>
27. E.B. Sterk, A.-E. Nieuwelink, M. Monai, J.N. Louwen, E.T.C. Vogt, I.A.W. Filot, B.M. Weckhuysen, Structure Sensitivity of CO<sub>2</sub> Conversion over Nickel Metal Nanoparticles Explained by Micro-Kinetics Simulations. *JACS Au* **2**, 2714-2730 (2022).  
<https://doi.org/10.1021/jacsau.2c00430>
  28. C. Vogt, M. Monai, E. B. Sterk, J. Palle, A. E. M. Melcherts, B. Zijlstra, E. Groeneveld, P. H. Berben, J. M. Boereboom, E. J. M. Hensen, F. Meirer, I. A. W. Filot, B. M. Weckhuysen, Understanding carbon dioxide activation and carbon-carbon coupling over nickel. *Nat. Commun.* **10**, 5330 (2019). <https://doi.org/10.1038/s41467-019-12858-3>
  29. K. Hadjiivanov, M. Mihaylov, D. Klissurski, P. Stefanov, N. Abadjieva, E. Vassileva, L. Mintchev, Characterization of Ni/SiO<sub>2</sub> Catalysts Prepared by Successive Deposition and Reduction of Ni<sup>2+</sup> Ions. *J. Catal.* **185**, 314–323 (1999).  
<https://doi.org/10.1006/jcat.1999.2521>
  30. M. Agnelli, H. M. Swaan, C. Marquez-Alvarez, G. A. Martin, C. Mirodatos, CO hydrogenation on a nickel catalyst: II. A mechanistic study by transient kinetics and infrared spectroscopy. *J. Catal.* **175**, 117–128 (1998).  
<https://doi.org/10.1006/jcat.1998.1978>
  31. C. Hernández Mejía, C. Vogt, B. M. Weckhuysen, K. P. de Jong, Stable niobia-supported nickel catalysts for the hydrogenation of carbon monoxide to hydrocarbons. *Catal. Today.* **343**, 56–62 (2020). <https://doi.org/10.1016/j.cattod.2018.11.036>
  32. A. Davydov, Molecular Spectroscopy of Oxide Catalyst Surfaces. John Wiley & Sons, Ltd, New York (2003) ISBN:9780471987314, doi:10.1002/0470867981
  33. C. Vogt, E. Groeneveld, G. Kamsma, M. Nachtegaal, L. Lu, C. J. Kiely, P. H. Berben, F. Meirer, B. M. Weckhuysen, Unravelling structure sensitivity in CO<sub>2</sub> hydrogenation over nickel. *Nat. Catal.* **1**, 127–134 (2018). <https://doi.org/10.1038/s41929-017-0016-y>
  34. B. Cornils, W. A. Herrmann, J.-H. Xu, H.-W. Zanthoff, Catalysis from A to Z: A Concise Encyclopedia, 5th Edition (Wiley, 2020). ISBN: 978-3-527-34311-9
  35. M. Xu, X. Qin, Y. Xu, X. Zhang, L. Zheng, J.-X. Liu, M. Wang, X. Liu, D. Ma, Boosting CO hydrogenation towards C<sub>2+</sub> hydrocarbons over interfacial TiO<sub>2-x</sub>/Ni catalysts. *Nat. Commun.* **13**, 6720 (2022). <https://doi.org/10.1038/s41467-022-34463-7>
  36. D. A. H. Hanaor, C. C. Sorrell, Review of the anatase to rutile phase transformation. *J. Mater. Sci.* **46**, 855–874 (2011). <https://doi.org/10.1007/s10853-010-5113-0>
  37. G. L. Bezemer, J. H. Bitter, H. P. C. E. Kuipers, H. Oosterbeek, J. E. Holewijn, X. Xu, F. Kapteijn, A. J. Van Dillen, K. P. De Jong, Cobalt particle size effects in the Fischer – Tropsch reaction studied with carbon nanofiber supported catalysts. *J. Am. Chem. Soc.* **128**, 3956–3964 (2006). <https://doi.org/10.1021/ja058282w>
  38. R. A. van Santen, Complementary structure sensitive and insensitive catalytic relationships. *Acc. Chem. Res.* **42**, 57–66 (2009). <https://doi.org/10.1021/ar800022m>
  39. C. Vogt, B.M. Weckhuysen, The concept of active site in heterogeneous catalysis. *Nat. Rev. Chem.* **6**, 89–111 (2022). <https://doi.org/10.1038/s41570-021-00340-y>

40. A. Parastaev, V. Muravev, E. H. Osta, T. F. Kimpel, J. F. M. Simons, A. J. F. van Hoof, E. Uslamin, L. Zhang, J. J. C. Struijs, D. B. Burueva, E. V. Pokochueva, K. V. Kovtunov, I. V. Koptuyug, I. J. Villar-Garcia, C. Escudero, T. Altantzis, P. Liu, A. Béch e, S. Bals, N. Kosinov, E. J. M. Hensen, Breaking structure sensitivity in CO<sub>2</sub> hydrogenation by tuning metal–oxide interfaces in supported cobalt nanoparticles. *Nat. Catal.* **5**, 1051–1060 (2022). <https://doi.org/10.1038/s41929-022-00874-4>
41. R. Burch, A. R. Flambard, Strong metal-support interactions in nickel/titania catalysts: The importance of interfacial phenomena. *J. Catal.* **78**, 389–405 (1982). [https://doi.org/10.1016/0021-9517\(82\)90322-0](https://doi.org/10.1016/0021-9517(82)90322-0)
42. Y. Han, C. Fang, X. Ji, J. Wei, Q. Ge, J. Sun, Interfacing with Carbonaceous Potassium Promoters Boosts Catalytic CO<sub>2</sub> Hydrogenation of Iron. *ACS Catal.* **10**, 12098–12108 (2020). <https://doi.org/10.1021/acscatal.0c03215>
43. M. Cargnello, V. V. T. Doan-Nguyen, T. R. Gordon, R. E. Diaz, E. A. Stach, R. J. Gorte, P. Fornasiero, C. B. Murray, Control of Metal Nanocrystal Size Reveals Metal-Support Interface Role for Ceria Catalysts. *Science* **341**, 771–773 (2013). DOI: 10.1126/science.1240148
44. H. Xiong, S. Lin, J. Goetze, P. Pletcher, H. Guo, L. Kovarik, K. Artyushkova, B. M. Weckhuysen, A. K. Datye, Thermally Stable and Regenerable Platinum–Tin Clusters for Propane Dehydrogenation Prepared by Atom Trapping on Ceria. *Angew. Chem. Int. Ed.* **56**, 8986–8991 (2017). <https://doi.org/10.1002/anie.201701115>
45. R. Burch, A. R. Flambard, Preparation of Titania-Supported Catalysts by Ion Exchange, Impregnation and Homogeneous Precipitation. *Studies in Surface Science and Catalysis* **16**, 311–322 (1983). [https://doi.org/10.1016/S0167-2991\(09\)60029-X](https://doi.org/10.1016/S0167-2991(09)60029-X)
46. L. Jones, P. D. Nellist, Identifying and Correcting Scan Noise and Drift in the Scanning Transmission Electron Microscope. *Microsc. Microanal.* **19**, 1050–1060 (2013). <https://doi.org/10.1017/S1431927613001402>
47. A. De Backer, K. H. W. van den Bos, W. Van den Broek, J. Sijbers, S. Van Aert, StatSTEM: An efficient approach for accurate and precise model-based quantification of atomic resolution electron microscopy images. *Ultramicroscopy* **171**, 104–116 (2016). <https://doi.org/10.1016/j.ultramic.2016.08.018>
48. B. Goris, J. De Beenhouwer, A. De Backer, D. Zanaga, K. J. Batenburg, A. Sánchez-Iglesias, L. M. Liz-Marzán, S. Van Aert, S. Bals, J. Sijbers, G. Van Tendeloo, Measuring Lattice Strain in Three Dimensions through Electron Microscopy. *Nano Lett.* **15**, 6996–7001 (2015). <https://doi.org/10.1021/acs.nanolett.5b03008>
49. T. D. Kühne, M. Iannuzzi, M. Del Ben, V. V. Rybkin, P. Seewald, F. Stein, T. Laino, R. Z. Khaliullin, O. Schütt, F. Schiffmann, D. Golze, J. Wilhelm, S. Chulkov, M. H. Bani-Hashemian, V. Weber, U. Borštnik, M. Taillefumier, A. S. Jakobovits, A. Lazzaro, H. Pabst, T. Müller, R. Schade, M. Guidon, S. Andermatt, N. Holmberg, G. K. Schenter, A. Hehn, A. Bussy, F. Belleflamme, G. Tabacchi, A. Glö , M. Lass, I. Bethune, C. J. Mundy, C. Plessl, M. Watkins, J. VandeVondele, M. Krack, J. Hutter, CP2K: An electronic structure and molecular dynamics software package - Quickstep: Efficient and accurate electronic structure calculations. *J. Chem. Phys.* **152**, 194103 (2020). <https://doi.org/10.1063/5.0007045>

50. G. Lippert, J. Hutter, M. Parrinello, A hybrid Gaussian and plane wave density functional scheme. *Mol. Phys.* **92**, 477–488 (1997). <https://doi.org/10.1080/002689797170220>
51. J. VandeVondele, M. Krack, F. Mohamed, M. Parrinello, T. Chassaing, J. Hutter, Quickstep: Fast and accurate density functional calculations using a mixed Gaussian and plane waves approach. *Comput. Phys. Commun.* **167**, 103–128 (2005). <https://doi.org/10.1016/j.cpc.2004.12.014>
52. J. P. Perdew, K. Burke, M. Ernzerhof, Generalized gradient approximation made simple. *Phys. Rev. Lett.* **77**, 3865–3868 (1996). <https://doi.org/10.1103/PhysRevLett.77.3865>
53. S. Grimme, J. Antony, S. Ehrlich, H. Krieg, A consistent and accurate ab initio parametrization of density functional dispersion correction (DFT-D) for the 94 elements H-Pu. *J. Chem. Phys.* **132**, 154104 (2010). <https://doi.org/10.1063/1.3382344>
54. S. Grimme, S. Ehrlich, L. Goerigk, Effect of the damping function in dispersion corrected density functional theory. *J. Comput. Chem.* **32**, 1456–1465 (2011). <https://doi.org/10.1002/jcc.21759>
55. J. VandeVondele, J. Hutter, Gaussian basis sets for accurate calculations on molecular systems in gas and condensed phases. *J. Chem. Phys.* **127**, 114105 (2007). <https://doi.org/10.1063/1.2770708>
56. S. Goedecker, M. Teter, J. Hutter, Separable dual-space Gaussian pseudopotentials. *Phys. Rev. B* **54**, 1703–1710 (1996). <https://doi.org/10.1103/PhysRevB.54.1703>
57. C. Hartwigsen, S. Goedecker, J. Hutter, Relativistic separable dual-space Gaussian pseudopotentials from H to Rn. *Phys. Rev. B* **58**, 3641–3662 (1998). <https://doi.org/10.1103/PhysRevB.58.3641>
58. H. J. Monkhorst, J. D. Pack, Special points for Brillouin-zone integrations. *Phys. Rev. B* **13**, 5188–5192 (1976). <https://journals.aps.org/prb/abstract/10.1103/PhysRevB.13.5188>
59. C. Arrouvel, M. Digne, M. Breyse, H. Toulhoat, P. Raybaud, Effects of morphology on surface hydroxyl concentration: a DFT comparison of anatase–TiO<sub>2</sub> and  $\gamma$ -alumina catalytic supports. *J. Catal.* **222**, 152–166 (2004). <https://doi.org/10.1016/j.jcat.2003.10.016>
60. R. W. G. Wyckoff, *Crystal Structures – Volume 1*. Interscience Publishers (1963) <https://books.google.nl/books?id=40uGpwAACAAJ>
61. C. J. Howard, T. M. Sabine, F. Dickson, Structural and thermal parameters for rutile and anatase. *Acta Cryst. B* **47**, 462–468 (1991). <https://doi.org/10.1107/S010876819100335X>
62. V. Bratan, C. Munteanu, C. Hornoiu, A. Vasile, F. Papa, R. State, S. Preda, D. Culita, N. I. Ionescu, CO oxidation over Pd supported catalysts —In situ study of the electric and catalytic properties. *Appl. Catal. B Environ.* **207**, 166–173 (2017). <https://doi.org/10.1016/j.apcatb.2017.02.017>
63. P. Munnik, M. E. Z. Velthoen, P. E. de Jongh, K. P. De Jong, C. J. Gommers, Nanoparticle growth in supported nickel catalysts during methanation reaction—larger is better. *Angew. Chem. Int. Ed.* **53**, 9493–9497 (2014). <https://doi.org/10.1002/ange.201404103>
64. U. Holzwarth, N. Gibson, The Scherrer equation versus the “Debye-Scherrer equation”. *Nat. Nanotechnol.* **6**, 534 (2011). <https://doi.org/10.1038/nnano.2011.145>

65. J. Végh, The analytical form of the Shirley-type background. *J. Electron Spectros. Relat. Phenomena* **46**, 411–417 (1988). [https://doi.org/10.1016/0368-2048\(88\)85038-2](https://doi.org/10.1016/0368-2048(88)85038-2)
66. A. Herrera-Gomez, M. Bravo-Sanchez, F. S. Aguirre-Tostado, M. O. Vazquez-Lepe, The slope-background for the near-peak regimen of photoemission spectra. *J. Electron Spectros. Relat. Phenomena* **189**, 76–80 (2013). <https://doi.org/10.1016/j.elspec.2013.07.006>
67. A. B. McLean, C. E. J. Mitchell, D. M. Swanston, Implementation of an efficient analytical approximation to the Voigt function for photoemission lineshape analysis. *J. Electron Spectros. Relat. Phenomena* **69**, 125–132 (1994). [https://doi.org/10.1016/0368-2048\(94\)02189-7](https://doi.org/10.1016/0368-2048(94)02189-7)
68. W. Smekal, W. S. M. Werner, C. J. Powell, Simulation of electron spectra for surface analysis (SESSA): A novel software tool for quantitative Auger-electron spectroscopy and X-ray photoelectron spectroscopy. *Surf. Interface Anal.* **37**, 1059–1067 (2005). <https://doi.org/10.1002/sia.2097>
69. M. Mihaylov, K. Hadjiivanov, H. Knözinger, Formation of Ni(CO)<sub>4</sub> during the interaction between CO and silica-supported nickel catalyst: An FTIR spectroscopic study. *Catal. Letters* **76**, 59–63 (2001). <https://doi.org/10.1023/A:1016786023456>
70. J. C. Campuzano, R. G. Greenler, The adsorption sites of CO on Ni(111) as determined by infrared reflection - absorption spectroscopy. *Surf. Sci.* **83**, 301–312 (1979). [https://doi.org/10.1016/0039-6028\(79\)90495-3](https://doi.org/10.1016/0039-6028(79)90495-3)
71. M. Bradley, *Curve Fitting in Raman and IR Spectroscopy: Basic Theory of Line Shapes and Applications* (2007), Thermo Fisher Scientific, Madison, WI, USA, application note 50733
72. L. Mino, G. Spoto, A. M. Ferrari, CO<sub>2</sub> Capture by TiO<sub>2</sub> Anatase Surfaces: A Combined DFT and FTIR Study. *J. Phys. Chem. C* **118**, 25016–25026 (2014). <https://doi.org/10.1021/jp507443k>

**Acknowledgments:** BMW thanks NWO for a CHIPP Research Grant, Gravitation Program (Netherlands Center for Multiscale Catalytic Energy Conversion (MCEC)) and Advanced Research Center Chemical Building Blocks Consortium (ARC CBBC) grants. Savannah Turner (Utrecht University, UU) is acknowledged for performing the STEM measurements, Luc Smulders (UU) for H<sub>2</sub> chemisorption experiments, Carlos Hernández Mejía (UU) for performing the TPR-TPO experiments, and Justine Harmel (UU) and Kang Cheng (UU) for performing the H<sub>2</sub> chemisorption measurements. This work made use of the Dutch national e-infrastructure with the support of the SURF Cooperative using grant no. EINF-2959.

**Funding:**

BASF and NWO CHIPP research grant to B.M.W.

MCEC NWO Gravitation Program to B.M.W.

ARC-CBBC NWO Program to B.M.W.

European Research Council Grant 770887 PICOMETRICS to S.V.A.

European Research Council Grant 815128 REALNANO to S.B.

**Author contributions:**

Conceptualization: MM, KJ, AEMM, SB, BMW

Methodology: MM, KJ, AEMM, CV, TD, BS, EG, JNL, EAI, SVA, TA

Investigation: MM, KJ, AEMM, CV, TD, EG, JNL, WvdS, BŠ

Visualization: KJ, MM, AEMM, TD, JNL, EAI

Funding acquisition: BMW, SB

Project administration: EG, PB

Supervision: MM, BMW, SB

Writing: MM, KJ, AEMM, SB, BMW

**Competing interests:** Authors declare that they have no competing interests.

**Data and materials availability:** All data needed to evaluate the conclusions in the paper are present in the paper or the supplementary materials.

**Supplementary Materials**

Materials and Methods

Supplementary Text

Figs. S1 to S50

Tables S1 to S11

References (45-72)

Supplementary Information to

# Restructuring of titanium oxide overlayers over nickel nanoparticles during catalysis

**Authors:** Matteo Monai<sup>1,†</sup>, Kellie Jenkinson<sup>2,†</sup>, Angela E. M. Melcherts<sup>1,†</sup>, Jaap N. Louwen<sup>1</sup>, Ece A. Irmak<sup>2</sup>, Sandra Van Aert<sup>2</sup>, Thomas Altantzis<sup>3</sup>, Charlotte Vogt<sup>1,‡</sup>, Ward van der Stam<sup>1</sup>, Tomáš Duchoň<sup>4</sup>, Břetislav Šmíd<sup>5</sup>, Esther Groeneveld<sup>6</sup>, Peter Berben<sup>6</sup>, Sara Bals<sup>2,\*</sup> and Bert M. Weckhuysen<sup>1,\*</sup>

**Affiliations:**

<sup>1</sup>Inorganic Chemistry and Catalysis group, Institute for Sustainable and Circular Chemistry and Debye Institute for Nanomaterials Science, Utrecht University, Universiteitsweg 99, 3584 CG Utrecht, The Netherlands.

<sup>2</sup>EMAT and NANOlaboratory Center of Excellence, University of Antwerp, 2020 Antwerp, Belgium

<sup>3</sup>ELCAT, University of Antwerp, 2610 Wilrijk, Belgium

<sup>4</sup>Peter-Grünberg-Institut 6, Forschungszentrum Jülich GmbH, 52425 Jülich, Germany.

<sup>5</sup>Department of Surface and Plasma Science, Faculty of Mathematics and Physics, Charles University, V Holešovičkách 2, Prague 180 00, Czech Republic.

<sup>6</sup>BASF Nederland B.V., Strijkviertel 61, 3454 PK De Meern, The Netherlands.

<sup>†</sup>These authors contributed equally

<sup>‡</sup>Present address: Schulich Faculty of Chemistry, Technion, Israel Institute of Technology, Technion City, Haifa 32000, Israel

\*Corresponding authors: email: [sara.bals@uantwerpen.be](mailto:sara.bals@uantwerpen.be), [B.M.Weckhuysen@uu.nl](mailto:B.M.Weckhuysen@uu.nl)

## Materials and methods.

**Catalyst synthesis.** Ni catalysts supported on TiO<sub>2</sub> (Degussa P25, S.A. = 60 m<sup>2</sup>/g) were prepared by homogeneous deposition precipitation (HDP) with urea. For a 6 wt.% Ni/TiO<sub>2</sub> catalyst, 0.4807 g of Ni (II) nitrate hexahydrate (99.999%, Sigma Aldrich) and 3.0 g of urea (p.a., Acros) were dissolved in 130 mL of water, followed by the addition of 1.52 g of TiO<sub>2</sub>. The system was kept at 95 °C for 20 h under vigorous stirring to induce Ni precipitation via the hydrolysis of urea (45). Then, the system was washed by centrifugation with water until the pH of the supernatant was neutral. The resulting powders were dried at 60 °C overnight, followed by further drying at 120 °C for 24 h.

**Catalyst characterization.** Inductively coupled plasma-optical emission spectroscopy (ICP-OES) analysis was used to measure the actual Ni loading on the synthesized Ni/TiO<sub>2</sub> catalyst materials. The ICP-OES measurements have been performed by the Geolab (Utrecht University), using a SPECTRO CIROSCCD (by SPECTRO Analytical Instruments GmbH, Germany). Samples were dissolved using an aqua regia/HF solution at 90 °C overnight, after which the solution was cooled down to RT, neutralized using boric acid and diluted with ultrapure water to yield solutions of appropriate concentration for analysis.

Temperature programmed reduction (TPR) and temperature programmed oxidation (TPO) profiles of the catalyst materials were obtained with an AutoChem II 2920 V4.03 equipped with a TCD detector. 50 mg of catalyst was reduced to either 600 °C or 800 °C (300 °C/h) under a flow of 5 vol.% H<sub>2</sub> in Ar. TPO was performed after TPR to show the uptake of oxygen of the reduced catalyst materials. The temperature was lowered under Ar atmosphere. Subsequently, the temperature was raised again to 600 °C or 800 °C under 5 vol.% O<sub>2</sub>/He.

H<sub>2</sub> chemisorption measurements were performed on a Micrometrics ASAP 2020 C. About 200 mg of sample was used. Before the measurements, the samples were reduced for 1 h at different reduction temperatures (i.e., 400 °C and 600 °C) with a ramp of 600 °C/h under pure H<sub>2</sub> flow (1020–1090 mbar). After reduction, the samples were evacuated and cooled to 35 °C, after which the samples were exposed to H<sub>2</sub> (645 mbar) to measure the amount of gas adsorbed. As H<sub>2</sub> can be both physisorbed and chemisorbed, both forms are measured during the first adsorption isotherm. To determine solely the chemisorbed H<sub>2</sub> amount, proportional to the Ni active area, the sample was then evacuated to remove all the physisorbed H<sub>2</sub>, and the procedure was repeated. The difference between the values gives the chemisorbed H<sub>2</sub> volume. The Ni particle size was calculated with an assumed atomic cross-section of 0.0649 nm<sup>2</sup> and a density of 8.902 cm<sup>3</sup>/g. The H/Ni ratio was assumed to be one and the particles to be hemispherical.

The pre-reduced and used Ni/TiO<sub>2</sub> catalyst materials were examined with scanning transmission electron microscopy (STEM) in combination with high-angle annular dark-field (HAADF) and energy dispersive X-ray (EDX) analyzes on an FEI Talos F200X, after passivation in air. The microscope was operated at 200 kV and equipped with a high-brightness field emission gun (X-FEG) and a Super-X G2 EDX detector. STEM samples were prepared by drop-casting samples on lacey carbon film, 300 mesh gold grids (PELCO). The samples were crushed and dispersed in pure ethanol under ultrasonic vibration and finally deposited on the grids by drop-casting. The grids were placed in a low background sample holder for measurements. The particle size distribution was determined for pre-reduced and used samples using the ImageJ software (version 1.53).

Powder X-ray diffraction (XRD) patterns of support, pre-reduced and used catalyst materials were obtained with a Bruker D2 Advance powder X-ray diffractometer equipped with automatic divergence slits, a Vantec detector and a cobalt K $\alpha_{1,2}$  ( $\lambda = 1.7889/1.79026$  Å) source. XRD patterns were collected between 25–100 ° with an increment of 0.05 ° and an acquisition time of 26 s per step.

X-ray photoelectron spectroscopy (XPS) measurements were carried out at Charles University, Prague, CZ using a lab-based system (SPECS Surface Nano Analysis GmbH, monochromatized Al-K $\alpha$  source) with a base pressure of 5×10<sup>-10</sup> mbar. XPS samples were prepared by pressing the catalyst materials into a tungsten mesh (wire diameter 0.05 mm, nominal aperture 0.2 mm, purity 99.95%, Goodfellow, England) in between two sheets of a weighing paper (Machery-Nagel, Germany) via a mechanical press (H-62, Trystom, CZ) with a force of 70 kN. Samples were characterized in situ in 0.3 mbar of H<sub>2</sub> (5.0, Air Liquide), and from 0 to 1.2 mbar CO<sub>2</sub> at 400 °C, and reference samples were characterized in ultra-high vacuum (UHV) at room temperature. The temperature was ramped up after the introduction of the H<sub>2</sub>. Survey scans were recorded for all the samples along with Ni 2p, O 1s, Ti 2p, and C 1s core-level spectra. The core-level spectra were recorded with pass energy of 20 eV, step size of 0.05 eV, and dwell time of 200 ms and corrected for charging assuming the binding energy of Ti 2p<sub>3/2</sub> to be 458.5 eV for TiO<sub>2</sub>.

**In-situ and operando electron microscopy studies.** All in-situ and in operando electron microscopy studies were carried out using an aberration-corrected ThermoFisher Scientific – Titan Cubed electron microscope operating at 300 kV. The gas and heating nanoreactor comprised two electron-transparent Si<sub>3</sub>N<sub>4</sub> windowed chips and a gas cell holder

(climate G+, DENSsolutions). To minimize potential electron beam induced artefacts, the electron dose was reduced to approximately  $5580 \text{ e}^-/\text{\AA}^2$  and a low screen current of 50 pA, which is consistent with previous in-situ gas phase STEM microscopy investigations (23). Moreover, we elected to blank the electron beam in between acquisitions and when the climate system was stabilizing from changing reaction parameters (temperature of gas feed mixture) to prevent unnecessary additional irradiation. To ensure that the catalyst's structural evolution was not a product of electron beam exposure, we compared the observed catalyst behavior at key stages of the experiments with alternative windows that had no prior electron beam exposure. This comparison method aligns with current state-of-the-art in-situ microscopy studies of SMSIs (10, 12) and showed an identical overlayer formation and (partial) removal without irradiation, therefore allowing us to conclude that our observations are not a product of electron beam induced artefacts.

(i) *Ni/TiO<sub>2</sub> synthesis.* Ni(OH)<sub>x</sub>/TiO<sub>2</sub> was dispersed in ethanol and deposited on the lower climate chip before constructing the climate holder and sealing the nanoreactor. All gas supply system lines and the nanoreactor were subject to a pump-purge protocol three times to flush any moisture and oxygen from the system. A region of interest was imaged before the reaction to show TiO<sub>2</sub> without NPs present before blanking the beam to prevent electron beam induced artefacts or Ni nucleation. The Ni nanoparticles were reduced for four hours in a 1:1 mixture of He and H<sub>2</sub> at 400 °C (400-Ni/TiO<sub>2</sub>) or 600 °C (600-Ni/TiO<sub>2</sub>). The measurements were performed at atmospheric pressure. Ni's oxidation state was confirmed by atomic resolution HAADF STEM imaging.

(ii) *CO<sub>2</sub> hydrogenation.* Once the Ni/TiO<sub>2</sub> catalyst was prepared in situ, the temperature was either maintained at (or lowered to) 400 °C. Several particles, oriented such that a primary zone axis could be imaged, were chosen to compare before and during hydrogenation to assess their morphology and the extent of TiO<sub>2</sub> encapsulation. CO<sub>2</sub> and H<sub>2</sub> in a 1:3 ratio were pre-mixed in an inbuilt mixing chamber of the gas supply system for 10 min to ensure a homogenous mixture before being diverted into the nanoreactor to initiate the hydrogenation reaction at 1 atmosphere. Reactants and reaction products exiting the nanoreactor were measured using a dedicated gas analyzer (DENSsolutions). Although H<sub>2</sub>O was detected in all cases, it could not be quantified. To mitigate the potential for electron beam induced artefacts, such as the enhanced or reduced stability of TiO<sub>2-x</sub>, the electron beam was blanked, while the gas mixture was changed, and each particle was observed sparingly. Moreover, to ensure observations are an accurate depiction of the catalyst's behavior, windows within the Si<sub>3</sub>N<sub>4</sub> chip were left unexposed to the electron beam until their investigation after CO<sub>2</sub> + H<sub>2</sub> introduction to confirm shell removal without any prior irradiation.

(iii) *STEM image restoration and registration.* An in-house developed convolutional neural network (CNN) was first used to correct distortions. More details regarding the training of the CNN for the restoration of ADF STEM images can be found in ref. (23). To correct sample drift or rotation, each time series of images corrected by CNN was then used as an input for an in-house developed rigid and non-rigid registration procedures (46). Next, every series of individually corrected and registered ADF STEM images was averaged to increase signal-to-noise ratio and to clearly resolve projected atomic columns.

(iv) *Quantitative analysis on STEM images.* A peak finding routine that searches for local maxima in ADF STEM images was applied. The atomic columns corresponding to the Ni NP and TiO<sub>x</sub> overlayer were then identified by classifying the peaks based on the lattice parameter of the Ni crystal structure. Next, the positions resulting from this peak finding routine have been used as an input for further refinement using statistical parameter estimation theory. Therefore, the projected atomic columns viewed along a major zone axis were modelled as a superposition of 2D Gaussian peaks on a constant background(24). By fitting this model to the experimental images using a criterion of goodness of fit, which quantifies the similarity between the experimental images and the model, accurate and precise positions of atomic columns could be obtained. This is performed using an iterative optimization algorithm, which is implemented in the StatSTEM software package (47).

The projected atomic displacement maps were extracted for the projected Ni atomic columns using the ideal positions of the Ni atoms as a reference. By calculating derivatives of the displacement map, the strain distribution in the Ni particle was investigated (48).

Because of the low signal-to-noise ratio, especially for the TiO<sub>x</sub> overlayer, atomic columns are difficult to detect using peak finding combined with statistical parameter estimation theory, as explained above. Therefore, we applied a more advanced statistical method. The so-called maximum a posteriori (MAP) probability rule has been developed based on a combination of statistical parameter estimation theory and Bayesian probability theory and can be used to reliably detect atomic columns. The MAP rule searches for possible column locations and compares probabilities of all



candidate parametric models. The selected number of columns corresponds to the model for which the probability is the largest. More details regarding the MAP rule can be found in ref (25, 26). The estimated atomic column positions on the outer layer of the Ni NP ( $x_{Ni}$ ), inner ( $x_{Ti1}$ ) and outer ( $x_{Ti2}$ ) layers of the TiO<sub>x</sub> overlayer are shown in Fig SA.

Next, the perpendicular distance between the outer layer of the Ni NP and the inner Ti layer, as well as the Ti-Ti interplanar distances were measured (Fig. S14). Therefore, we first applied a linear regression model to the atomic column positions located on the outer layer of the Ni NP, shown as red dots in Fig. S14 ( $x_{Ni}$ ). The linear regression model provided a model of a straight line with slope  $m$  and intercept  $c_{Ni}$ . We then used this estimated slope while fitting the linear regression model to the Ti atomic columns on the inner and outer layers. From this model, we estimated the intercept for each Ti-layer ( $c_{Ti-layer1}$ ,  $c_{Ti-layer2}$ ), along with their standard error values. Next, the perpendicular distance between the outer layer of the Ni NP and the inner Ti layer ( $d_{Ni-Ti}$ ) and Ti overlayer interplanar distance were calculated using equations (1) and (2).

$$d_{Ni-Ti} = \frac{|c_{Ni} - c_{Ti-layer1}|}{\sqrt{1 + m^2}} \quad (1)$$

$$d_{Ti-Ti} = \frac{|c_{Ti-layer1} - c_{Ti-layer2}|}{\sqrt{1 + m^2}} \quad (2)$$

It is important to note that this approach assumes that all layers are parallel to each other. Moreover, we used error propagation to compute the error on the estimated interplanar distances. The outcome of all these analyses for three different particles is tabulated in Fig. S17. We also measured average interatomic distances for Ti-Ti atomic columns located on the inner ( $\Delta x_{Ti1}$ ) and outer ( $\Delta x_{Ti2}$ ) Ti-layers using equation (3).

$$\Delta x_{Ti} = \frac{\sum_{n=2}^N \sqrt{(x_{Ti,n} - x_{Ti,n-1})^2}}{N - 1}, \quad (3)$$

Where  $N$  represents the number of atomic columns located on each T-layer and  $x_{Ti}$  is the 2D coordinate vector of Ti atomic columns,  $x_{Ti,n} = (x_{Ti,n}, y_{Ti,n})$ . The interatomic distances for each layer and the standard deviation on the estimated values are also presented in Fig. S17.

**Operando FT-IR spectroscopy with on-line product analysis.** Operando transmission FT-IR spectroscopy was carried out in a Specac High-Temperature transmission IR cell. Catalyst preparation was done by preparing pellets of compressed catalyst powder (4 tons of pressure) of 13 mm weighing between 15–30 mg. These pellets were made with a Specac Laboratory Pellet Press and a diaphragm vacuum pump. The Ni/TiO<sub>2</sub> catalysts were reduced with H<sub>2</sub> in situ at 400 °C or 600 °C (ramp 5 °C/min) for 1 h at 1 bar. A total flow of 50 mL/min (He:H<sub>2</sub> = 1:1) was used. After the in-situ reduction, the CO<sub>x</sub> hydrogenation reactions were carried out using 3:1:7 CO<sub>2</sub>:CO:H<sub>2</sub> flow at 5 bar with CO<sub>2</sub> at 6 mL/min, CO at 2 mL/min, and H<sub>2</sub> at 14 mL/min. He was used to dilute the gases to a total flow of 40 mL/min. The reaction gases were introduced at 200 °C, and the temperature was held for 30 min. This step was repeated for 250 °C, 300 °C, 350 °C, and 400 °C at 5 bar. CO<sub>2</sub> hydrogenation was carried out with the same temperature program using 1:4 CO<sub>2</sub>:H<sub>2</sub> at either 1 or 5 bar. All gases were introduced through Bronkhorst EL-FLOW Mass Flow Controllers. Active carbon carbonyl traps were placed before the reactor for safety against the formation of volatile and highly toxic Ni(CO)<sub>4</sub>.

Operando transmission FT-IR spectroscopy measurements were performed with a Bruker Tensor 37 FT-IR spectrometer with a deuterated triglycine sulphate (DTGS) detector. A spectrum was taken every 30 s. To follow the formed reaction products, an Interscience custom-built Global Analyzer Solutions (G.A.S.) Compact GC<sub>4.0</sub> gas chromatograph (GC) was connected to the outlet of the reaction cell. H<sub>2</sub>, CO and CO<sub>2</sub> signals were calculated with a thermal conductivity detector (TCD). Methane, ethane, ethene, propane, propene and n-butane values were detected with a Flame Ionisation Detector (FID). The shown error bars are based on the standard deviations of the used GC data points. For TOF calculations, the number of Ni atoms on the surface was based on spherical Ni nanoparticles, with 10 Ni atoms per nm<sup>2</sup>.

Conversion of CO ( $X_{CO}$ ), CO<sub>2</sub> ( $X_{CO_2}$ ) and total conversion ( $X_{CO_x}$ ) were calculated according to the following, with  $\nu_n$  being the number of carbon atoms of the species  $n$  (e.g., 2 for ethane):

$$X_{CO}(\%) = \frac{[CO]_{In} - [CO]_{Out}}{[CO]_{In}} \cdot 100 \quad (1)$$

$$X_{CO_2}(\%) = \frac{[CO_2]_{In} - [CO_2]_{Out}}{[CO_2]_{In}} \cdot 100 \quad (2)$$

$$X_{CO_x}(\%) = \frac{\sum \nu_n [C_n]_{n,Out}}{[CO_2]_{Out} + [CO]_{Out} + \sum \nu_n [C_n]_{n,Out}} \cdot 100 \quad (3)$$

Carbon yield to C<sub>n</sub> ( $Y_{C_n}$ ) and product selectivity ( $S_{C_n}$ ) were calculated as:

$$Y_{C_n}(\%) = \frac{\nu_n [C_n]_{n,Out}}{[CO_2]_{Out} + [CO]_{Out} + \sum \nu_n [C_n]_{n,Out}} \cdot 100 \quad (4)$$

$$S_{C_n}(\%) = \frac{Y_{C_n}}{X_{CO_x}} \cdot 100 \quad (5)$$

Carbon balance was not included in the selectivity calculations because it was comparable for the catalysts studied herein under any reaction conditions (see Table S6).

The TOF was calculated based on the exposed metal surface area, as determined by the mean Ni particle sizes obtained by ex-situ HAADF-STEM after the reaction. The Ni NP shape was assumed spherical, with 10 Ni atoms per nm<sup>2</sup>.

$$TOF_{C_n}(s^{-1}) = \frac{[C_n]}{n_{Ni\ surface}} \quad (6)$$

### Computational Details

The calculations were performed with the Quickstep module of the program CP2K, version 8.1(49–51) using the PBE GGA type density functional (52) with D3 Grimme corrections for nonbonded interactions.(53, 54) A MOLOPT double- $\zeta$  plus polarization function valance basis set(55) was used in conjunction with GTH pseudopotentials.(56, 57) Electron smearing was applied using Fermi-Dirac statistics and an electronic temperature of 300 K. For SCF convergence, a target accuracy of 10<sup>-6</sup> Hartree was specified. For locating the minimum energy geometry by the BFGS method, standard program settings were used. The calculations were performed with periodic boundary conditions and the k-point grid was based on the Monkhorst-Pack scheme.(58)

We realize that the use of periodic boundary conditions (PBC) in the directions parallel to the surface is an approximation as it assumes infinite surfaces covered by infinite layers, whereas we are in actual fact dealing with finite nanoparticles. However, since realistic nanoparticles contain too many atoms to be treated at this level of theory, the use of PBC is preferred to doing computations on unrealistically small particles. Using PBC incurs the danger of imposing too strict periodicity. This can be mitigated by the use of a large unit cell (instead of using a small cell with many k-points).

Models for Ni surfaces were created from a slab of four layers of Ni. For the unit cell size of FCC Ni we used a computed value of 3.5291 Å. Rutile (110) and anatase (101) layer dimensions were based on the PBE-D3 computed crystal structures. It has been shown before that the anatase (101) surface is the most stable one, so if any anatase overlayers were formed these would be expected to be (101) layers.(59)

The rutile structure was computed with full optimization of lattice vector lengths and atom positions (specifying a pressure tolerance of 10 bar), using a 6x6x10 mesh of k-points. The computed lattice vector lengths of a = b = 4.6111 Å and c = 2.9633 Å compare well with the experimental values of 4.5937 Å and 2.9581 Å, respectively.(60) For anatase a 7x7x3 k-points mesh was applied and the computed lattice vector lengths were a = b = 3.7852 Å, c = 9.6565

$\text{\AA}$ , in reasonable agreement with the experimental values of  $a = b = 3.7852 \text{ \AA}$ ,  $c = 9.6565 \text{ \AA}$ .<sup>(61)</sup> Based on these bulk structures, the 2D lattice vectors for the rutile (110) layer are  $a = 2.9581 \text{ \AA}$ ,  $b = 6.4834 \text{ \AA}$  and for anatase (101):  $a = 3.7852 \text{ \AA}$ ,  $b = 10.3719 \text{ \AA}$ .

### Reducibility of Ni/TiO<sub>2</sub> catalysts

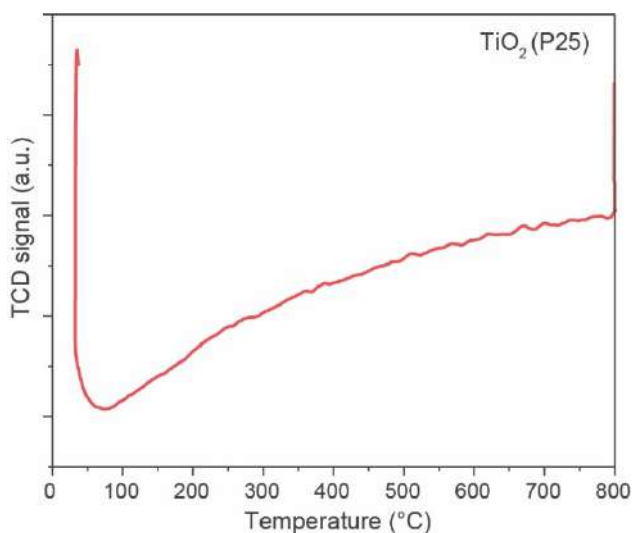


**Fig. S1.** Temperature Programmed Reduction (TPR) profile of TiO<sub>2</sub> (P25, Degussa) reduction in H<sub>2</sub> (5 vol.%) / Ar at 1 bar as a function of temperature.

TiO<sub>2</sub> shows a weak gradual consumption of hydrogen, indicating that H<sub>2</sub> spillover from Ni is required to reduce TiO<sub>2</sub> under the TPR conditions.

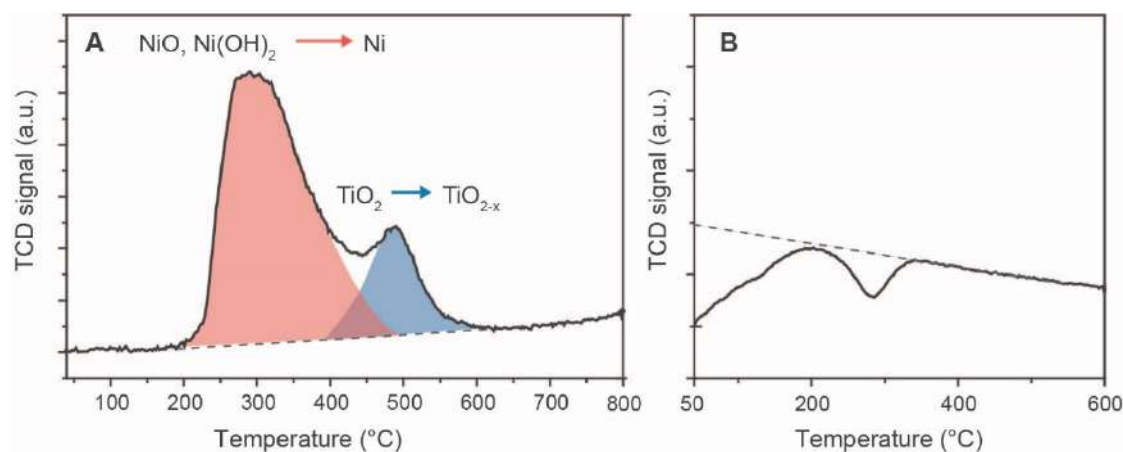


**Fig. S2.** (A) Temperature Programmed Reduction (TPR) profile and (B) Temperature Programmed Oxidation (TPO) profile of the fresh Ni/TiO<sub>2</sub> catalyst after a TPR to 600 °C, showing NiO and TiO<sub>2</sub> redox behavior.

A large peak at 200–450 °C is assigned to the reduction of nickel oxide/hydroxide to metallic nickel, while the smaller peak centered at 493 °C is assigned to TiO<sub>2</sub> partial reduction catalyzed by metallic Ni (Fig. S2A) (62). Notably, the onset of TiO<sub>2</sub> reduction is consistent with thermodynamic calculations, which also predict about 1% of Ti<sub>2</sub>O<sub>3</sub> to be formed at 600 °C (Fig. S3). This amount is about 15 wt./wt.% with respect to Ni content, which is 2–3 times higher than the dispersion of 7–14 nm NPs, meaning that the amount would be enough to cover all Ni surface atoms (TiO<sub>2</sub>/Ni weight = 1.4, Ni/TiO<sub>2</sub> density = 2.1). Accordingly, 400 °C and 600 °C were chosen as the two reduction temperatures for this study, to grant Ni reduction, while modulating SMSI. Re-oxidation of Ni/TiO<sub>2</sub> during a subsequent O<sub>2</sub>-TPO shows two main contributions at low temperature and 300 °C, showcasing the reactivity of the catalyst to oxidizing gaseous molecules at temperatures comparable to those used for CO<sub>x</sub> hydrogenation (Fig. S2B). The drift in baseline of oxygen consumption shows further oxidation of the catalyst at higher temperatures, which was previously exploited in ROR treatments (10, 11).

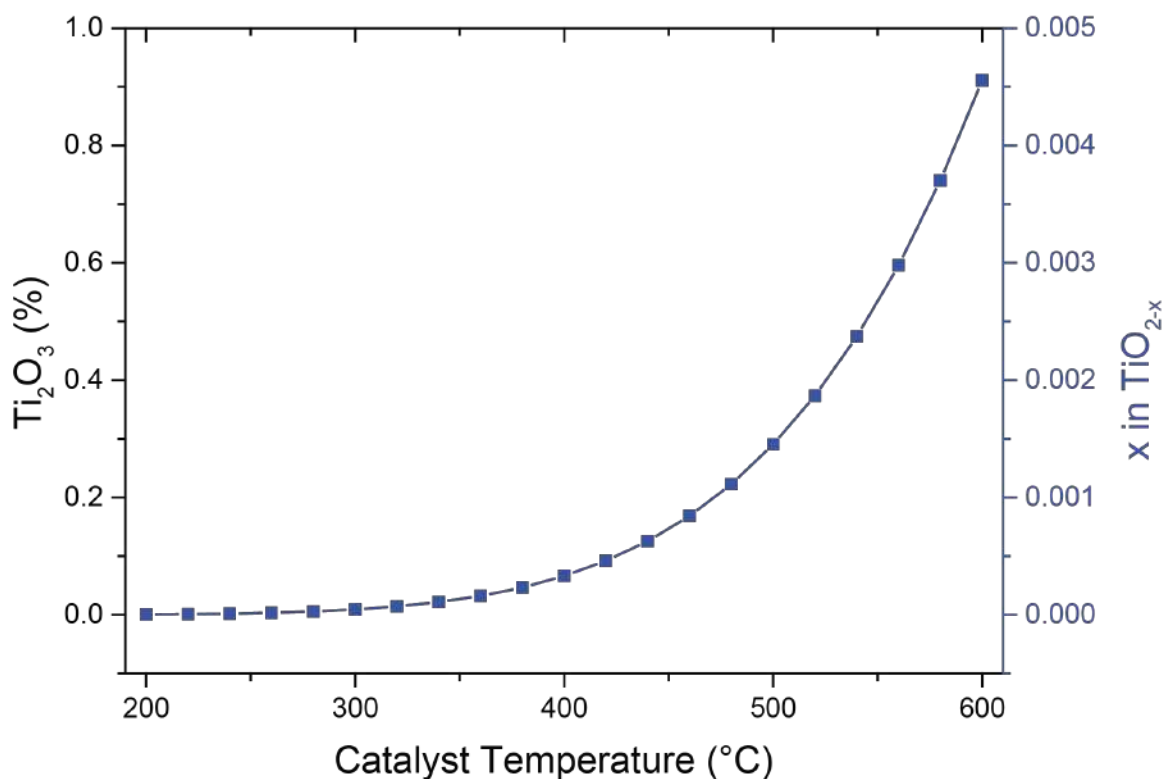


**Fig. S3.** Thermodynamic equilibrium for TiO<sub>2</sub> reduction in H<sub>2</sub> (5 vol.)/He at 1 bar as a function of temperature. Equilibrium calculations were performed using the HSC Chemistry 9.1 software in the Gem equilibrium composition module by the Gibbs free energy minimization method.

Notably, the onset of TiO<sub>2</sub> reduction is at 400 °C, which is the onset of the second peak observed by TPR (Fig. S2).

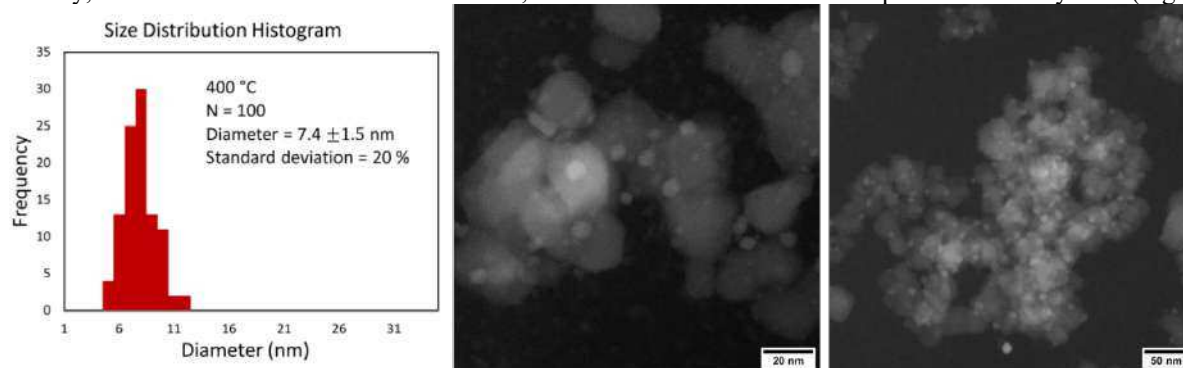


**Fig. S4.** In-situ growth of 400-Ni/TiO<sub>2</sub> showing well dispersed Ni metal nanoparticles supported on larger TiO<sub>2</sub> crystallites.

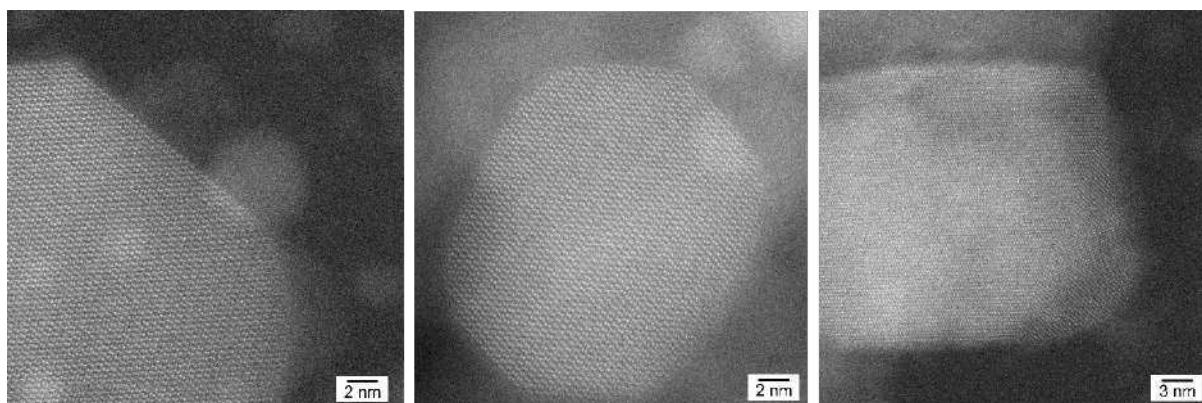


Fig. S5. 400-Ni/TiO<sub>2</sub> prepared in situ in H<sub>2</sub> and He after 4 h showing the formation of Ni-based NPs with poor crystallinity. Large crystalline particles correspond to TiO<sub>2</sub> support.

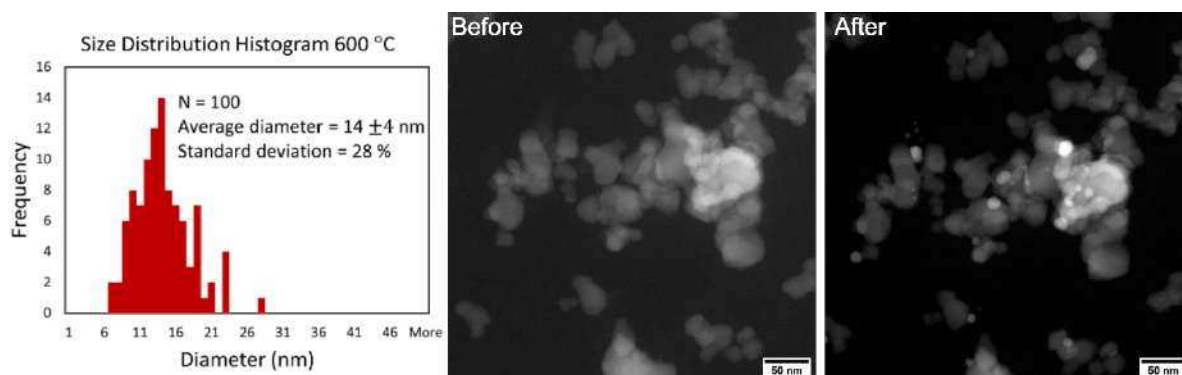


Fig. S6. The same area before and after in-situ growth of 600-Ni/TiO<sub>2</sub> to produce well dispersed Ni metal nanoparticles supported on larger TiO<sub>2</sub> crystallites.

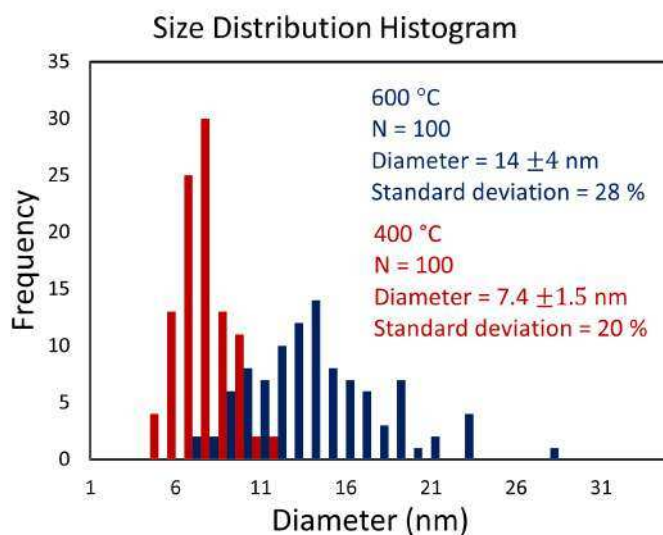
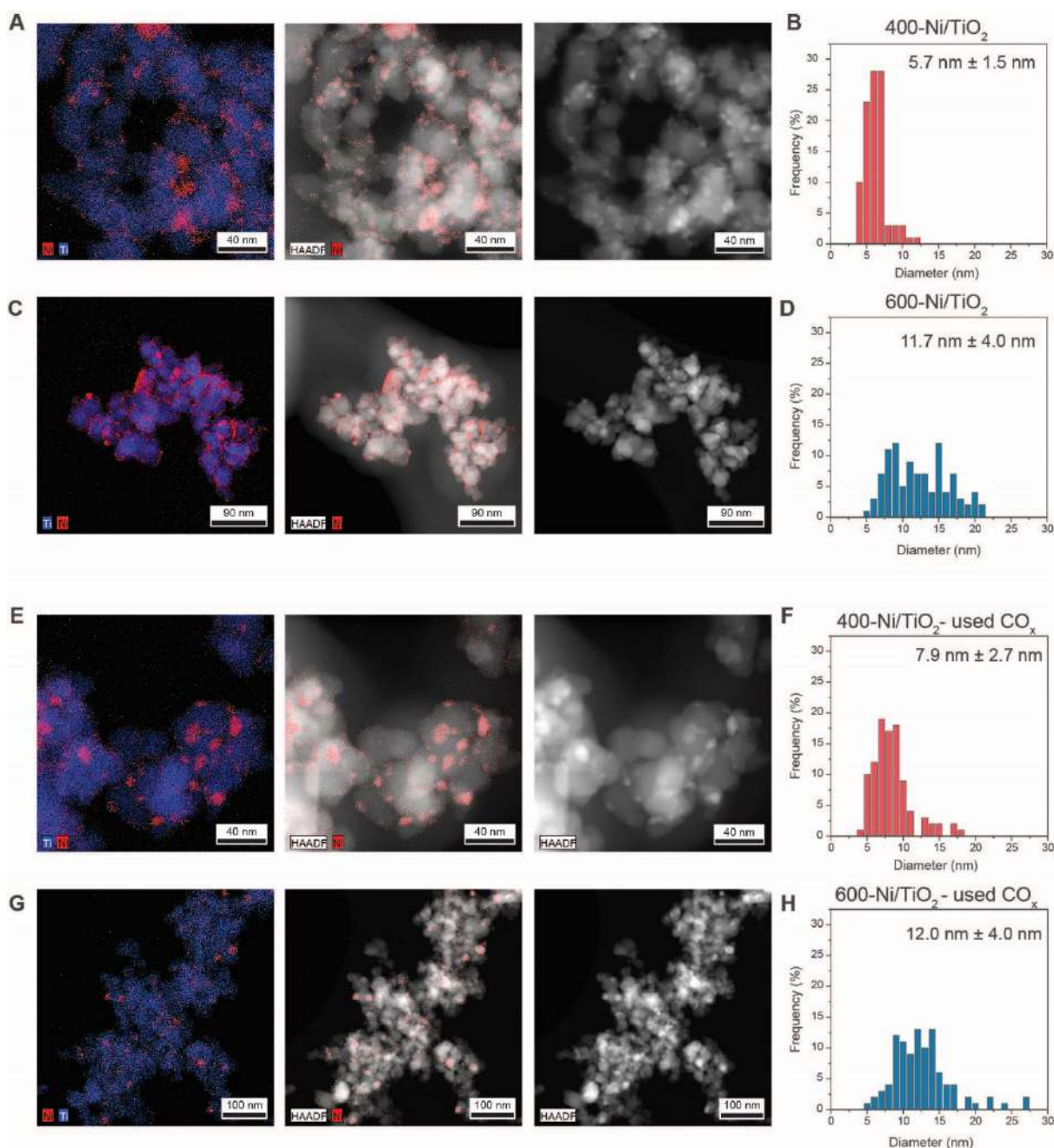


Fig. S7. Particle size distribution comparison between 400-Ni/TiO<sub>2</sub> (red) and 600-Ni/TiO<sub>2</sub> (blue) prepared in situ.



**Fig. S8.** Ex-situ STEM characterization of 400-Ni/TiO<sub>2</sub> and 600-Ni/TiO<sub>2</sub> after ex-situ reduction (A-D) and CO<sub>x</sub> hydrogenation (E-H) (CO<sub>2</sub>:CO:H<sub>2</sub>:He = 3:1:7:16, 5 bar, GHSV = 80,000 h<sup>-1</sup>).

Both Ni/TiO<sub>2</sub> catalysts show some Ni NP growth after CO<sub>x</sub> hydrogenation, going from 5.7 ± 1.5 to 7.9 ± 2.7 nm for the used 400 °C reduced catalyst and from 11.7 ± 4.0 to 12.0 ± 4.0 nm for the used 600 °C reduced catalyst. NP growth was more evident than for pure CO<sub>2</sub> hydrogenation (S29), which can be attributed to the effect of CO on the formation of volatile carbonyl species that tend to migrate from smaller NPs to bigger NPs and induce Ostwald ripening (63). NP growth was also observed by XRD analysis of the used 400 °C reduced catalyst, using the Scherrer equation to derive average crystallite size (Table S2) (64).

**Table S1.** Ni particle sizes in Ni(6 wt.)/TiO<sub>2</sub> catalysts after reduction at different temperature, fresh and used after CO<sub>x</sub> hydrogenation reaction, as determined by High-Angle Annular Dark-Field Scanning Transmission Electron Microscopy (HAADF-STEM), X-ray Diffraction (XRD) and H<sub>2</sub>-chemisorption. The last column reports the average Ni surface coverage by TiO<sub>2-x</sub>, calculated based on HAADF-STEM and H<sub>2</sub>-chemisorption results.

<b>Catalyst</b>	<b>HAADF-STEM particle size (nm)</b>	<b>XRD crystallite size (nm)<sup>a</sup></b>	<b>H<sub>2</sub>-chemisorption apparent size (nm)<sup>b</sup></b>	<b>Average Ni surface covered by TiO<sub>2-x</sub> (%)<sup>c</sup></b>
Ni/TiO <sub>2</sub> -400 °C fresh	5.7 ± 1.5	n.a. <sup>d</sup>	15	30
Ni/TiO <sub>2</sub> -600 °C fresh	11.7 ± 4.0	14.5 ± 0.2	352	97
Ni/TiO <sub>2</sub> -400 °C used	7.9 ± 2.7	10.9 ± 0.9	n.a. <sup>e</sup>	n.a.
Ni/TiO <sub>2</sub> -600 °C used	12.0 ± 4.0	14.2 ± 0.4	n.a.	n.a.

<sup>a</sup>derived from Scherrer's equation on nickel (200) reflection  $2\theta = 52.2-52.4^\circ$  (see SI for details)

<sup>b</sup>calculated assuming Ni:H stoichiometry of 1, hemispherical nanoparticles and 10 Ni atoms per nm<sup>2</sup>

<sup>c</sup>calculated assuming hemispherical nanoparticles, as a ratio between geometrical surface from HAADF-STEM and available surface from H<sub>2</sub>-chemisorption

<sup>d</sup>no XRD reflection was observed, suggesting the presence of small crystallites, in accordance with TEM.

<sup>e</sup>n.a. = not applicable. The H<sub>2</sub> chemisorption analysis could not be carried out on used samples without exposure to air, which would induce passivation and prevent a correct estimation of exposed Ni sites. The coverage is instead derived by operando FT-IR spectroscopy experiments (Fig. 3).



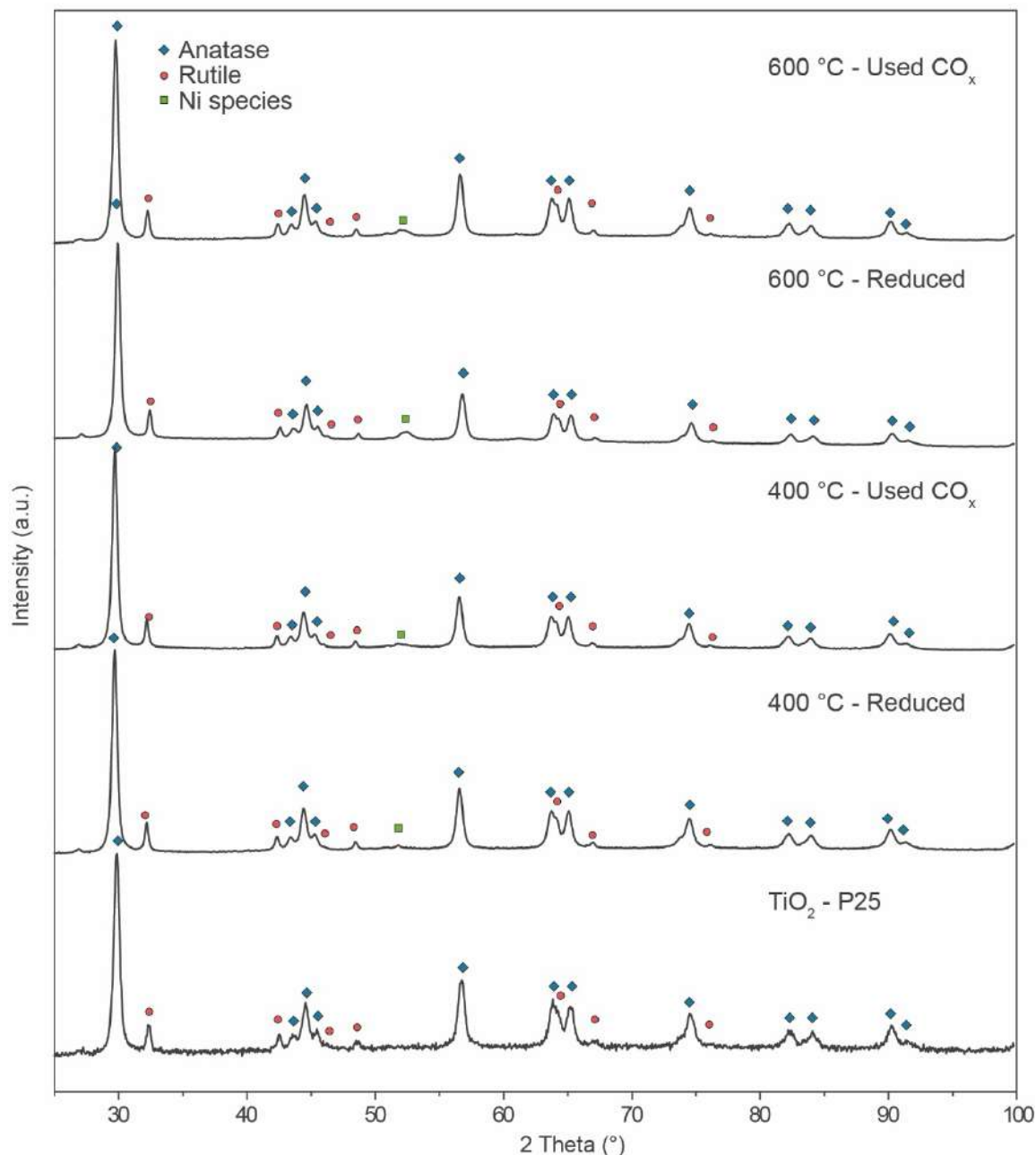


**Fig. S9. X-ray diffraction (XRD) patterns of fresh TiO<sub>2</sub> (P25, Degussa) support, reduced Ni(6 wt%)/TiO<sub>2</sub> at 400 °C and 600 °C and used catalyst materials after the CO<sub>x</sub> hydrogenation reaction.**

XRD results (Fig. S9) indicate that the bulk crystalline structure of the TiO<sub>2</sub> P25 support is not appreciably changed by any of the stages of the catalyst life, from synthesis to pretreatments and reaction runs. Notably, this observation is not in contrast with SMSI formation, as SMSI only involves a very thin layer, which cannot be observed by bulk characterization (10), but it rules out extended TiO<sub>2</sub> phase transformation from e.g. anatase to rutile at 600 °C, which could have affected the catalytic activity (36).

**Table S2. Nickel size calculation based on the position of maximum intensity of the reflections and FWHM by the Scherrer equation.**

Catalyst	Reflection	Reflection Position (°)	FWHM (°)	Crystallite size (nm) <sup>a</sup>
Ni/TiO <sub>2</sub> - 400 °C	NiO (012)	50.944 ± 0.046	0.51 ± 0.12	30.1 ± 6.9
Ni/TiO <sub>2</sub> - 400 °C - used	NiO (012)	50.990 ± 0.039	0.46 ± 0.10	33.6 ± 7.9
	Ni (200)	52.232 ± 0.074	1.44 ± 0.12	10.9 ± 0.9
Ni/TiO <sub>2</sub> - 600 °C	NiO (012)	51.169 ± 0.026	0.59 ± 0.06	26.1 ± 2.8
	Ni (200)	52.473 ± 0.006	1.09 ± 0.02	14.5 ± 0.2
Ni/TiO <sub>2</sub> - 600 °C - used	NiO (012)	50.950 ± 0.033	0.71 ± 0.08	21.6 ± 2.3
	Ni (200)	52.233 ± 0.020	1.10 ± 0.03	14.2 ± 0.4

<sup>a</sup>Calculated by the Scherrer equation:  $D = \frac{K\lambda}{\beta \cos \theta}$ , where K = 0.94 is the Scherrer constant,  $\lambda = 0.1789$  nm is the X-ray source wavelength (Co K $\alpha_{1,2}$ ),  $\beta$  is the FWHM in radians and  $\theta$  is the peak position in radians.

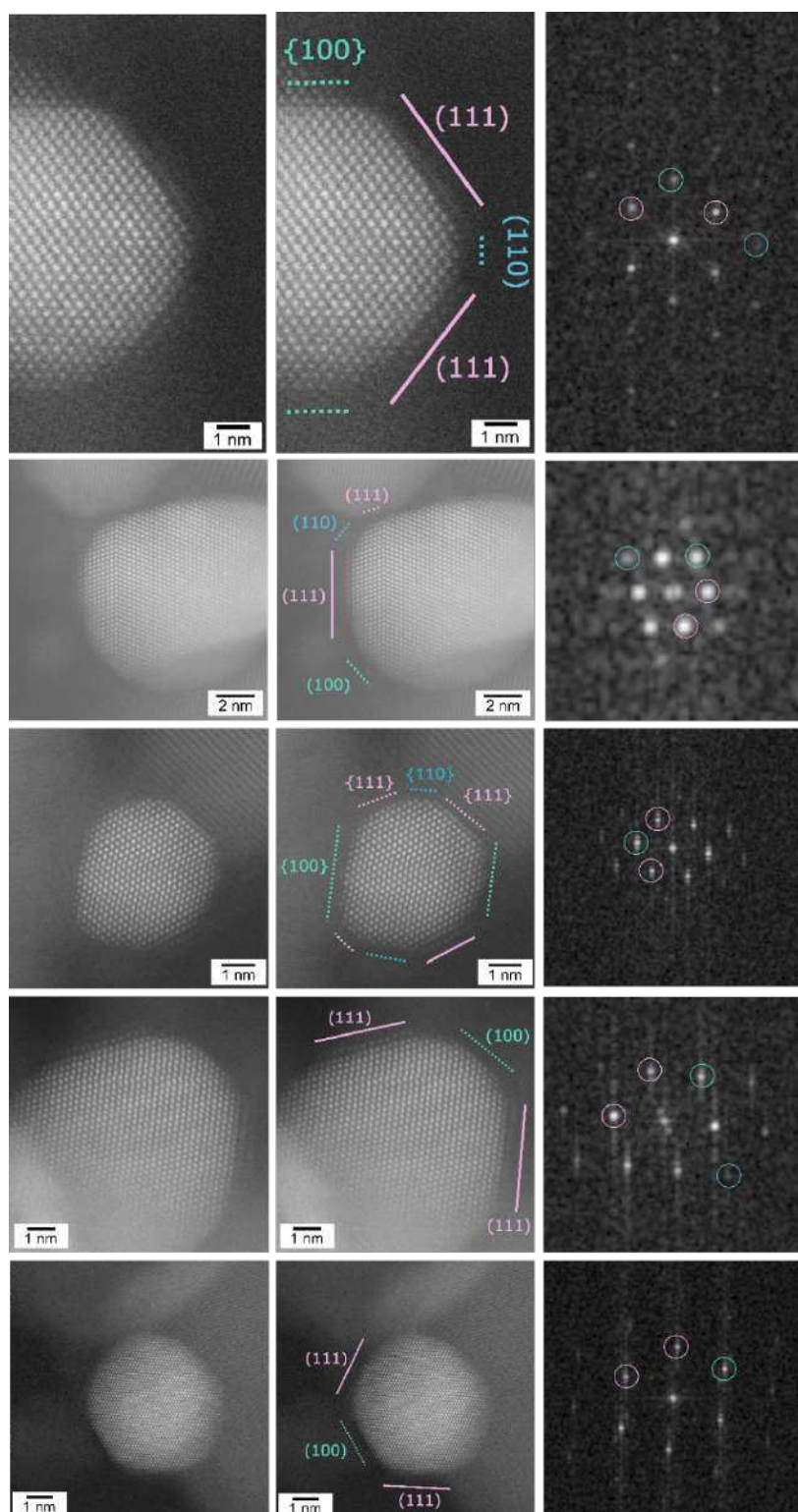


**Fig. S10.** Evidence of Ni metal oxidation state and facet selective titanium suboxide overlayer growth for 400-Ni/TiO<sub>2</sub> prepared in situ. Left column shows unannotated atomic resolution HAADF STEM images of individual nanoparticles displaying a surface TiO<sub>2-x</sub> bilayer. Center column shows the same images annotated with surface facets (111) pink, (100) green, and (110) blue, where complete lines and dashed lines indicate overlayer presence or absence, respectively. Right column shows indexed FTs of corresponding Ni NPs.

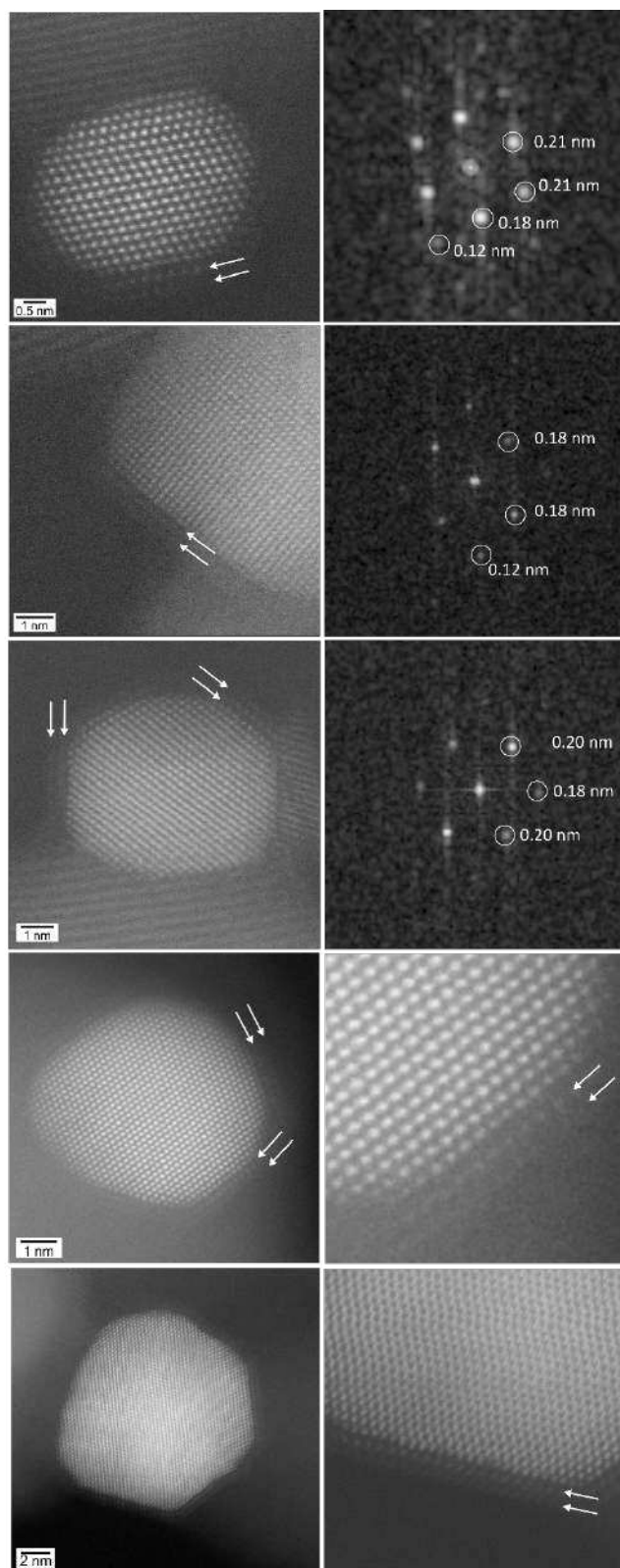


**Fig. S11.** Evidence of Ni metal oxidation state and two fully-encapsulating atomic layers of titanium suboxide overlayer for 400-Ni/TiO<sub>2</sub> pre-reduced sample, which has been re-reduced in situ. Showing atomic resolution HAADF STEM images and corresponding FTs with interatomic distances confirming Ni metal and white arrows highlighting TiO<sub>2-x</sub> atomic layers.

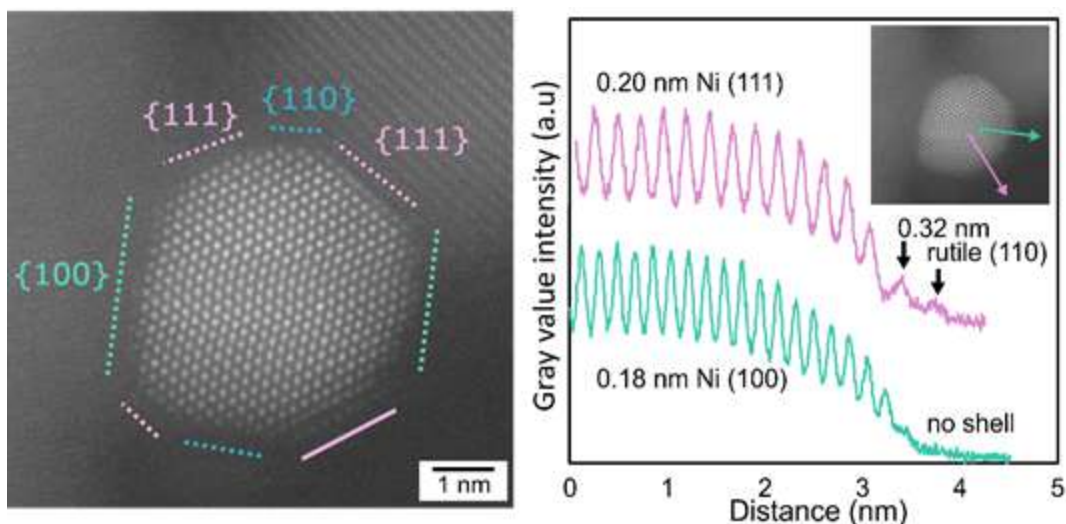


Fig. S12. (left) Atomic resolution HAADF STEM images of Ni/TiO<sub>2</sub> catalyst in H<sub>2</sub> at 400 °C shown in Fig. 1. Solid line indicates TiO<sub>x</sub> covered Ni atomic plane and dashed lines indicate uncovered planes. (111), (110) and (100) facets are indicated by pink, blue and green, respectively. (right) Line scan intensity profiles over the same Ni NP across (111) in pink and (100) in green, the directions of the line scan are shown in the inset. Arrows indicate atomic columns allocated to TiO<sub>x</sub> overlayer.

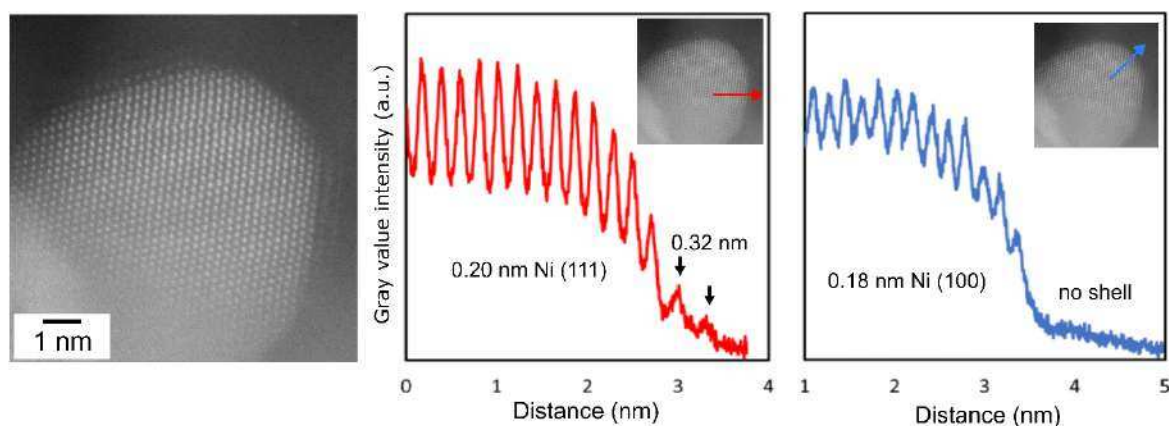


Fig. S13. Evidence for facet selectivity of in-situ prepared TiO<sub>2-x</sub> bilayer on 400-Ni/TiO<sub>2</sub> by atomic resolution HAADF STEM imaging. Left: HAADF STEM image of a Ni NP. Middle and Right: gray scale intensity line scans showing the clear occupation of a TiO<sub>2-x</sub> bilayer upon the (111) surface facet (middle) and absence of any overlayer upon the (100) facet (right). The TiO<sub>2-x</sub> overlayer interatomic spacing is consistent with the rutile phase.

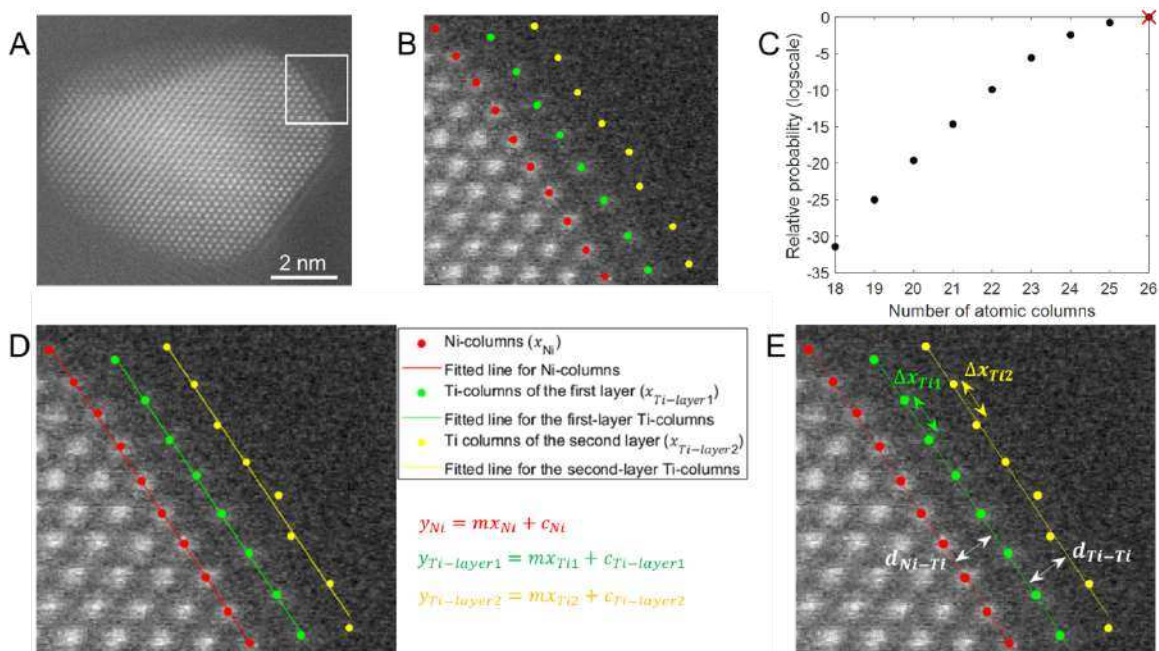


Fig. S14. A) ADF STEM image of a Ni NP in a Ni/TiO<sub>2</sub> catalyst in H<sub>2</sub> at 400 °C. Enlarged image of the area indicated by the white rectangle is given in (B). B) The refined positions of the Ni atomic columns at the surface, Ti atomic columns on the inner (green) and outer (yellow) layers. C) The MAP probability rule evaluated as a function of the number of columns. The most probable number of columns for the selected region of the image shown in (A) equals 26 and corresponds to the red cross. D) The estimated atomic column positions by the MAP probability rule and their corresponding linear regression models. E) Illustration of the different interatomic distances reported in Fig. S17.

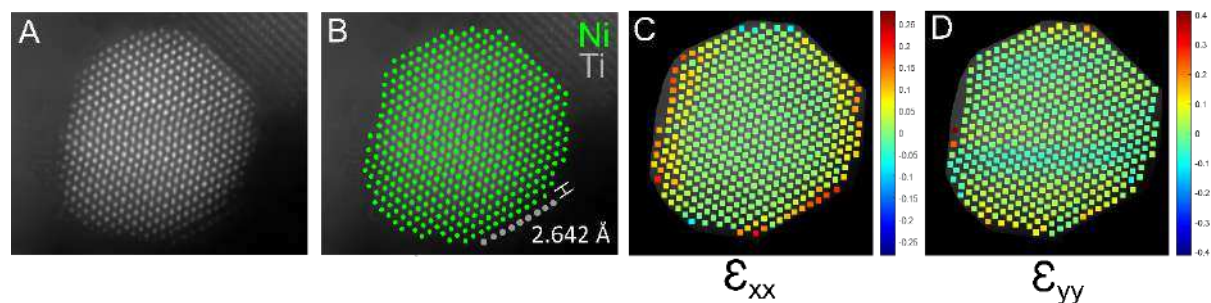


Fig. S15. (A) HAADF STEM imaging of a single Ni/TiO<sub>2</sub> particle from 400-Ni/TiO<sub>2</sub> in H<sub>2</sub> at 400 °C and atmospheric pressure. (B-D) shows the same particle as in (A) with atomic positions of Ni (green) and Ti (grey) in (B) and atomic strain maps in the x (C) and y (D) directions compared to an idealized Ni lattice.

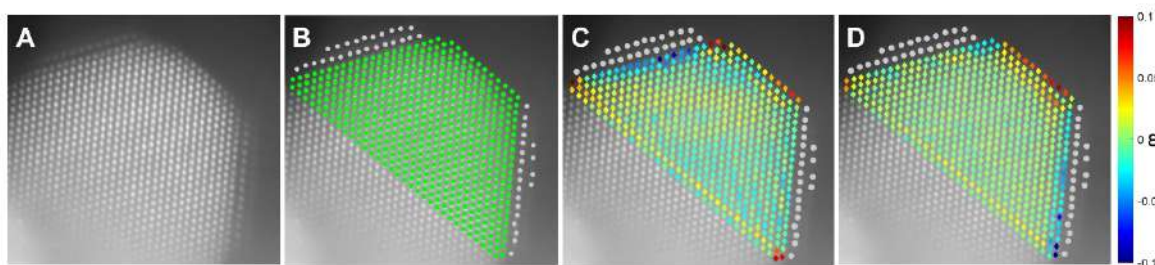


Fig. S16. (A) HAADF STEM imaging of a single Ni/TiO<sub>2</sub> particle from 400-Ni/TiO<sub>2</sub> in H<sub>2</sub> at 400 °C and atmospheric pressure. (B-D) shows the same particle as in (A) with atomic positions of Ni (green) and Ti (grey) in (B) and atomic strain maps in the x (C) and y (D) directions compared to an idealized Ni lattice.

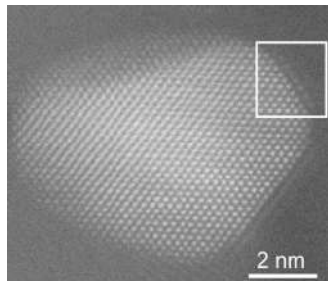
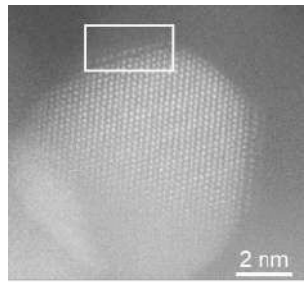
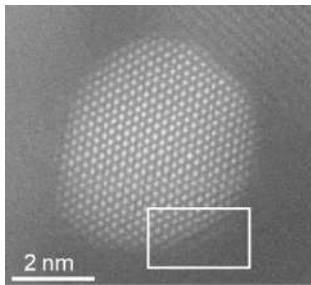
			
$d_{Ni-Ti}$ (Å)	$2.76 \pm 0.01$	$2.93 \pm 0.09$	$2.73 \pm 0.01$
$d_{Ti-Ti}$ (Å)	$2.82 \pm 0.02$	$2.95 \pm 0.01$	$2.77 \pm 0.02$
$\Delta x_{Ti1}$ (Å)	$2.73 \pm 0.05$	$2.82 \pm 0.04$	$2.53 \pm 0.08$
$\Delta x_{Ti2}$ (Å)	$2.78 \pm 0.13$	$2.89 \pm 0.07$	$3.21 \pm 0.29$

Fig. S17. HAADF STEM images of 400-Ni/TiO<sub>2</sub> NPs in H<sub>2</sub> (1 bar) and 400 °C with corresponding Ni-Ti and Ti-Ti interatomic distances extracted once the column positions were estimated by the MAP rule<sup>(25, 26)</sup>.

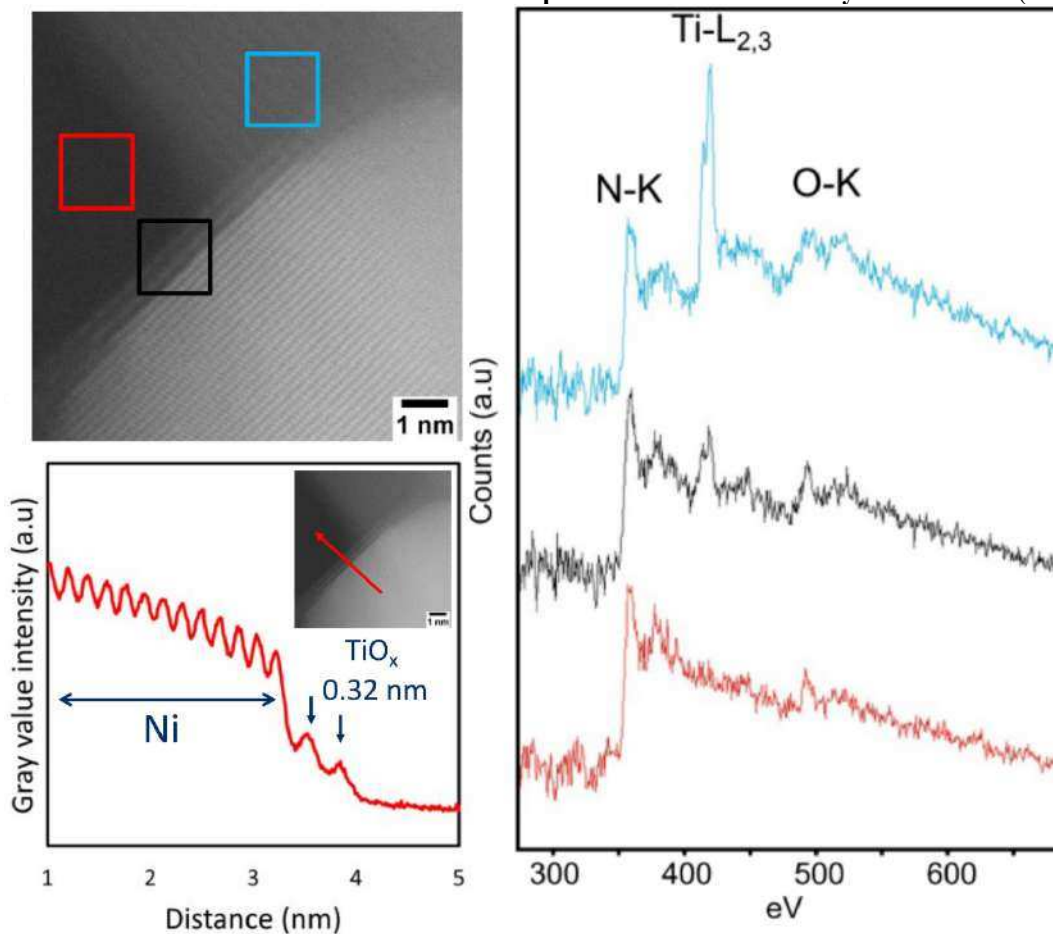
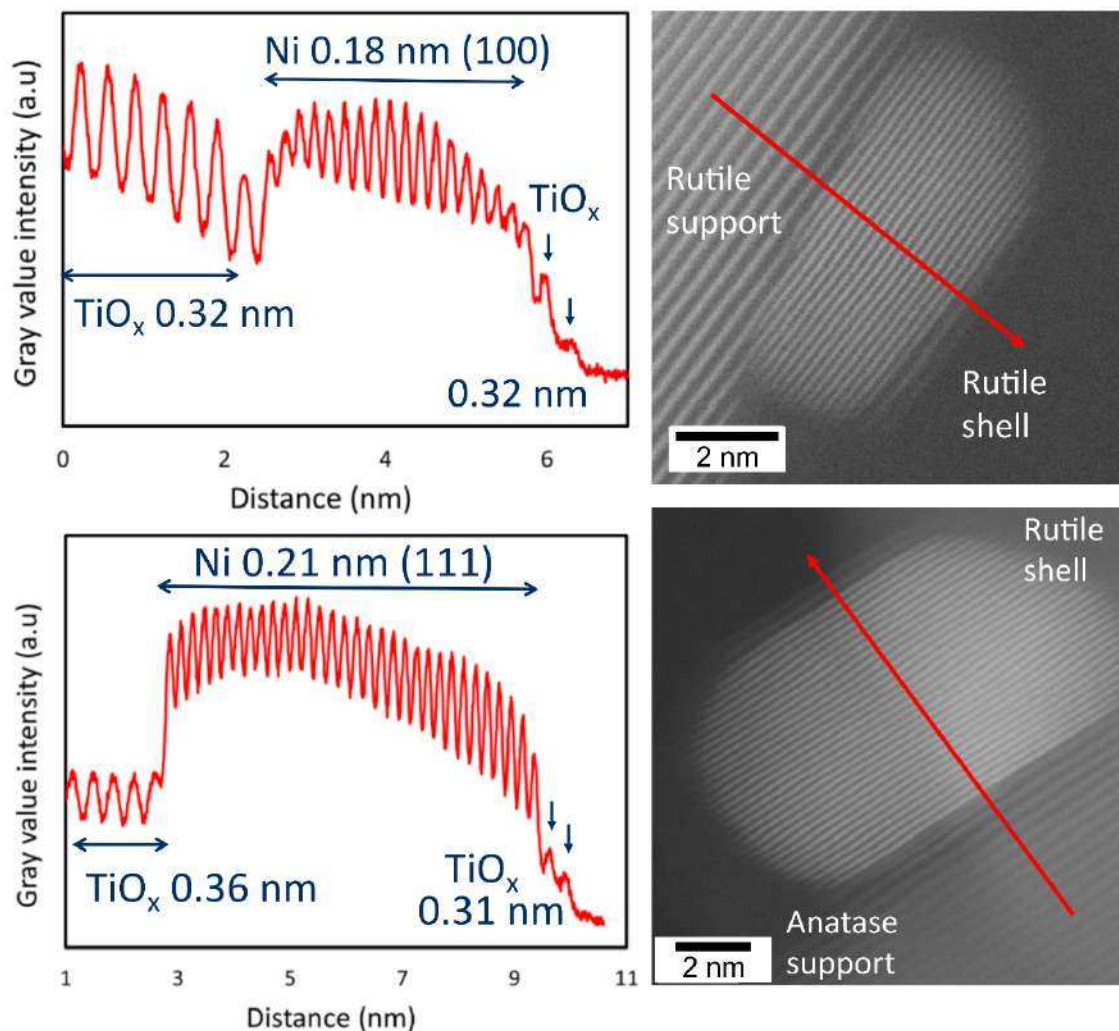


Fig. S18. Electron Energy-Loss Spectroscopy (EELS) chemical mapping evidencing atomic bilayer containing Ti on 400-Ni/TiO<sub>2</sub> re-reduced in situ. Top Left: HAADF STEM image showing the location of three EELS

spectra, where bulk  $\text{TiO}_2$  nanocrystal support (blue), bilayer upon Ni NP surface (black) and  $\text{Si}_3\text{N}_4$  window background (red) are compared. Right: the three compared EELS spectra showing a strong Ti-L<sub>2,3</sub> edge for the bulk  $\text{TiO}_2$  in addition to N and O K edges. The  $\text{TiO}_{2-x}$  overlayer also shows a clear Ti L<sub>2,3</sub> ionization edge, while the  $\text{Si}_3\text{N}_4$  background spectra show a clear N K and O K edge and absence of Ti L<sub>2,3</sub>. Left Bottom: gray scale intensity line scans over the particle showing the clear occupation of a  $\text{TiO}_{2-x}$  bilayer upon the Ni NP surface where interatomic spacing of the bilayer is consistent with the rutile structure.



**Fig. S19.** Atomic resolution HAADF STEM imaging evidencing phase independency between the  $\text{TiO}_{2-x}$  bilayer and  $\text{TiO}_2$  support on 400-Ni/ $\text{TiO}_2$  re-reduced in situ. Top: Ni metal NP upon a rutile support ( $d=0.32$  nm, Rutile (110)) with the same interatomic spacing found within the overlayer (0.32 nm). Bottom: Ni Metal NP upon an anatase support ( $d=0.36$  nm, anatase (110)) with a different interatomic spacing found within the overlayer (0.32 nm, rutile (110)).

#### Extended DFT Discussion

We first investigated whether the preferred formation of rutile layers on the Ni (111) surface could be due to compatibility of the 2D lattices of Ni and  $\text{TiO}_2$  facets. The match or lack of same of the Ni surfaces and the  $\text{TiO}_2$  layers is quantified as follows: for each of the (100), (110) and (111) surfaces we determined the minimal length axes of the 2D rectangular lattice. In general, to match these with the rectangular 2D lattice of the (110) rutile layer or the (101) anatase layer, the axes of both layers needed to be multiplied by integer factors to match to within a certain norm (we chose less than 3% deviation). As an indicator for the match, we used the area of the  $\text{TiO}_2$  superlattice required for the match. The larger this area, the worse the match between the nickel surface and titania layer. The results of matching is shown in the table below.



**Table S3. TiO<sub>2</sub>/Ni superlattice area calculation for TiO<sub>2</sub> rutile (110) and anatase (101) on different Ni surfaces (100), (110), (111).**

Ni	a [Å]	b [Å]	Ni surface superlattice			Rutile (110) superlattice			Area [Å <sup>2</sup> ]
(100)	2.495	2.495	6a,8	14.972	19.963	5a,3	14.790	19.450	288
)	4	4	b	7	6	b	6	1	
(110)	2.495	3.529	6a,9	19.963	17.645	3b,6	19.450	17.748	
)	4	1	b	6	5	a	1	7	345
(111)	2.495	4.322	6a,3	14.972	12.966	5a,2	14.790	12.966	192
)	4	2	b	7	7	b	6	7	
Ni	a [Å]	b [Å]	Ni surface superlattice			Anatase (101) superlattice			
(100)	2.495	2.495	3a,17b	7.4863	42.422	2a,4b	7.5704	41.487	314
)	4	4			6			6	
(110)	2.495	3.529	3a,6b	7.4863	21.174	2a,2b	7.5704	20.7438	
)	4	1			6				157
(111)	2.495	4.322	3a,7b	7.4863	30.255	2a,3b	7.5704	31.1157	236
)	4	2			7				

Based on the match (or lack of same) observed for the rutile (110) overlayers we offer a tentative explanation why these are formed on the Ni (111) surface and not on the other two low index surfaces: smaller superlattices are required. Note that the matching does not explain why no anatase overlayers are formed: the anatase (101) superlattice on Ni(110) would be the smallest of all. However, we note that anatase is less thermodynamically stable than rutile. Another question to be addressed is that of the nature of the interface between the Ni (111) surface and the rutile layers. As only the metal atoms are observed, we based ourselves on the (average) distance between the last Ni and the first Ti layer of 2.73-2.93 Å, observed by TEM (Fig. S17).

Two models initially suggested themselves:

1. Two rutile layers covering the bare Ni (111) surface
2. Additional O atoms are present on the Ni surface such that the bonding between the Ni and Ti layers is the same as between two Ti (110) layers

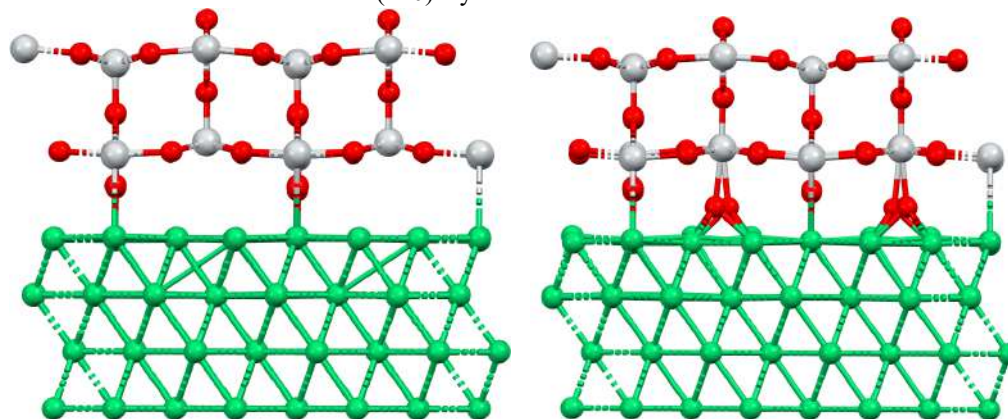


**Fig. S20. Computed structures of Ni (111) covered by rutile layers (model 1, left) and by both rutile layers and extra O atoms to make the bonding between Ni and rutile layers similar to the bonding between successive Ti layers (model 2, right).**

These calculations were done in a unit cell of 14.9727 by 12.967 by 25 Å, as per the lattice matching above and with sufficient vacuum between successive slabs in the z-direction, with a 2x3x1 k-point mesh. For models 1 and 2, we found an average distance between the upper Ni and lower Ti layer of 3.21 and 3.20 Å, respectively, which is too long to be commensurable with the distance experimentally measured by TEM. This suggest that other elements than O

are involved in the interface between Ni and Ti. The only reasonable alternative for O under the gas atmosphere used during reduction is H. Therefore, we also did computations on the following two models:

3. As 1, but with the lowest O sublayer of the Rutile layers (bridging between Ti atoms) replaced by an H sublayer.
4. As 3, but with additional H on the surface, analogous to the additional O atoms in 2.

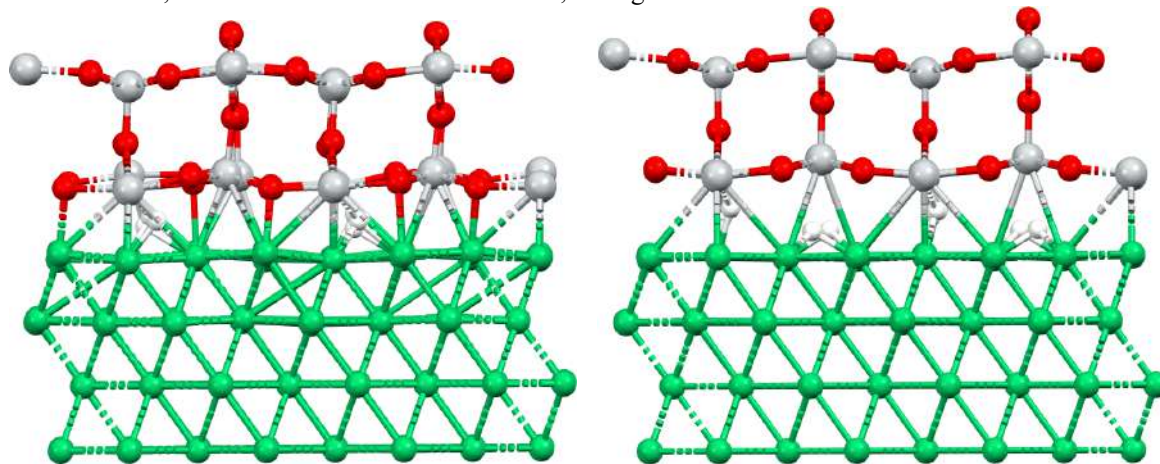


**Fig. S21. Computed structures of Ni (111) covered by  $\text{Ti}_4\text{O}_7\text{H}$  layers (model 3, left) and by both  $\text{Ti}_4\text{O}_7\text{H}$  layers and extra H atoms (model 4, right).**

Model 3 led to a Ni–Ti layer distance of 2.42 Å, while for model 4 the Ni–Ti distance was 2.79 Å. Model 4 thus comes closest to the observed Ni–Ti distance observed by TEM (Fig. 1). Based on these calculations, it appears unlikely that fully formed  $\text{TiO}_2$  rutile overlayers are present on the Ni (111) surface, so the overlayers are most likely a suboxide phase. H atoms may have replaced the lowest O sublayer, with additional H on the surface.

In the hopes that we could find a thermodynamic reason for the absence of rutile overlayers on other low index surfaces we also did a calculation of model 4 applied to the Ni (100) surface, using a unit cell of 14.9727 by 12.967 by 25 Å and a 2x3x1 k-point mesh. For reference, we computed the energy of two layers of rutile, with the lowest O sublayer replaced by H. The equilibrium unit cell had axes of 2.9146 and 6.4438 Å (the third axis was fixed at 20 Å). A 6x3x1 k-point mesh was used. For H we used the  $\text{H}_2$  molecule as reference.

We computed a stabilization energy by taking the energy of model 4, and subtracting the energy of the (geometry optimized) bare surface slab, the reference energy of the  $\text{Ti}_4\text{O}_7\text{H}$  units as well as the reference energy of the additional H atoms at the surface, and normalized that by dividing by the number of Ti atoms in the structure. This yielded stabilization energies of -38.9 kJ/mol for the (111) and -61.6 kJ/mol for the (100) surface. Based on these results, we cannot explain the preference of rutile overlayers on the (111) surface observed by TEM by thermodynamic arguments alone. Since the overlayers appear thermodynamically stable, forming rapidly (s-min scale) at high temperature, and since they do not evolve over time (hours), we believe that the current model does not yet describe the exact nature and structure of the Ni/ $\text{TiO}_x$  interface. Nonetheless, we can conclude that the observed  $\text{TiO}_x$  overlayers are formed on the Ni surface which allows for the lowest lattice mismatch (Table S3), which minimizes strain. Thus, we have a geometrical descriptor for the formation of the overlayers, while describing electronic stabilization effects and the overall thermodynamics of the system requires further studies.

Note that whether or not the rows of Ti in rutile are right above each other depends on the viewing angle, as depicted in Fig. S22 below.

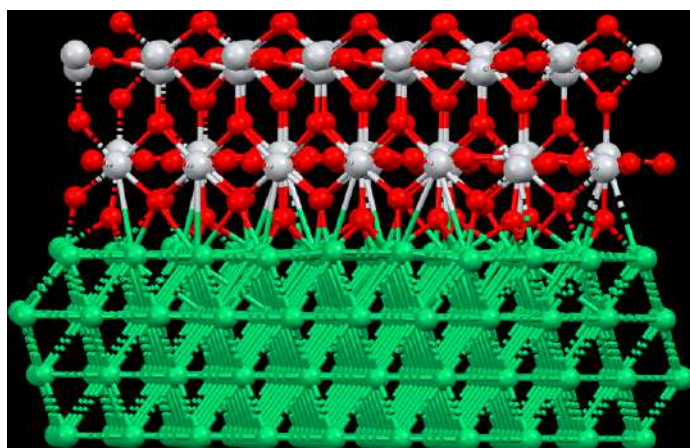


**Fig. S22. Computed structure of Ni (111) as in model, seen from a slightly tilted angle so that the Ti atoms are alternating similarly to what observed in Fig. 1.**

In a subsequent step, we allowed the unit cell to relax in the two directions parallel to the slab for models 1-4 on the Ni(111) surface, as well as the bare Ni(111) slab, keeping only the z coordinates of the atoms in the two bottom Ni layers fixed. We also computed unit cell constant of bulk Ni using the same basis set and other numerical approximations as in the slab calculations (using 14x14x14 k-points), so we can compare the unit cell vectors of the slabs with those of the pure cutting plane. The results are given in Table S4 below. Model 4 gives the most significant contraction of the surface area and is therefore most commensurable with the experimental observation of compressive strain. Note that the bare Ni(111) slab shrinks even more, so putting on the Ti layers relieves some of the strain.

**Table S4. Axis length of the unit cell vectors of the modelled slabs when allowing the unit cell to relax in the two directions parallel to the slabs for models 1-4 on the Ni(111) surface, and relative change with respect to a non-relaxed Ni(111) cutting plane**

	Axis length [ $\text{\AA}$ ]		change	
	a	b	a	b
Ni(111) cutting plane	14.8491	12.8597		
Ni(111) slab	14.7061	12.7526	-0.96%	-0.83%
Model 1	14.7470	12.8757	-0.69%	0.12%
Model 2	14.8206	12.9085	-0.19%	0.38%
Model 3	14.7986	12.8617	-0.34%	0.02%
Model 4	14.7632	12.8448	-0.58%	-0.12%

In Table S5 we give the computed distances between successive metal (oxide) layers. Since the z coordinates of the bottom two layers of Ni were fixed, for Ni-Ni we only show the distances between layers 2 and 3 as well as 3 and 4. The Ni(4)-Ti distance is but little affected by the expansion of the unit cell. We find the best fit with experiments for model 4, while for all models Ni-Ni interlayer distances are in reasonable agreement with experiment. All models show a computed Ti-Ti interlayer distance which is much larger than experimentally observed (see Fig. 1). This suggests that the oxygen sublayer structure between successive Ti layers is not exactly as in perfect rutile. This might be due to oxygen vacancies or hydrogen at oxygen positions. Note that substituting H for O causes the Ni(4)-Ti interlayer distance to shrink from 3.228 Å to 2.795 Å upon going from model 2 to model 4.

**Table S5. Computed distances between successive metal (oxide) layers for the modelled relaxed slabs.**

	Interlayer distances [Å]			
	Ni(2)-Ni(3)	Ni(3)-Ni(4)	Ni(4)-Ti	Ti-Ti
Model 1	2.012	2.016	3.243	3.278
Model 2	2.012	2.016	3.228	3.278
Model 3	2.016	2.034	2.447	3.237
Model 4	2.010	2.036	2.795	3.267

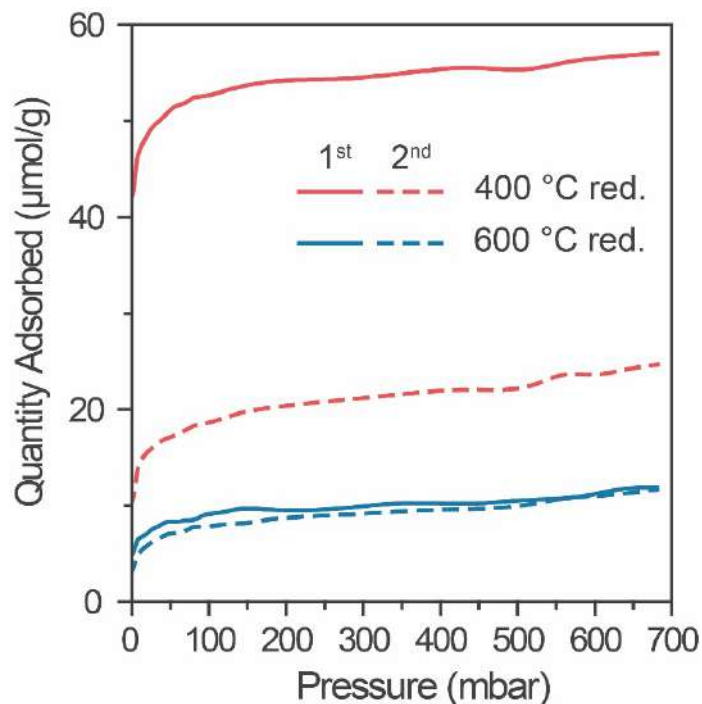


Fig. S23. First and second cycle  $\text{H}_2$  chemisorption isotherms on  $\text{Ni/TiO}_2$  pre-reduced at  $400\text{ }^\circ\text{C}$  and  $600\text{ }^\circ\text{C}$ .

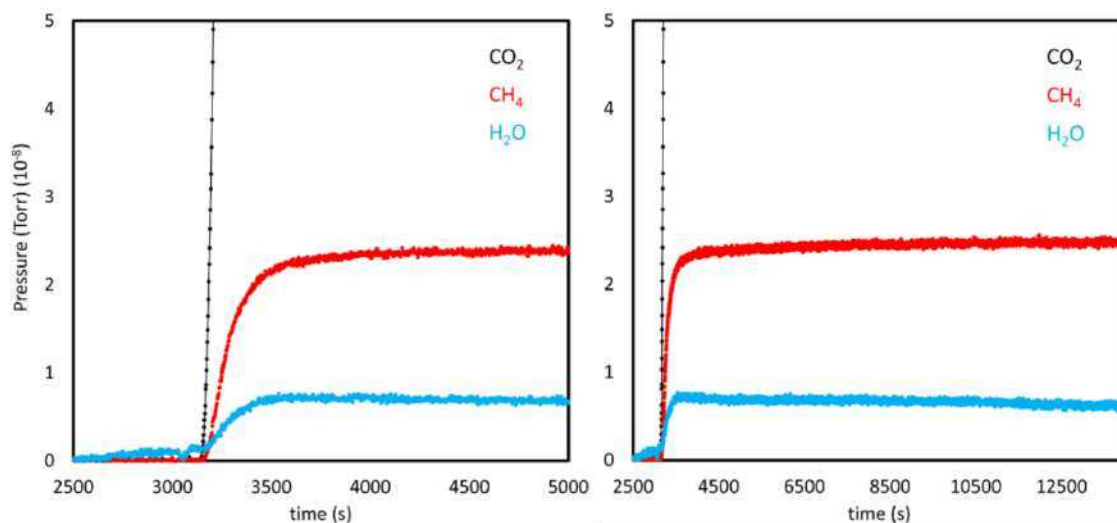
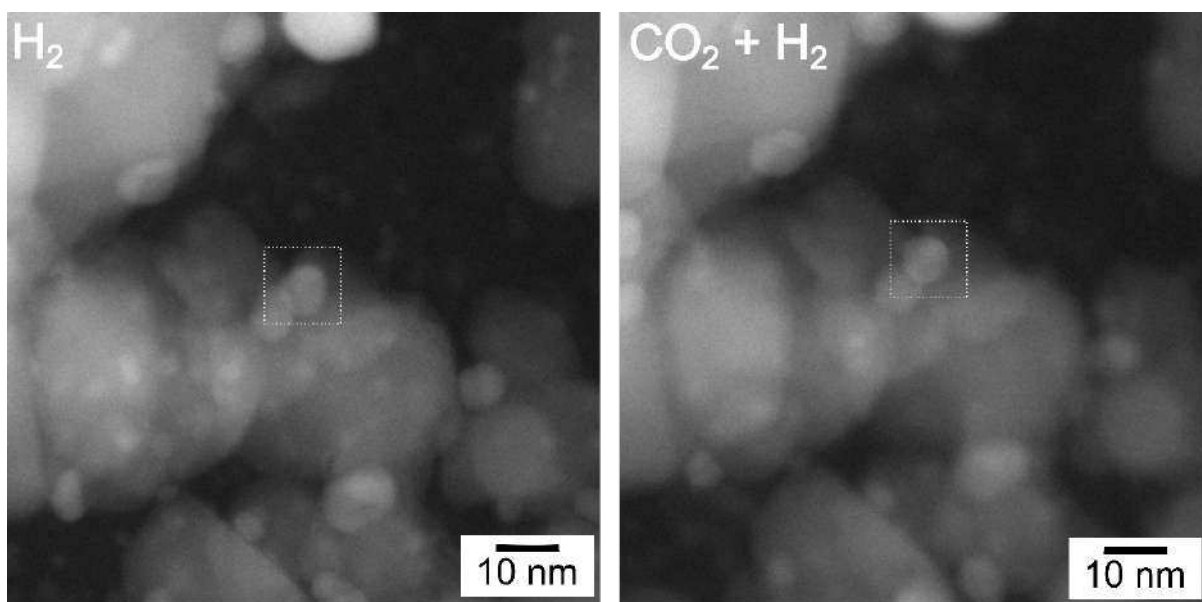
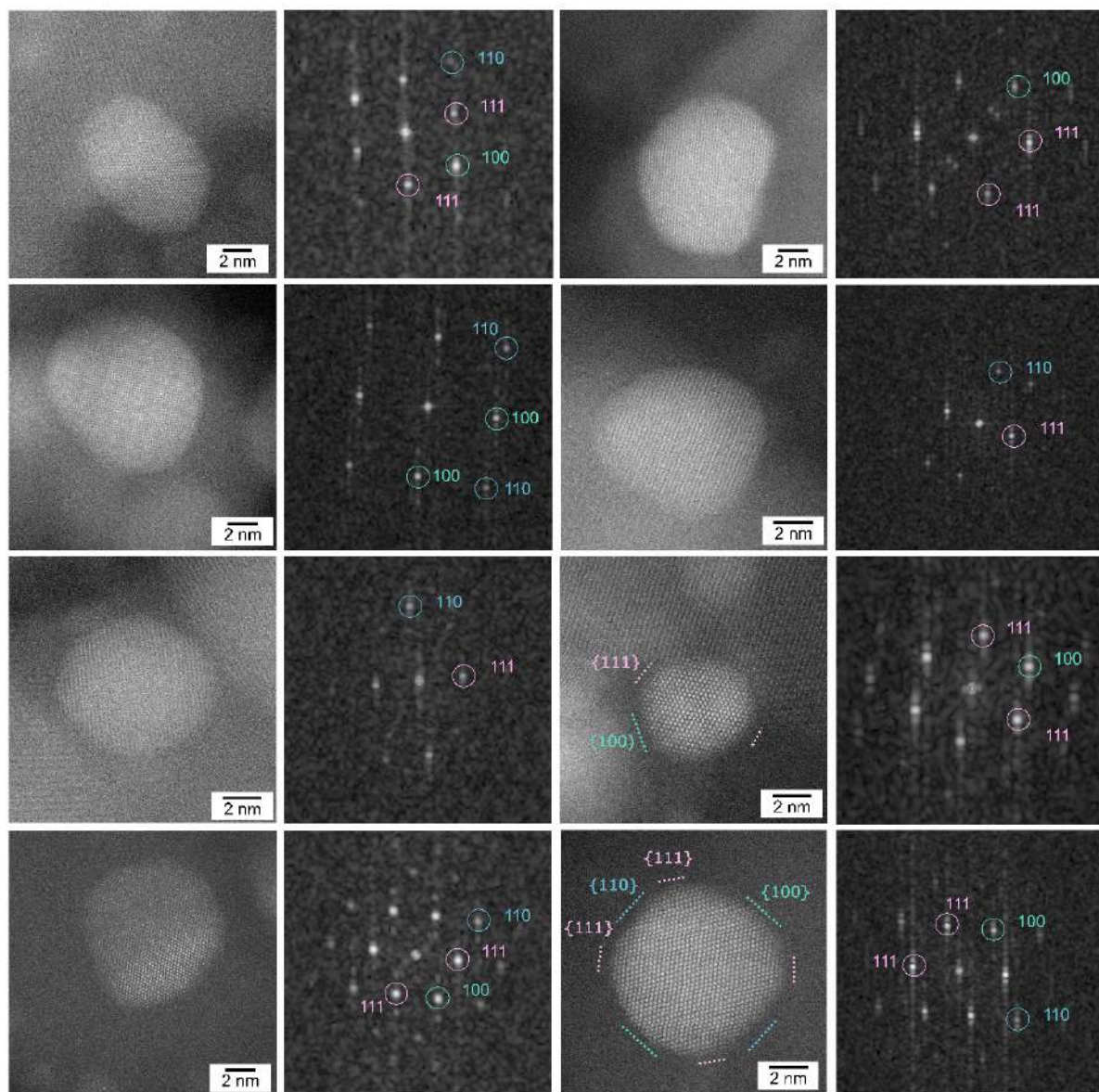


Fig. S24. Mass spectrometry data obtained by a dedicated gas analyzer attached to the windowed gas cell at the point of  $\text{CO}_2 + \text{H}_2$  introduction for  $400\text{-Ni/TiO}_2$  catalyst prepared in situ.  $\text{CO}_2$  (Black),  $\text{CH}_4$  (red) and  $\text{H}_2\text{O}$  (blue). Left: 2500-5000 s; right: 2500-14500 s of experiment time.



**Fig. S25.** Low magnification operando HAADF STEM images of 400-Ni/TiO<sub>2</sub> NP prepared in situ and shown in Fig. 3, with a clearly faceted structure in H<sub>2</sub> environment and more rounded structure during CO<sub>2</sub> hydrogenation.



**Fig. S26.** Atomic resolution and operando HAADF STEM images of 400-Ni/TiO<sub>2</sub> catalyst prepared in situ, during exposure to CO<sub>2</sub> hydrogenation conditions. Images show the conservation of Ni oxidation state during CO<sub>2</sub> hydrogenation and the generation of a more rounded structure and absence of TiO<sub>2-x</sub> overlayer.

**Table S6. Thermodynamically stable Ti<sub>2</sub>O<sub>3</sub> amount (%) under CO–CO<sub>2</sub> hydrogenation conditions (CO<sub>2</sub>:CO:H<sub>2</sub> = 3:1:7, 4 bar), as a function of temperature.**

T (°C)	Ti <sub>2</sub> O <sub>3</sub> (%)
200	1.01E-13
220	6.03E-13
240	3.14E-12
260	1.45E-11
280	6.01E-11
300	2.25E-10
320	7.74E-10
340	2.45E-09
360	7.23E-09
380	2E-08
400	5.19E-08
420	1.28E-07
440	2.99E-07
460	6.7E-07
480	1.44E-06
500	2.99E-06
520	6.01E-06
540	1.17E-05
560	2.24E-05
580	4.17E-05
600	7.62E-05

Equilibrium calculations were performed using the HSC Chemistry 9.1 software in the *Gem equilibrium composition* module, by the Gibbs free energy minimization method. The table shows that the TiO<sub>2</sub> to Ti<sub>2</sub>O<sub>3</sub> reduction equilibrium shifts back to TiO<sub>2</sub> under reaction conditions, with the highest Ti<sub>2</sub>O<sub>3</sub> percentage in the range 200–400 °C being in the order of 10<sup>-8</sup> %. This explains the observation that thin TiO<sub>x</sub> overlayers formed after 400 °C reduction are removed from the Ni surface when switching to CO<sub>2</sub> hydrogenation conditions (Fig. 1). On the other hand, thicker overlayers formed after 600 °C reduction were not removed, and instead restructured, as shown in Figs. 2 and 3. This can be explained by the fact that metastable TiO<sub>2-x</sub> may still exist due to kinetics effect, or by the reoxidation to TiO<sub>2</sub> which is still anchored on the Ni surface.



### XPS results

In order to determine the Ni and Ti 2p core level areas we take advantage of a fitting model that allows us to utilize the acquired background for improved statistics. Specifically, we calculate the Shirley background analytically from the fitted peak functions (65) and include the extrinsic contributions via an approximation to the Tougaard background. (66) An analytical approximation to the Voigt function is used to facilitate the calculation. (67) A fitting model using two and four Voigt doublets is used for the Ti and Ni 2p core levels, respectively. We employ genetic algorithms with a simple roulette wheel selection for the fitting routine in order to avoid local minima generated by the background functions. We assume the oxidation state of the cations to be constant and converge the fitting model so that it can describe all our spectra. Thus, to determine the area of the curves we are left only with four parameters: an intensity, an energy offset, Gaussian width and the scattering constant for the extrinsic background. The Gaussian width is left as a parameter, since the resolution of the AP-XPS experiment depends on composition of the atmosphere. The scattering constant of the extrinsic background allows our model to capture the decline of the intensity at the high-binding energy side of the spectra (i.e., as opposed to a simple Shirley background that converges to a constant).

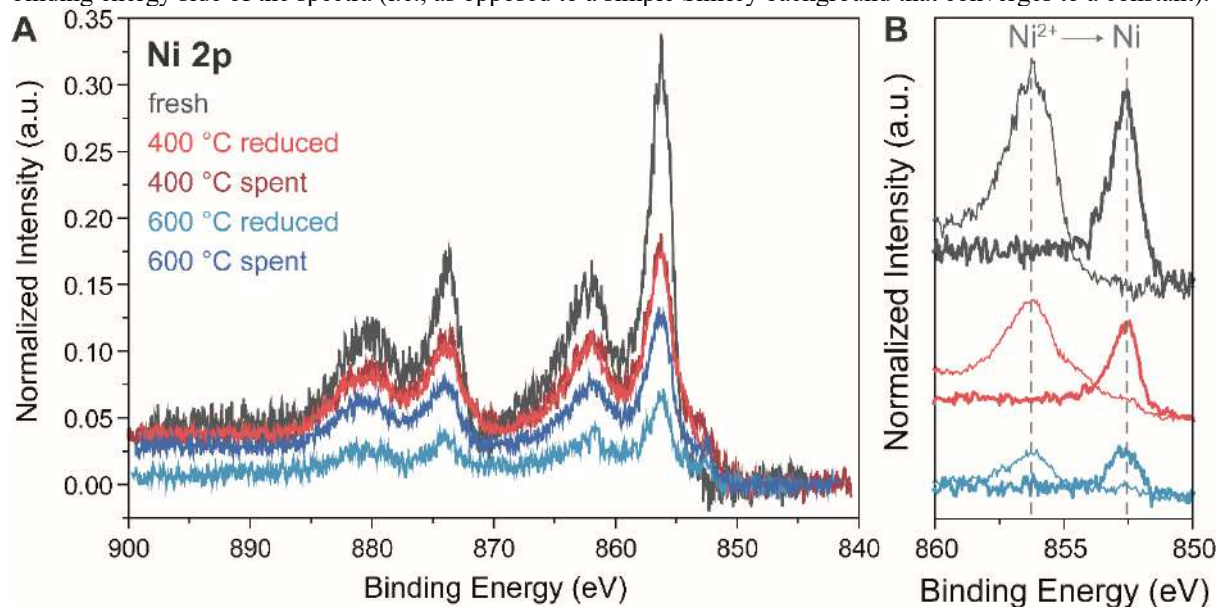


**Fig. S27.** Nickel encapsulation by TiO<sub>x</sub> overlayers revealed by Near-Ambient Pressure-X-ray Photoelectron Spectroscopy ((NAP)-XPS): (A) Ni 2p region of the XPS spectra of fresh, reduced and spent Ni/TiO<sub>2</sub> catalysts under UHV conditions, normalized to Ti 2p signal, after air passivation, showing different overall intensity in accordance with overlayer formation. (B) Detail of Ni 2p NAP-XPS spectra for the fresh and the pre-reduced catalysts under 0.3 mbar H<sub>2</sub> at 350 °C (thick lines) compared to the UHV spectra, showing the appearance of metallic Ni signal and thus suggesting availability to the gas phase.

To estimate the signal variation that would be obtained by the removal/formation of a TiO<sub>2</sub> bilayer 30 % of a Ni particles surface (i.e., the facet-selective encapsulation observed in the TEM experiments), we performed numerical simulations using SESSA 2.2 assuming hemispherical Ni metal NPs on a flat TiO<sub>2</sub> substrate (68). The resulting simulated variation of the Ni 2p / Ti 2p ratio is  $10 \pm 3$  %. We note that while we only observe a  $\sim 1$  % variation in our experiment (Fig. S28), there are two factors that make the numerical model overestimate the value. First, there is still a significant pressure gap between the NAP-XPS and TEM experiments. Second, the IMFP, an important input in the simulations, is poorly defined in the low-dimensional case of the TiO<sub>2</sub> bilayer. Specifically, the number of empty states normal to the surface is typically significantly reduced at the low-dimensional limit, closing available scattering channels and increasing the IMFP.

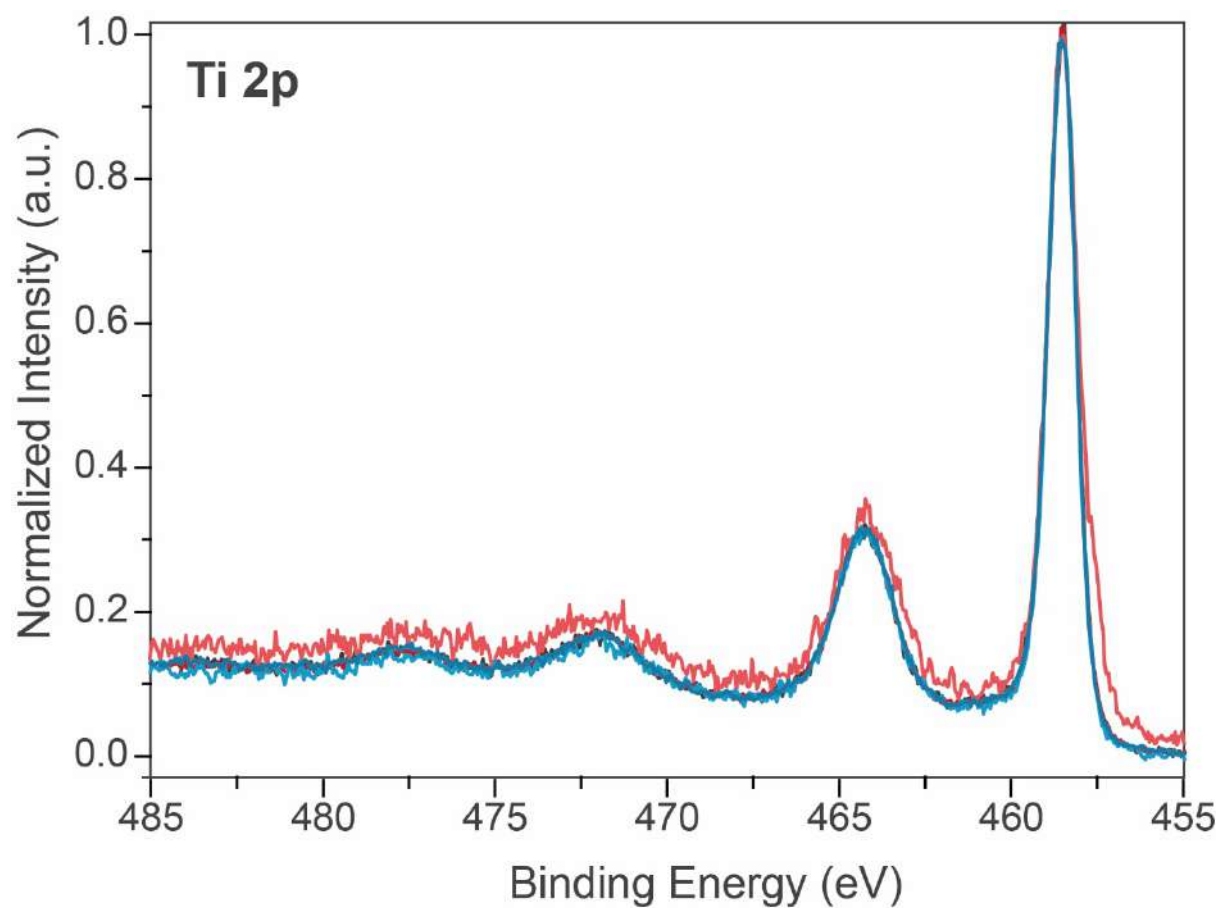
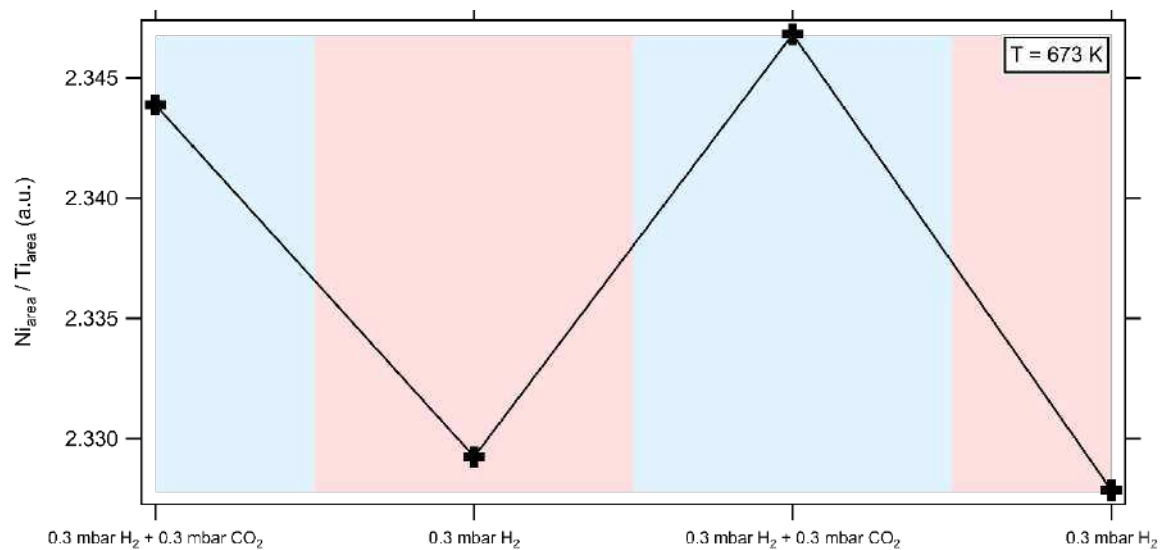
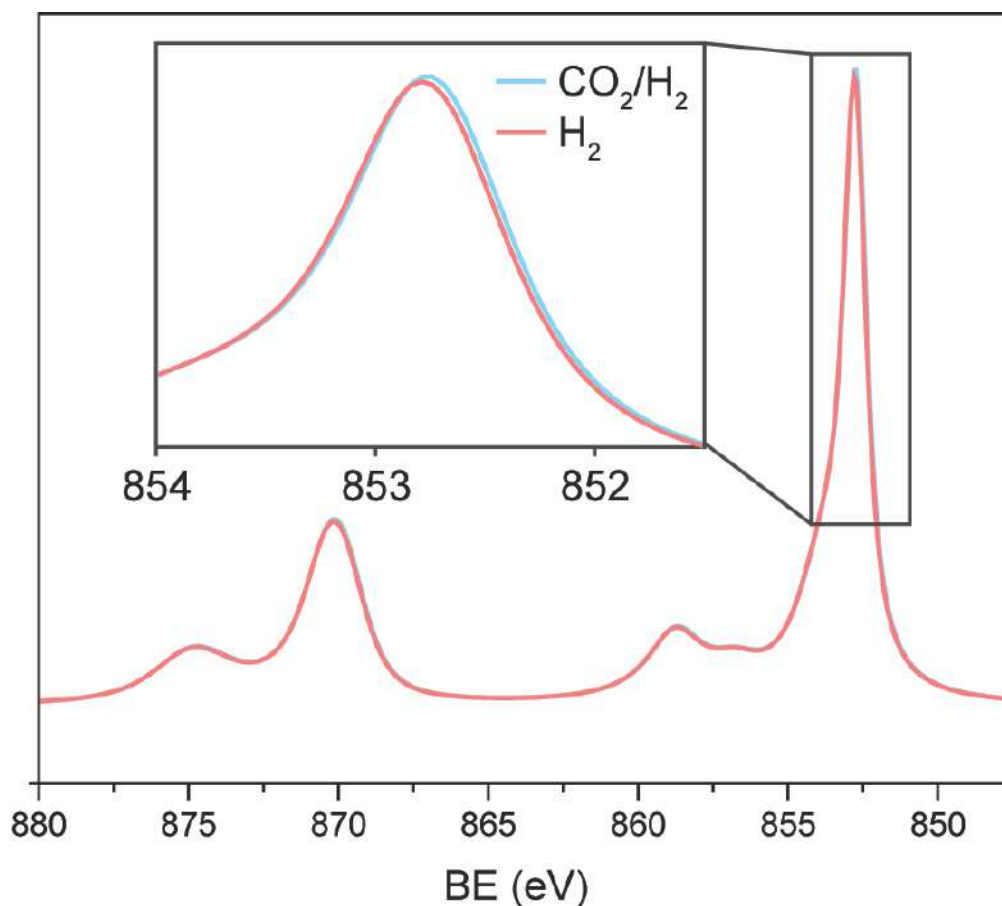
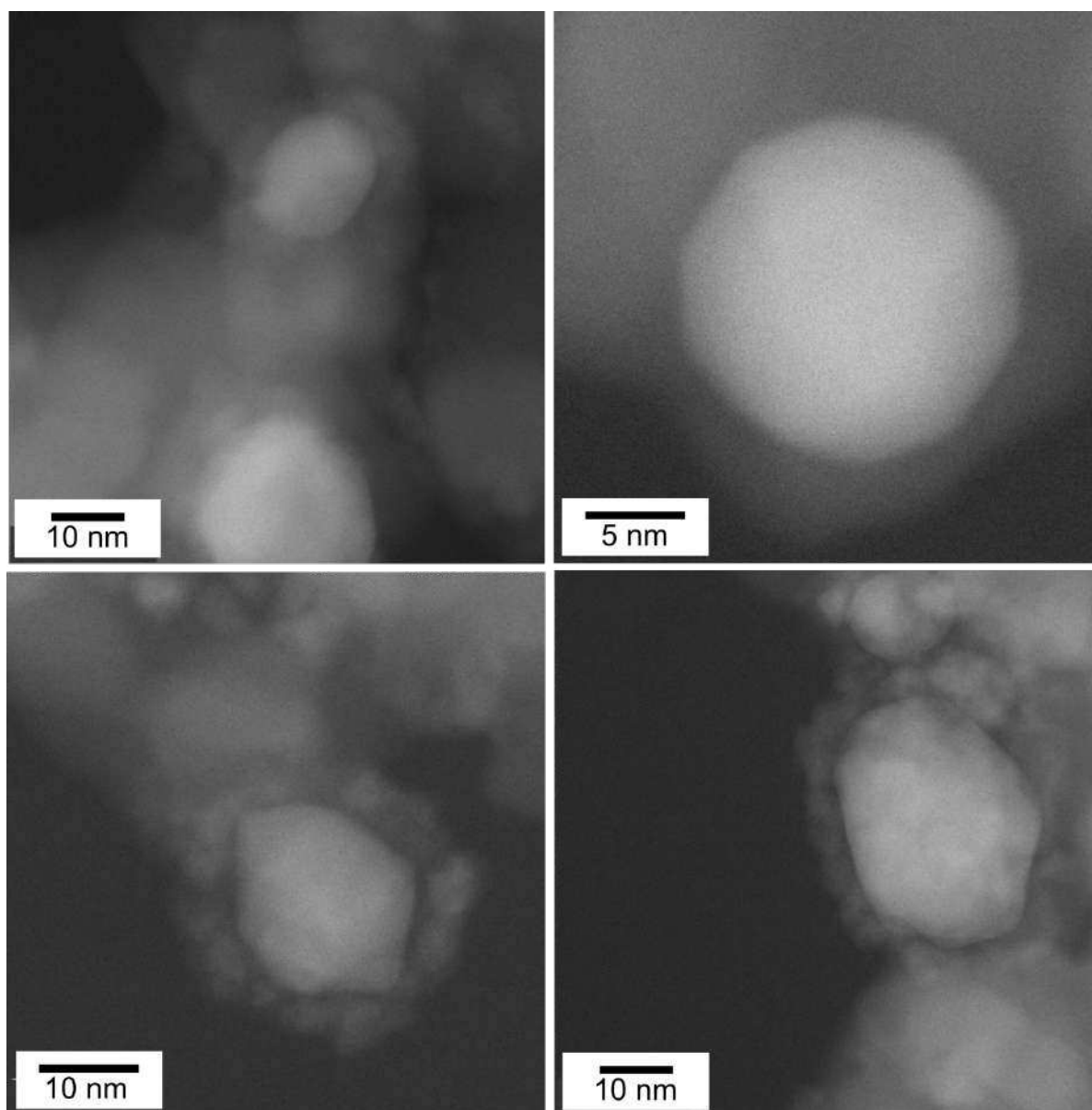


Fig. S28. X-ray Photoelectron Spectroscopy (XPS) of the Ti 2p spectral region under Ultra-High Vacuum (UHV) for the fresh (black), 400 °C reduced (light red) and used (dark red), and 600 °C reduced (light blue) and used (dark blue) catalyst materials after air passivation.





**Fig. S29. (Top) Ratio of Ni 2p/Ti 2p signal areas ( $Ni_{area}/Ti_{area}$ ) during the Near Ambient Pressure-X-ray Photoelectron Spectroscopy (NAP-XPS) experiments at 400 °C. The sample was cycled between 0.3 mbar H<sub>2</sub>/0.3 mbar CO<sub>2</sub> and 0.3 mbar H<sub>2</sub> to probe the reversibility of the TiO<sub>x</sub> overlayer formation and removal, which can be observed by a decrease and increase in the  $Ni_{area}/Ti_{area}$  during reduction and reaction, respectively. While the amplitude of oscillation is quite small (1 % of signal), this is robust against methods the areas are determined by. (Bottom) A visual representation of the ratio variation via the results of the applied fitting model, as described in the SI.**



**Fig. S30. HAADF STEM images of 600-Ni/TiO<sub>2</sub> prepared in situ showing thick TiO<sub>2-x</sub> overlayers prepared at high temperature.**

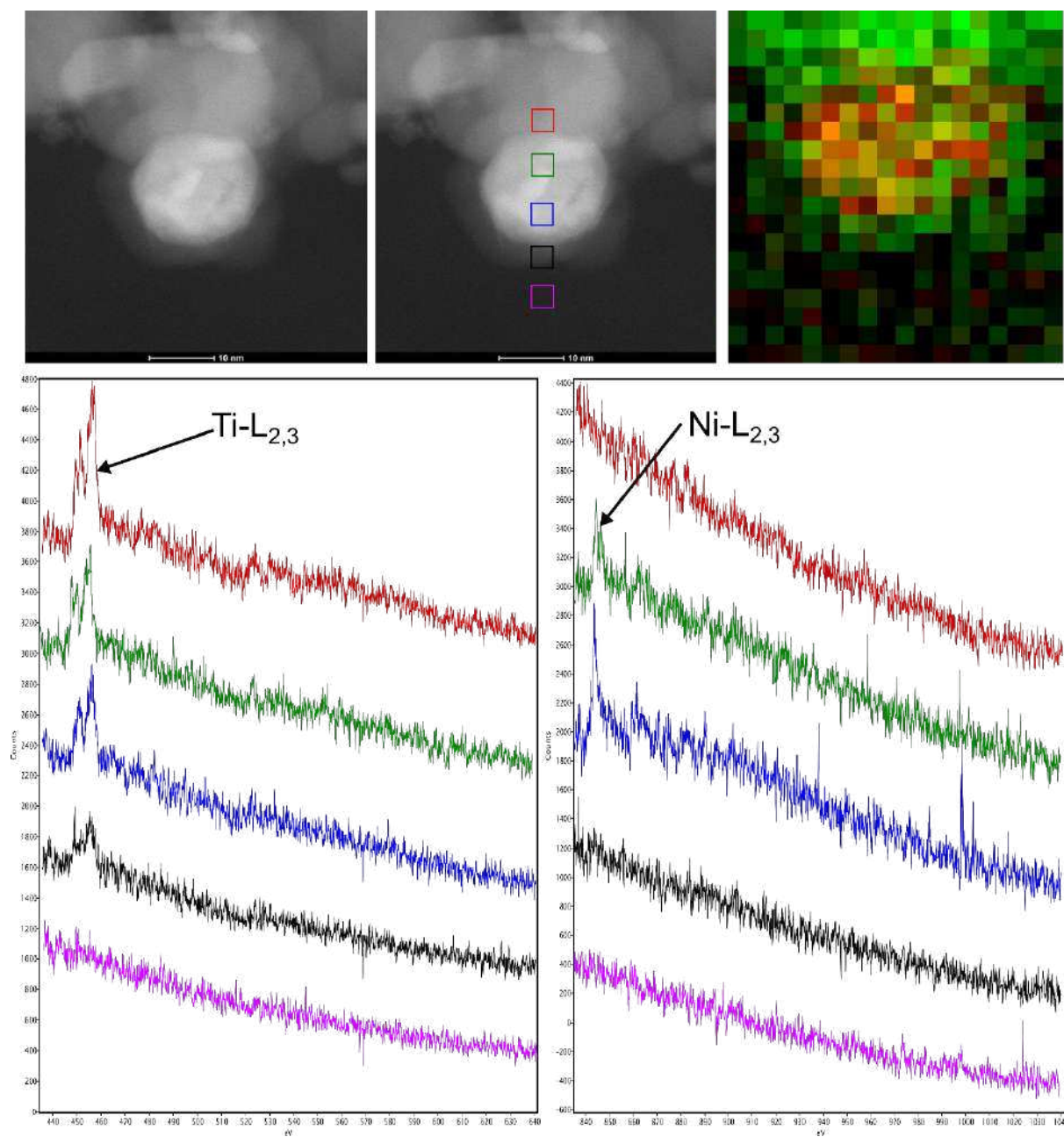


**Fig. S31. Electron Energy-Loss Spectroscopy (EELS) evidence for an overlayer consisting of Ti by chemical mapping on 600-Ni/TiO<sub>2</sub> prepared in situ. Top left and middle: HAADF STEM images showing the Ni NP measured (left) and locations of EELS spectra compared (middle). Right: extracted elemental distribution maps showing Ni (red) and Ti (green). Bottom: EELS spectra of Ti L<sub>2,3</sub> (left) and Ni L<sub>2,3</sub> (right) ionization edges clearly showing Ni edges exclusively at the region of the brighter particle, whereas the Ti signal is found on the Ti support, at the same location as the Ni NP (green and blue spectra) and also at the edge of the Ni NP (black). These data confirm that the darker shell surrounding the Ni NP corresponds to a Ti-based overlayer and also that the overlayer is completely encapsulating the Ni NP due to a clear Ti signal found over the entire Ni NP.**

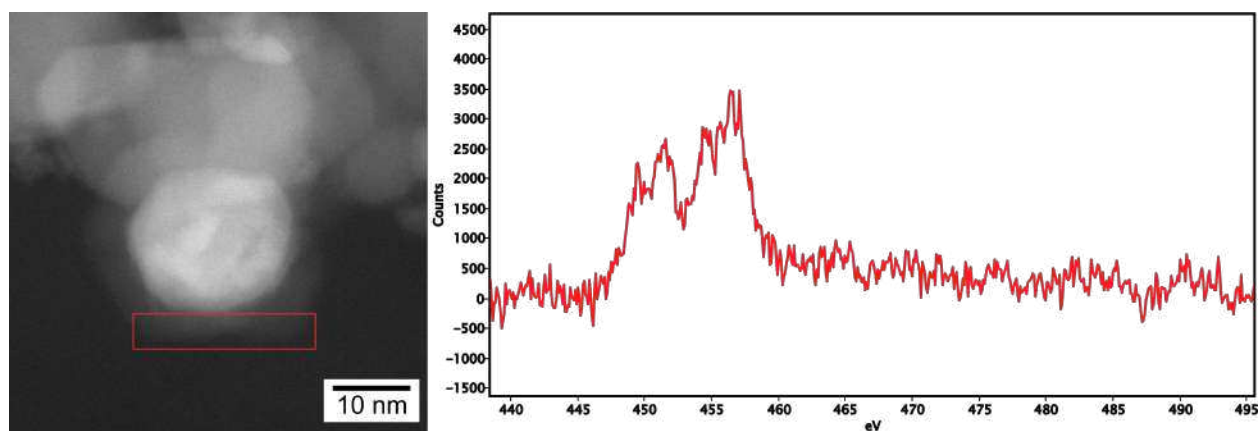


**Fig. S32.** In-situ Electron Energy-Loss Spectroscopy (EELS) evidence from the same encapsulated nanoparticle shown in Fig. 2 for an overlayer consisting of Ti upon an alternative Ni nanoparticle by chemical mapping on 600-Ni/TiO<sub>2</sub>. Left: HAADF STEM image showing the Ni NP measured and an annotation to show the location of TiO<sub>x</sub> shell where the corresponding EELS spectrum was summed in a similar manner to ref. (12). Right: EELS spectrum showing the summed Ti L<sub>2,3</sub> ionization edge with a sufficient signal-to-noise to display a fine structure consistent with a predominantly Ti<sup>4+</sup> ions (i.e., TiO<sub>2</sub>) (13).

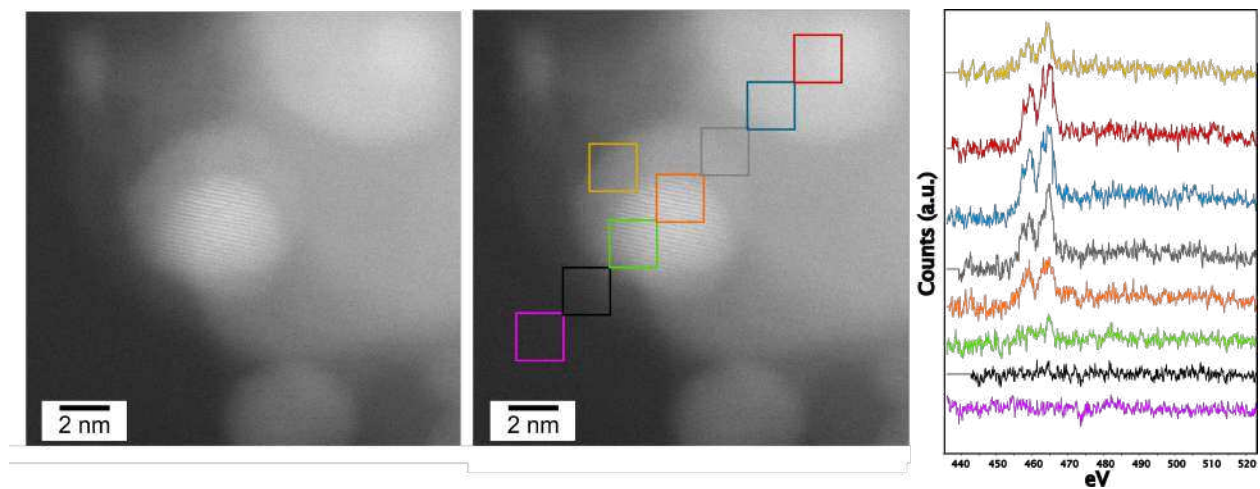


**Fig S33.** In-situ Electron Energy-Loss Spectroscopy (EELS) evidence for an overlayer consisting of Ti upon an alternative Ni nanoparticle by chemical mapping on 600-Ni/TiO<sub>2</sub>. Left, middle: HAADF STEM image showing the Ni NP measured (left) and locations of EELS spectra compared (middle). Right: spectra of Ti L<sub>2,3</sub> ionization edges clearly showing the Ti signal is found on the Ti support, at the same location as the Ni NP (green and orange spectra) and also at the edge of the Ni NP (yellow). These data confirm that the darker shell surrounding the Ni NP corresponds to a Ti-based overlayer.

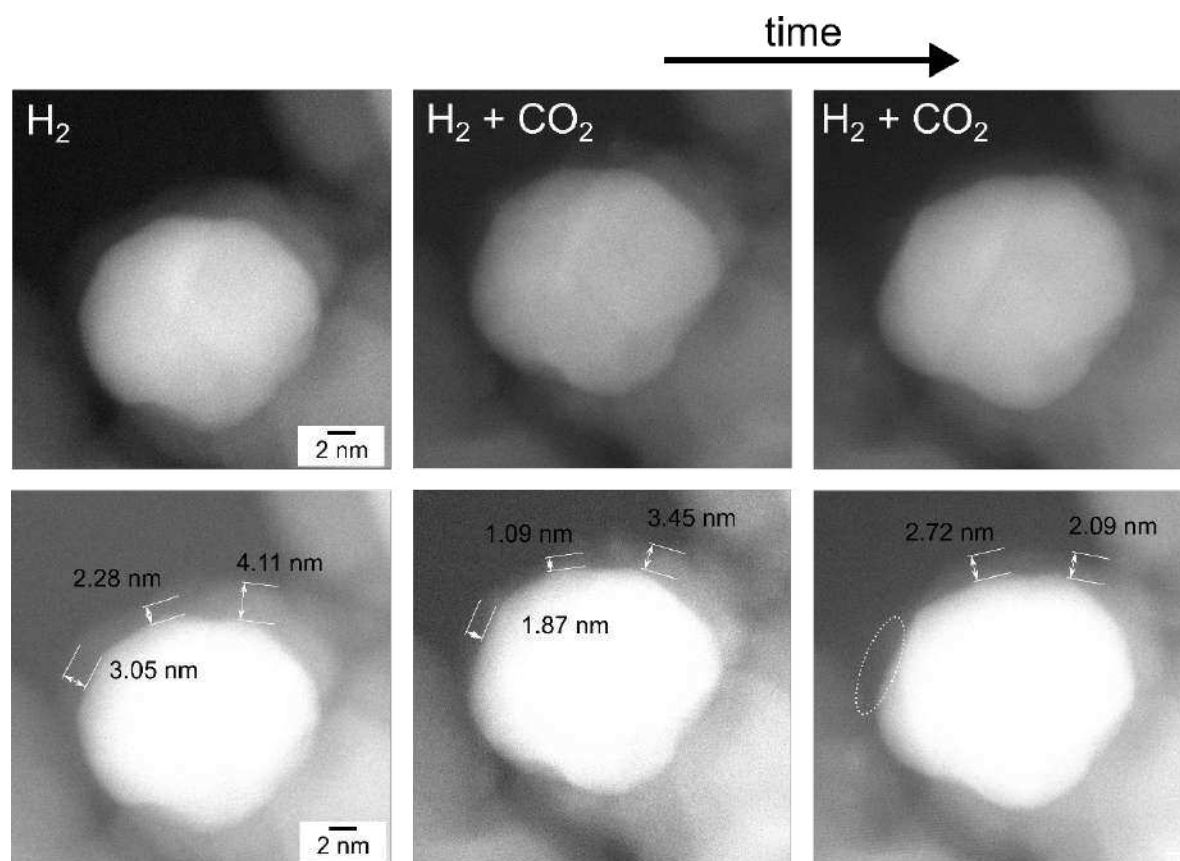


Fig. S34. (top) HAADF-STEM images of Ni/TiO<sub>2</sub> catalyst prepared in situ at 600 °C (600-Ni/TiO<sub>2</sub>) before reaction in H<sub>2</sub> (left) and during CO<sub>2</sub> hydrogenation conditions (middle–right) as shown in Fig. 2. (bottom) The same HAADF-STEM images as shown above, with an increased contrast to more clearly show the SMSI overlayer. Annotations show the changing overlayer thickness with time, and the circle identifies an area of exposed Ni surface.

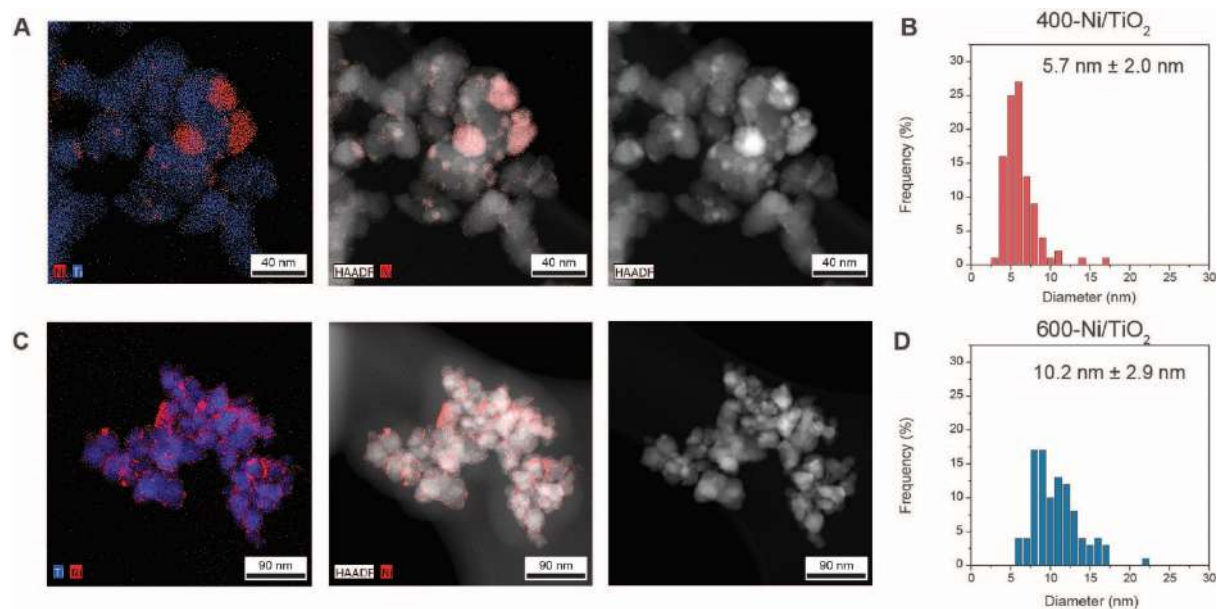
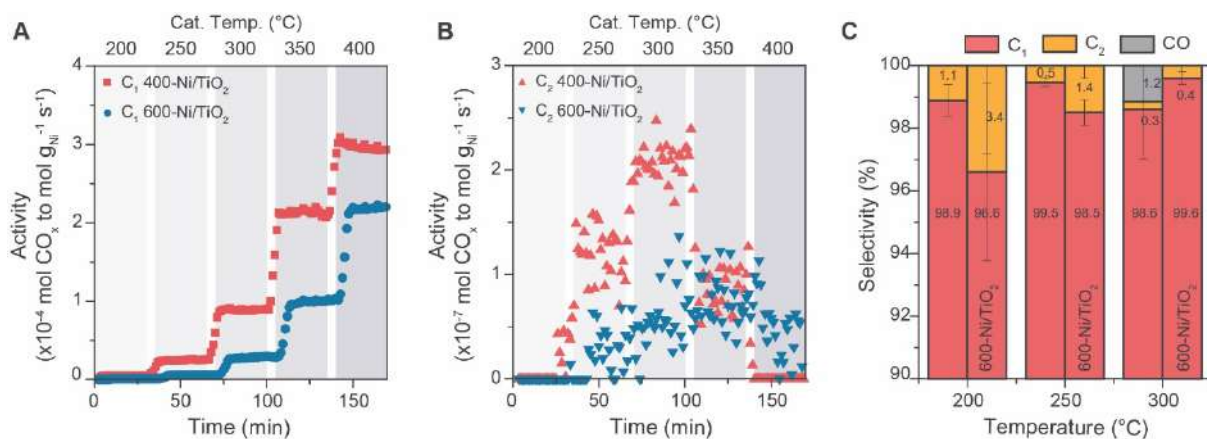
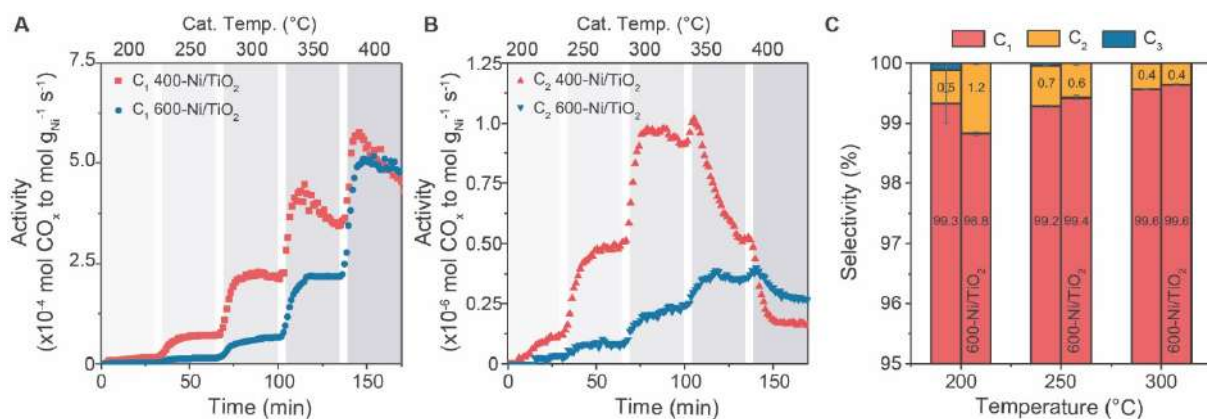


Fig. S35. Ex-situ STEM characterization of 400-Ni/TiO<sub>2</sub> (A,B) and 600-Ni/TiO<sub>2</sub> (C,D) after CO<sub>2</sub> hydrogenation (Conditions: CO<sub>2</sub>:H<sub>2</sub>:He = 1:4:5, 5 bar, GHSV = 80,000 h<sup>-1</sup>).



**Fig. S36.** Reduction temperature effect on catalyst performance: catalytic activity (A, B) and selectivity (C) to hydrocarbons in the  $\text{CO}_2$  hydrogenation reaction over Ni (6 wt.%) /  $\text{TiO}_2$  reduced at 400 °C and 600 °C (Conditions:  $\text{CO}_2:\text{H}_2:\text{He} = 1:4:5$ , 1 bar,  $\text{GHSV} = 80,000 \text{ h}^{-1}$ ).



**Fig. S37.** Reduction temperature effect on catalyst performance: catalytic activity (A, B) and selectivity (C) to hydrocarbons in the  $\text{CO}_2$  hydrogenation reaction over Ni (6 wt.%) /  $\text{TiO}_2$  reduced at 400 °C and 600 °C (Conditions:  $\text{CO}_2:\text{H}_2:\text{He} = 1:4:5$ , 5 bar,  $\text{GHSV} = 80,000 \text{ h}^{-1}$ ).

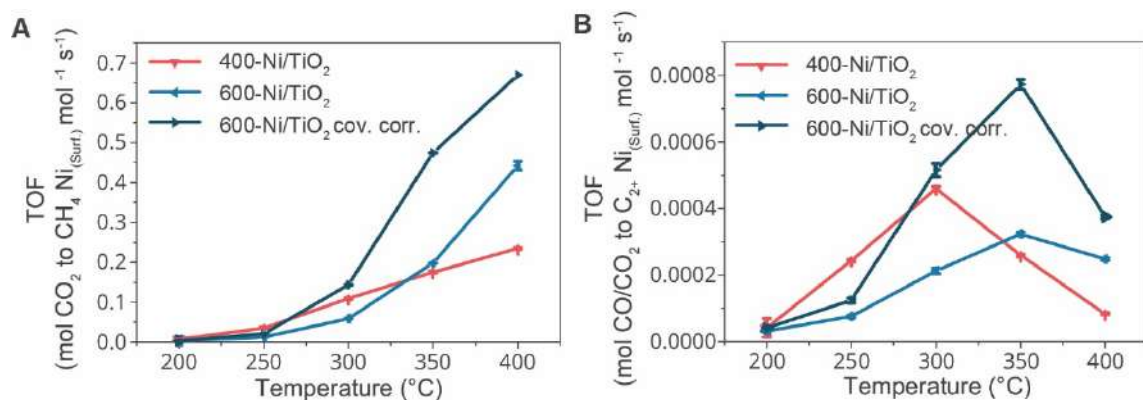


**Fig. S38.** Turnover Frequency (TOF) of the  $\text{CO}_2$  hydrogenation reaction over Ni (6 wt.%) /  $\text{TiO}_2$  to hydrocarbons reduced at 400 °C and 600 °C (Conditions:  $\text{CO}_2:\text{H}_2:\text{He} = 1:4:5$ , 5 bar,  $\text{GHSV} = 80,000 \text{ h}^{-1}$ ).



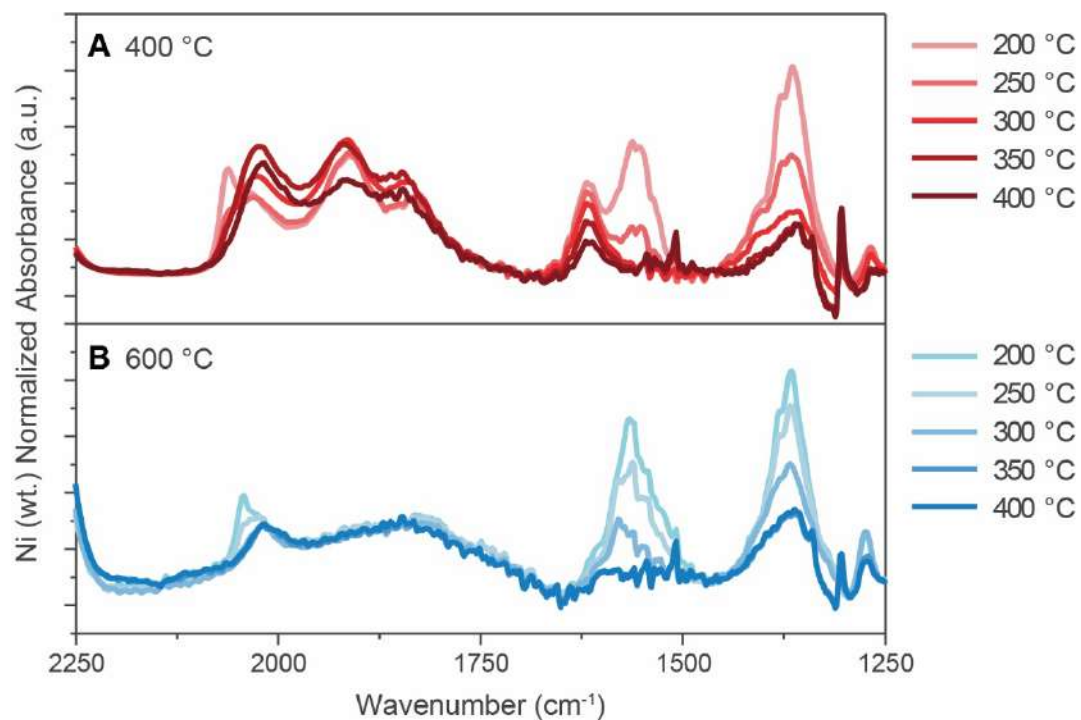


**Fig. S39.** Difference operando FT-IR spectra collected at 200–400 °C under CO<sub>2</sub> hydrogenation conditions (CO<sub>2</sub>:H<sub>2</sub>:He= 1:4:5, 1 bar, GHSV = 80,000 h<sup>-1</sup>) over Ni (6 wt.)/TiO<sub>2</sub> reduced at 400 °C (A) and 600 °C (B).

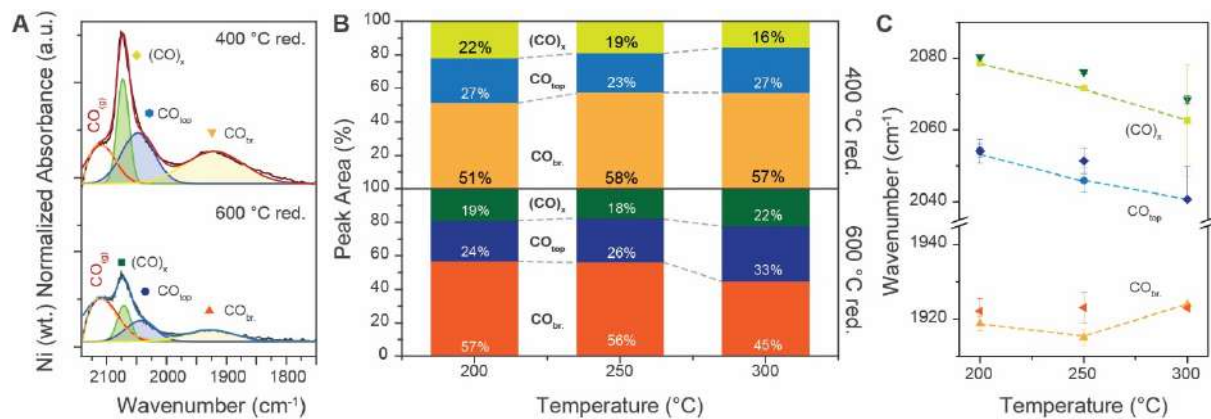


**Fig. S40.** (A) Example of fitting of the CO region (at 200 °C) to get signal contributions from different CO<sub>ads</sub> species from operando FT-IR spectra collected at 200–300 °C under CO<sub>x</sub> hydrogenation conditions (CO<sub>2</sub>:CO:H<sub>2</sub>:He = 3:1:7:16, 5 bar, GHSV = 80,000 h<sup>-1</sup>) over Ni (6 wt.)/TiO<sub>2</sub> reduced at 400 °C and 600 °C (see text for details). (B) Integrated signal of subcarbonyl ((CO)<sub>x</sub>), on-top adsorbed CO (CO<sub>top</sub>) and bridge-adsorbed CO (CO<sub>br</sub>) on Ni, with (C) respective position of maximum absorption, as a function of temperature. Trend lines are added as a guide to the eye.

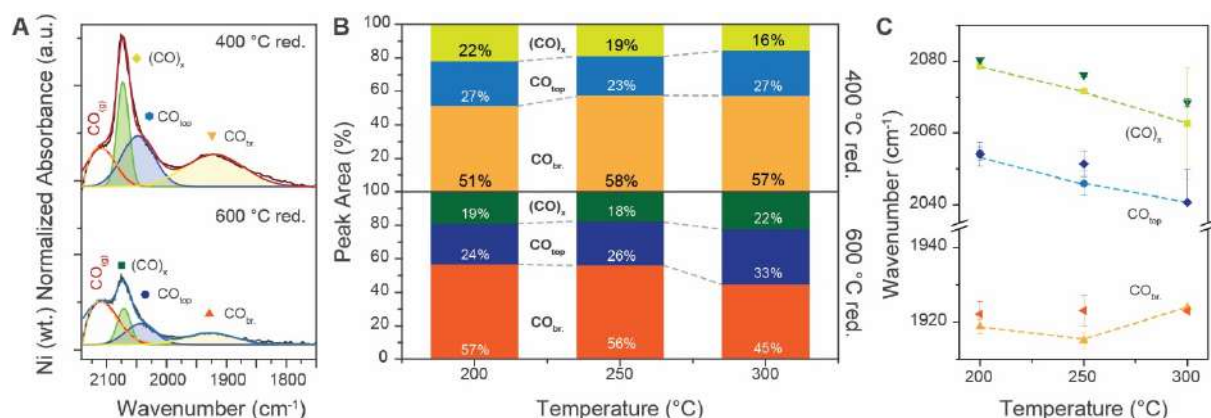


Fig. S40A shows a magnification of the CO region under CO–CO<sub>2</sub> hydrogenation conditions at 200 °C for the two catalyst materials studied, fitted using 4 Gaussians (CO<sub>(g)</sub>, (CO)<sub>x</sub>, CO<sub>top</sub> and CO<sub>br</sub>), whose relative areas and maximum positions are shown as a function of temperature in

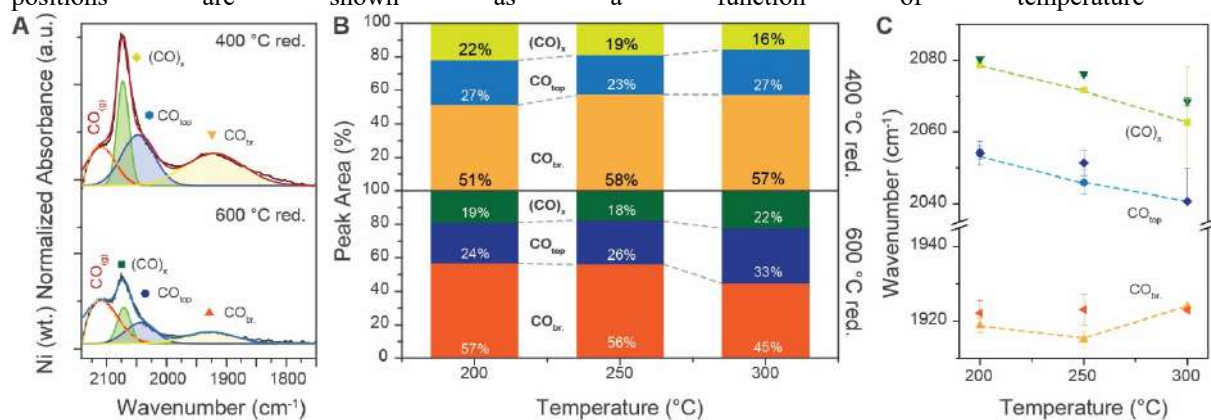


Fig. S40B, respectively. It can be observed that CO<sub>br</sub> species are the minority component over 600 °C reduced Ni/TiO<sub>2</sub>, conversely to what is expected for larger Ni NPs, and consistently with the presence of a TiO<sub>2-x</sub> overlayer. On the other hand, the relative area of the CO<sub>br</sub> species over 400 °C reduced samples grows as a function of temperature to become the majority species. In accordance with subcarbonyl species stability (69), the peak area of the subcarbonyl species (CO)<sub>x</sub> decreases with temperature over both catalyst materials, so that at higher temperatures only the CO<sub>top</sub> contribution remains at higher wavenumbers. Notably, the position of peak maxima for all species over the 400 °C and 600 °C reduced catalysts are comparable (within the fit error) for all temperatures, except for 200 °C, in which a shift of 10 cm<sup>-1</sup> towards higher wavenumber is observed after high reduction temperature (

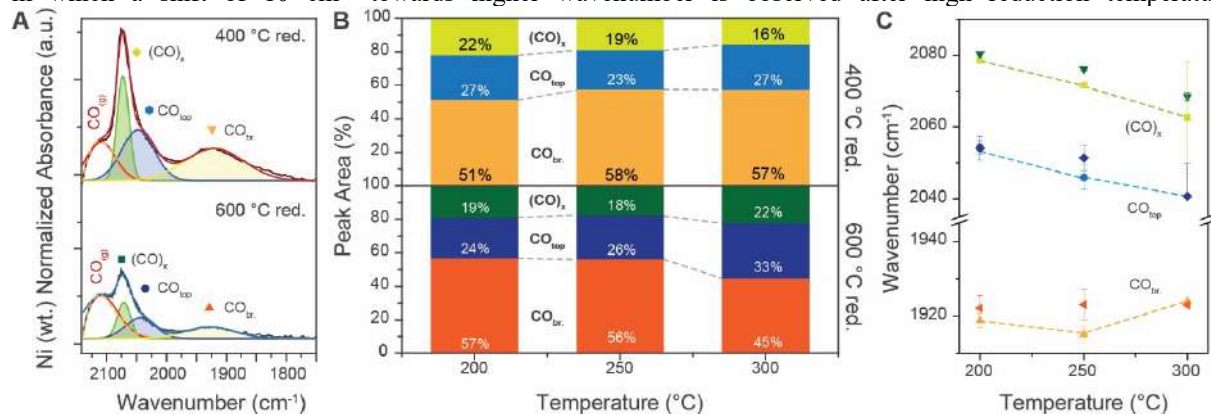


Fig. S40C). Such a shift can be explained by a lower dipole–dipole interaction between CO adsorbates (70), consistent with higher adsorbate–adsorbate distance induced by Ni coverage by a patchy TiO<sub>2-x</sub> overlayer.

After restructuring, the residual TiO<sub>x</sub> coverage is shown to reduce the extent to which Ni can react with CO to form unwanted Ni (sub)carbonyl (Fig. S40). Hernández Mejía et al. recently proposed two explanations for less nickel tetracarbonyl formation on Ni/Nb<sub>2</sub>O<sub>5</sub> due to SMSI (31): (i) physical blockage by suboxides of exposed low-coordinated nickel atoms, and/or (ii) destabilization of Ni–CO bond by electronic backdonation to the CO 2π\* orbital,

avored by electron transfer from the suboxides to Ni. The second hypothesis would result in a shift towards lower wavenumbers of the maximum of adsorbed CO signals with SMSI. We show that, instead, the wavenumber of all adsorbed CO species is comparable for both samples at all reaction temperatures (

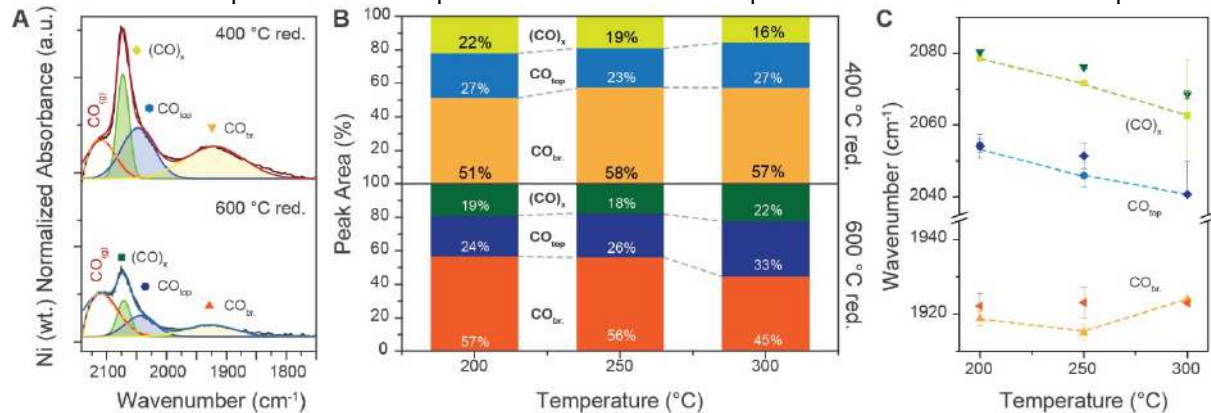
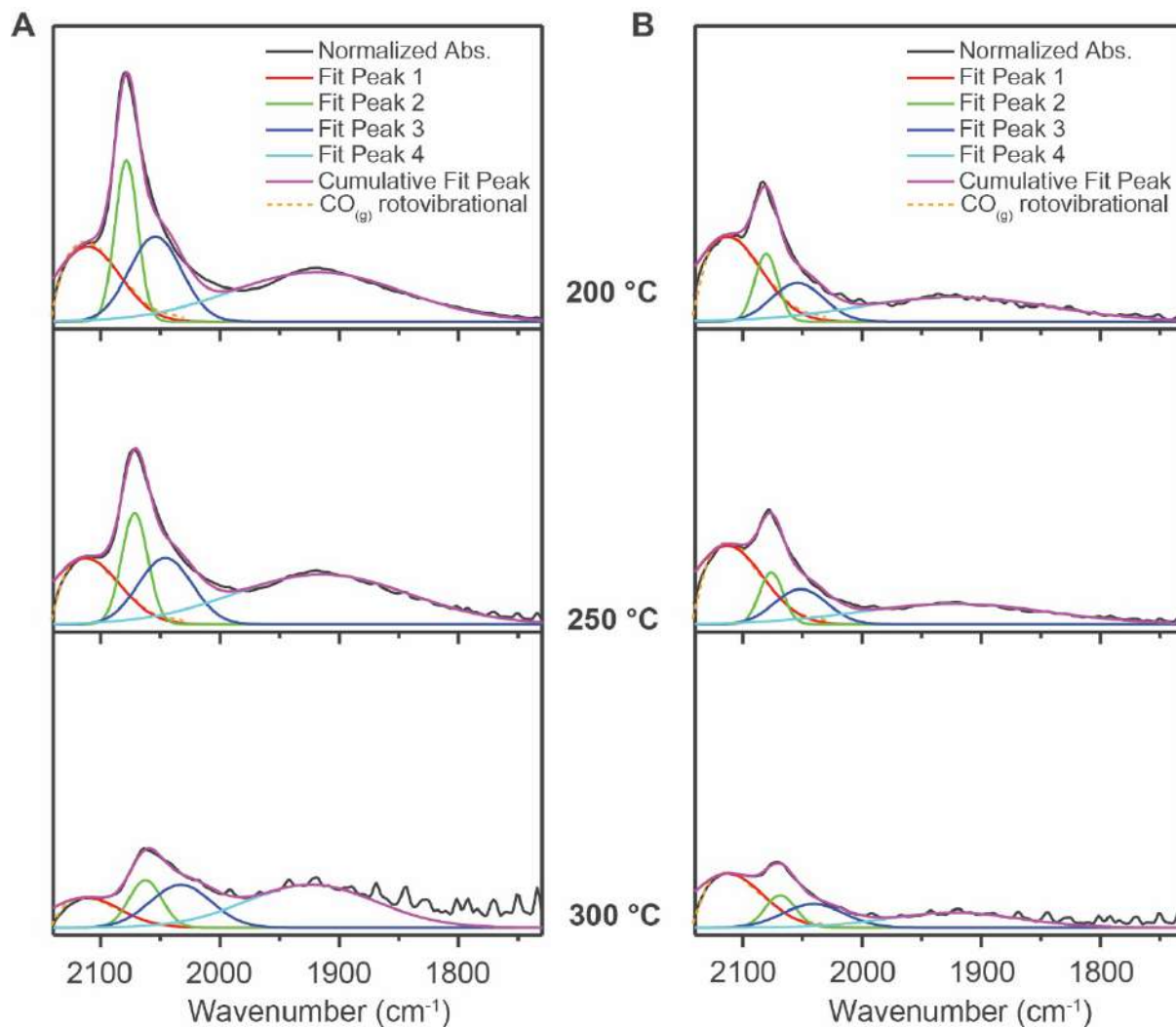


Fig. S40C), which strongly suggests that physical blockage is the reason for less Ni(CO)<sub>4</sub> formation by SMSI, at least over Ni/TiO<sub>2</sub> catalyst materials under the studied conditions.



**Fig. S41. Fitted CO region of the operando FT-IR spectra collected at 200–300 °C under CO<sub>x</sub> hydrogenation conditions (CO<sub>2</sub>:CO:H<sub>2</sub>:He = 3:1:7:16, 5 bar, GHSV = 80,000 h<sup>-1</sup>) over Ni (6 wt.%) /TiO<sub>2</sub> reduced at 400 °C (A) and 600 °C (B), showing Ni availability on both catalysts. See below for details of the fitting procedure.**

To fit the contributions of adsorbed CO species (1800–2100 cm<sup>-1</sup>), it is crucial to first correctly describe the contribution of the CO<sub>(g)</sub> signal which overlaps the same region. To this end, the signal for pure gaseous CO (dashed orange line) was obtained from the NIST database (<https://webbook.nist.gov/>) and scaled to the maximum observed at 2111 cm<sup>-1</sup>. Note that the dashed orange line nicely follows the observed spectrum on the left side (dark line). A Gaussian function (red line) was then used to fit the left part of the CO<sub>(g)</sub> curve, since this is the part that can affect the adsorbed CO contributions. Note that the fitting above a value of 2111 cm<sup>-1</sup> is not optimal, but does not influence the fitting of the targeted spectral contributions.

Once the gaseous CO fit was optimized, its parameters were fixed, and the rest of the contributions were fitted by three Gaussians.<sup>(71)</sup> Notably, using pseudo Voigt functions gave back almost pure Gaussians (but lead to divergent results in some cases), further supporting the validity of the Gaussian fitting method in the present case.

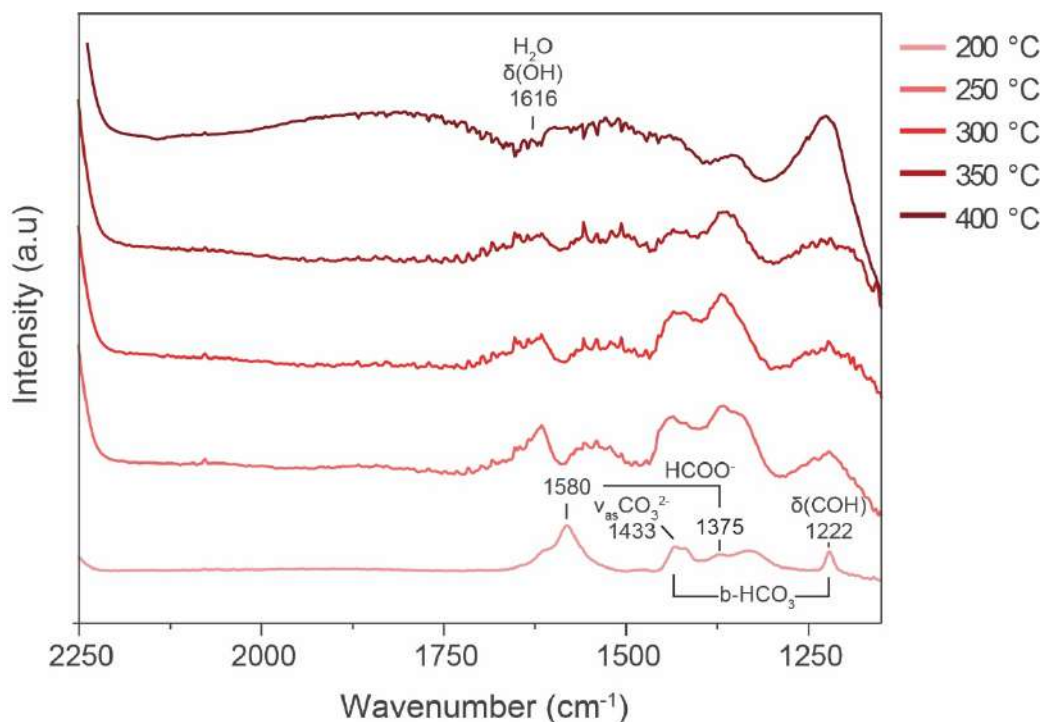


**Fig. S42. Difference operando FT-IR spectra during CO<sub>2</sub> hydrogenation over pure TiO<sub>2</sub> (P25, Degussa without Ni) (CO<sub>2</sub>:H<sub>2</sub>:He= 3:4:5, 1 bar, GHSV = 80,000 h<sup>-1</sup>). Formate, carbonate and hydrogen carbonate species were assigned baseCOD on (72).**

#### Ni surface area calculations based on operando FT-IR spectroscopy data

To calculate the relative amount of active sites on the Ni surface under reaction conditions after reduction at 600 °C compared to 400 °C due to TiO<sub>2-x</sub> coverage, we have compared the areas of the adsorbed CO species after normalization by Ni weight for one of the Ni/TiO<sub>2</sub> samples used in this study. This is based on the assumption that the quantity of exposed Ni sites correlates with the number of adsorbed CO species with a certain stoichiometry, and that the extinction coefficients are comparable for a given species on the samples reduced at two different temperatures. The ratio (*r*) of surface sites on 400 °C and 600 °C samples was then derived as the ratio of the following:

- Method 1 (M1): the area of integrated CO<sub>top</sub> (2104–1977 cm<sup>-1</sup>) and CO<sub>bridged</sub> (1977–1755 cm<sup>-1</sup>) regions of the operando FT-IR spectra (M1, Table S7).
- Method 2 (M2): the sum of the areas of the CO<sub>x</sub>, CO<sub>top</sub> and CO<sub>bridge</sub> components from the fitted operando FT-IR spectra (see Fig. S41). This method removes the area due to peaks from the rotovibrational spectrum of water.
- Method 3 (M3): the *weighed* sum of the areas of the CO<sub>x</sub>, CO<sub>top</sub> and CO<sub>bridge</sub> components from the fitted operando FT-IR spectra (see Fig. S41), with 1/3, 1 and 2 as weighing factors accounting for the Ni:CO stoichiometry of the different species.

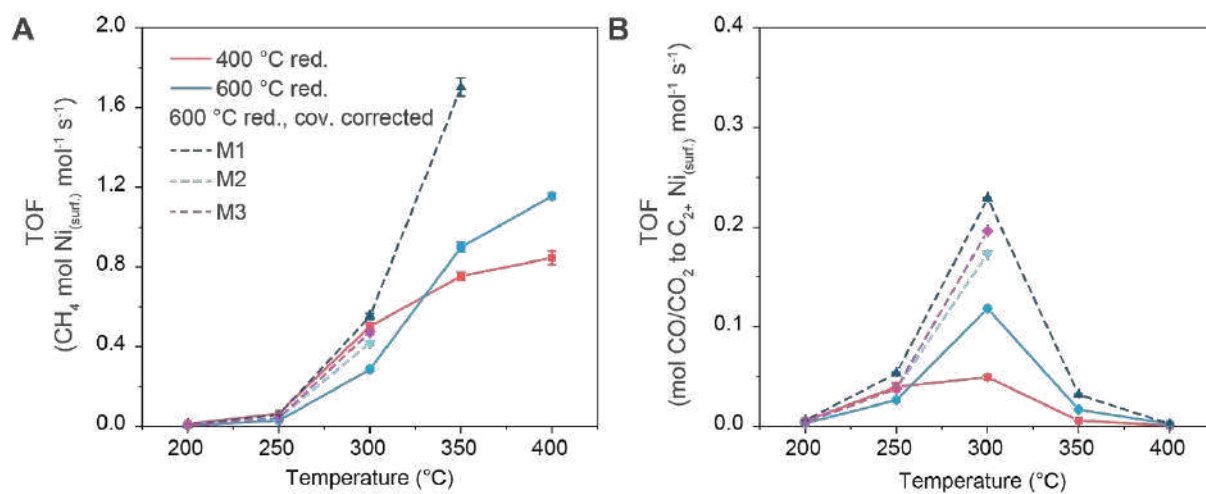
The coverage was then calculated taking the difference in size of the nanoparticles into consideration:

$$Relative\ coverage\ (\%) = \left( 1 - \frac{r}{\frac{Ni\ size_{400^\circ C}}{Ni\ size_{600^\circ C}}} \right) \times 100 = \left( 1 - \frac{r}{\frac{7.9}{12.0}} \right) \times 100$$

Finally, the TOF<sub>rel. cov.</sub>, i.e., corrected for the relative coverage, was calculated as:

$$TOF_{rel. cov.} = TOF / Ni_{fraction\ exposed} = TOF / \left( \frac{r}{\frac{7.9}{12.0}} \right)$$

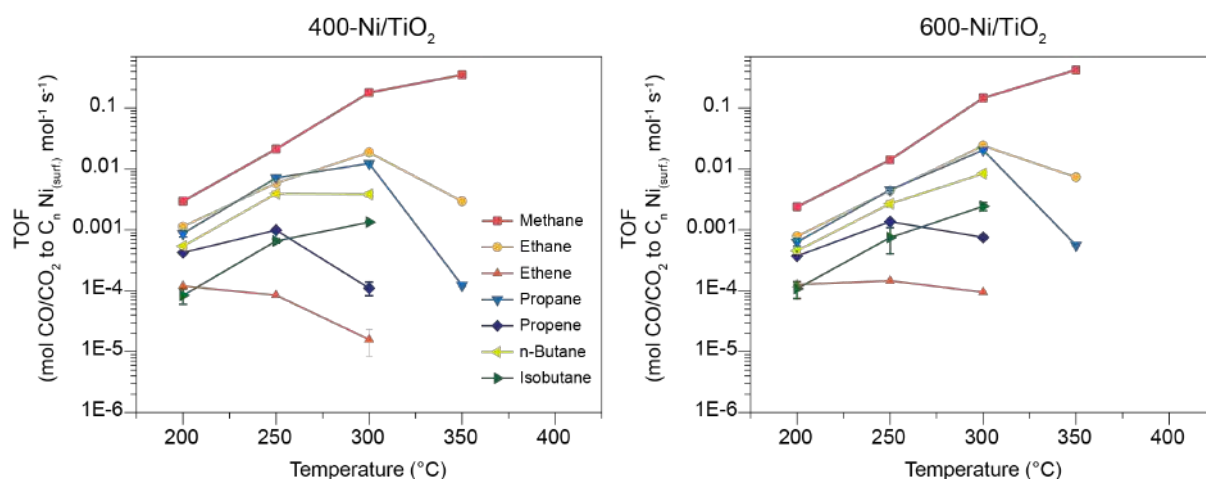
The TOF<sub>rel. cov.</sub> Curves plotted in Fig. 3F, G are based on the assumption giving the lowest values, i.e, a lower bound of TOF enhancement. A summary of the TOF<sub>rel. cov.</sub> curves is reported in Fig. S43.



**Fig. S43.** Turnover Frequency (TOF) for (A) methane production and (B) C–C coupling products under  $\text{CO}_x$  hydrogenation conditions ( $\text{CO}_2:\text{CO}:\text{H}_2:\text{He} = 3:1:7:16$ , 5 bar,  $\text{GHSV} = 80,000 \text{ h}^{-1}$ ) over Ni (6 wt.%) $\text{TiO}_2$  after reduction at 400  $^{\circ}\text{C}$  (red) and 600  $^{\circ}\text{C}$  (light blue). The dashed lines show the TOF corrected for the ratio of exposed Ni surface in the 600  $^{\circ}\text{C}$  vs. 400  $^{\circ}\text{C}$  reduced catalysts calculated by the three methods described in the text (M = method).

**Table S7. Ni coverage for the 600 °C reduced sample, calculated based on the three methods, and the average of the three methods.**

Temperature (°C)	Sites ratio M1	Coverage M1	Sites ratio M2	Coverage M2	Sites ratio M3	Coverage M3	Average Coverage
200	0.33	50%	0.50	24%	0.52	20%	32%
250	0.33	50%	0.46	30%	0.46	30%	37%
300	0.34	48%	0.45	32%	0.40	40%	40%
350	0.35	47%					

**Fig. S44. Turnover Frequency (TOF) for all observed reaction products under CO<sub>x</sub> hydrogenation conditions (CO<sub>2</sub>:CO:H<sub>2</sub> = 3:1:7:16, 5 bar, GHSV = 80,000 h<sup>-1</sup>) over Ni (6 wt.%) /TiO<sub>2</sub> after reduction at 400 °C (left) and 600 °C (right), based on metal nanoparticles dimensions, as calculated from Scanning Transmission Electron Microscopy High-Angle Annular Dark-Field (STEM-HAADF) analysis.**

**Table S8: Carbon mass balance under CO–CO<sub>2</sub> hydrogenation conditions (CO:CO<sub>2</sub>:H<sub>2</sub>:He = 1:3:7:9, 5 bar, GHSV = 80,000 h<sup>-1</sup>) over Ni (6 wt.%)/TiO<sub>2</sub>.**

Catalyst Temperature (°C)	C balance over Ni/TiO <sub>2</sub> reduced at 400 °C (%)	C balance over Ni/TiO <sub>2</sub> reduced at 600 °C (%)
200	85.2	84.3
250	94.3	90.6
300	96.4	89.9
350	100.0	94.9
400	105.7	103.2



**Table S9. Thermodynamically predicted partial pressure of gaseous Ni(CO)<sub>4</sub> under the investigated CO–CO<sub>2</sub> hydrogenation conditions (CO<sub>2</sub>:CO:H<sub>2</sub> = 3:1:7, 4 bar) as a function of temperature.**

Equilibrium calculations were performed using the HSC Chemistry 9.1 software in the *Gem equilibrium composition* module, by the Gibbs free energy minimization method. Notably, despite the fact that traces of gaseous Ni(CO)<sub>4</sub> are expected to form (and possibly lead to nanoparticles growth by Ostwald ripening), they could not be observed by FT-IR spectroscopy due to the low concentration predicted by thermodynamic calculations.

<b>Reaction temperature (°C)</b>	<b>Partial pressure of Ni(CO)<sub>4</sub>(g) (bar)</b>
200	1.47E-27
210	4.35E-27
220	1.23E-26
230	3.30E-26
240	8.51E-26
250	2.11E-25
260	5.05E-25
270	1.17E-24
280	2.62E-24
290	5.70E-24
300	1.21E-23
310	2.49E-23
320	5.01E-23
330	9.86E-23
340	1.90E-22
350	3.58E-22
360	6.62E-22
370	1.20E-21
380	2.15E-21
390	3.76E-21
400	6.49E-21

### Reproducibility of catalytic testing results

The following figures show repeated catalytic experiments with a different batch of 6 wt.% Ni/TiO<sub>2</sub> catalyst to ensure that the reported catalytic testing results can be considered as sufficiently reproducible. The slight difference observed with respect to the catalyst of the main text is due to some small differences in the metal nanoparticle sizes as well as the experimental settings used, but the overall results present a similar trend both in terms of particle size and catalytic performance.

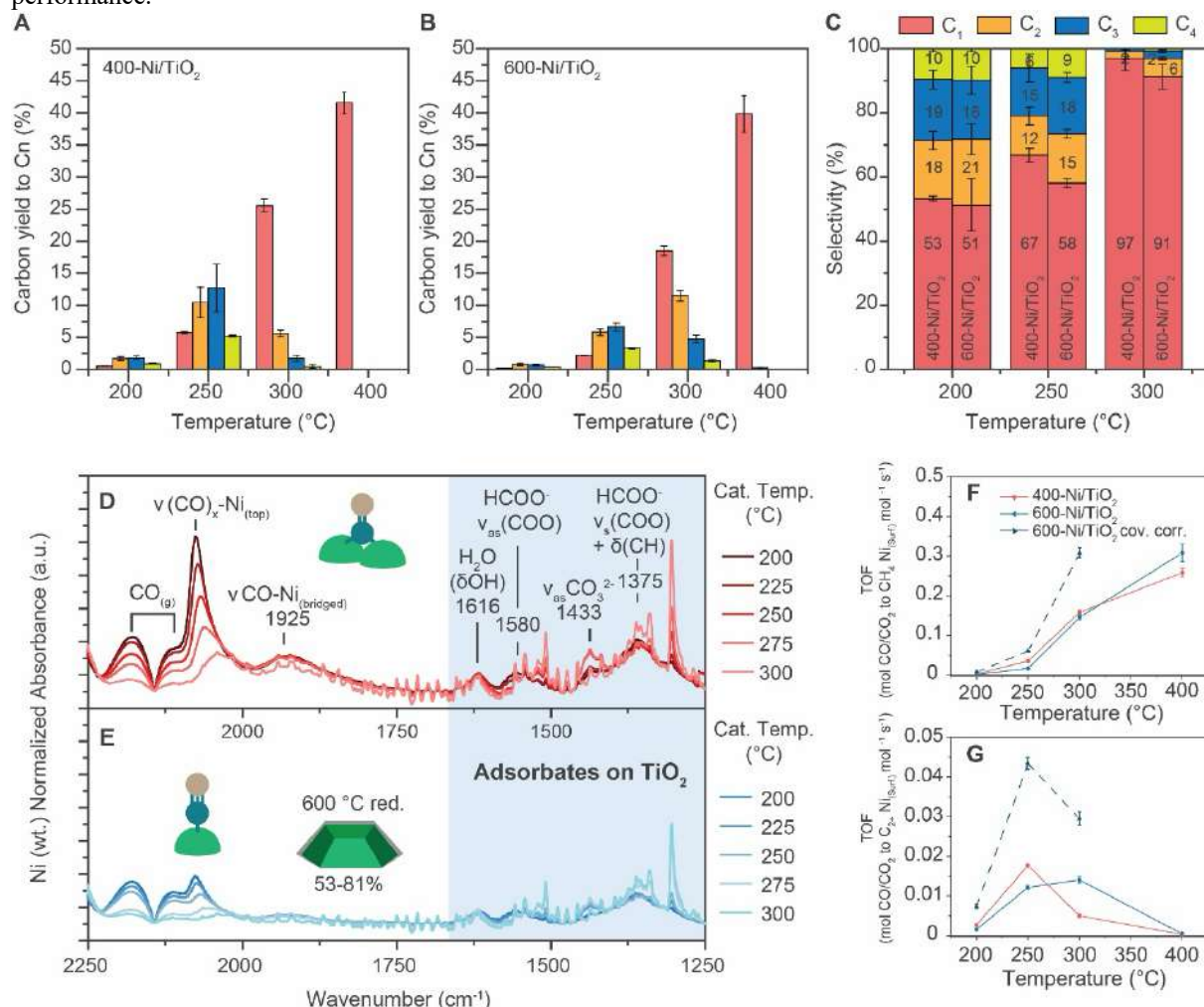


**Fig. S45.** Carbon yield of 400-Ni/TiO<sub>2</sub> (A) and 600-Ni/TiO<sub>2</sub> (B) for CO/CO<sub>2</sub> hydrogenation (light shade). (C) Selectivity to hydrocarbons in the CO/CO<sub>2</sub> hydrogenation reaction over 400-Ni/TiO<sub>2</sub> and 600-Ni/TiO<sub>2</sub>. (D and E) Operando FT-IR spectra collected at 200° to 300 °C under CO–CO<sub>2</sub> hydrogenation conditions over (D) 400-Ni/TiO<sub>2</sub> and (E) 600-Ni/TiO<sub>2</sub>, showing Ni exposure in both catalyst materials. The estimate for Ni coverage for 600-Ni/TiO<sub>2</sub> and the majority CO<sub>ads</sub> species at 300 °C is schematically depicted for the two catalysts. (F,G) Turnover frequency (TOF) for (F) methane production and (G) C–C coupling products over 400-Ni/TiO<sub>2</sub> (red) and 600-Ni/TiO<sub>2</sub> (light blue). The dashed dark blue line shows the TOF corrected for the most conservative estimate of exposed Ni surface in 600-Ni/TiO<sub>2</sub>. Conditions for CO/CO<sub>2</sub> methanation: CO<sub>2</sub>:CO:H<sub>2</sub>:He = 3:1:7:16, total flow = 27 mL/min, 5 bar, GHSV = 80,000 h<sup>-1</sup>.

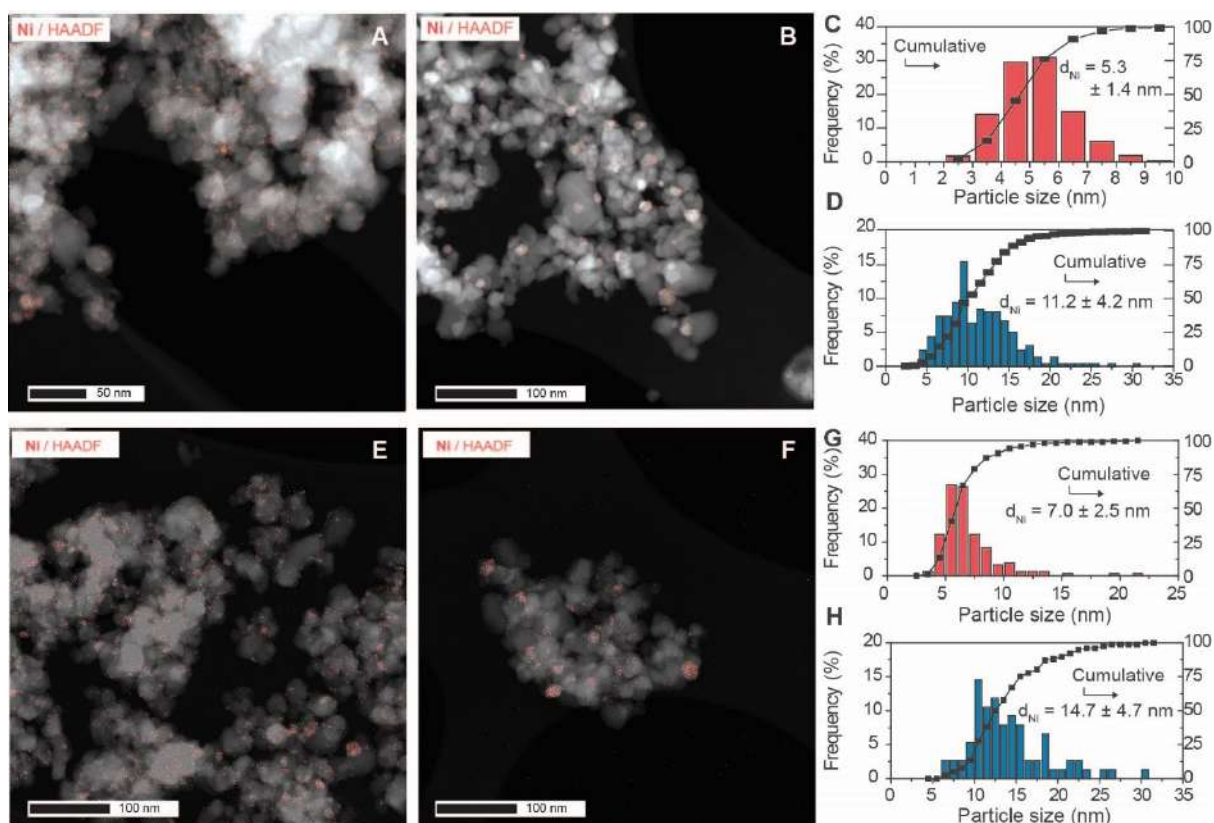


**Fig. S46.** Ex-situ STEM characterization of 400-Ni/TiO<sub>2</sub> (A, C) and 600-Ni/TiO<sub>2</sub> (B, D) after ex-situ reduction (Conditions: H<sub>2</sub>:He = 1:1, 1 bar) and of 400-Ni/TiO<sub>2</sub> (E, G) and 600-Ni/TiO<sub>2</sub> (F, H) after CO/CO<sub>2</sub> hydrogenation: CO<sub>2</sub>:CO:H<sub>2</sub>:He = 3:1:7:16, total flow = 27 mL/min, 5 bar, GHSV = 80,000 h<sup>-1</sup>.

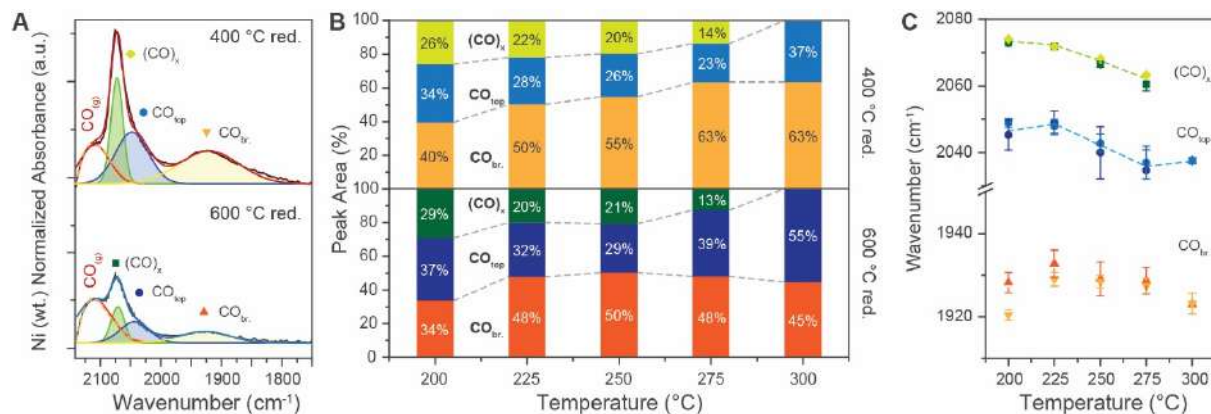


**Fig. S47.** (A) Example of fitting of the CO region (at 200 °C) to get signal contributions from different CO<sub>ads.</sub> species (see SI for details). (B) Integrated signal of subcarbonyl ((CO)<sub>x</sub>), on-top adsorbed CO (CO<sub>top</sub>), and bridge-adsorbed CO (CO<sub>br</sub>) on Ni during CO/CO<sub>2</sub> hydrogenation (CO<sub>2</sub>:CO:H<sub>2</sub>:He = 3:1:7:16, 5 bar, GHSV = 80,000 h<sup>-1</sup>), with (C) respective position of maximum absorption, as a function of temperature. Trend lines are added as guide to the eye.

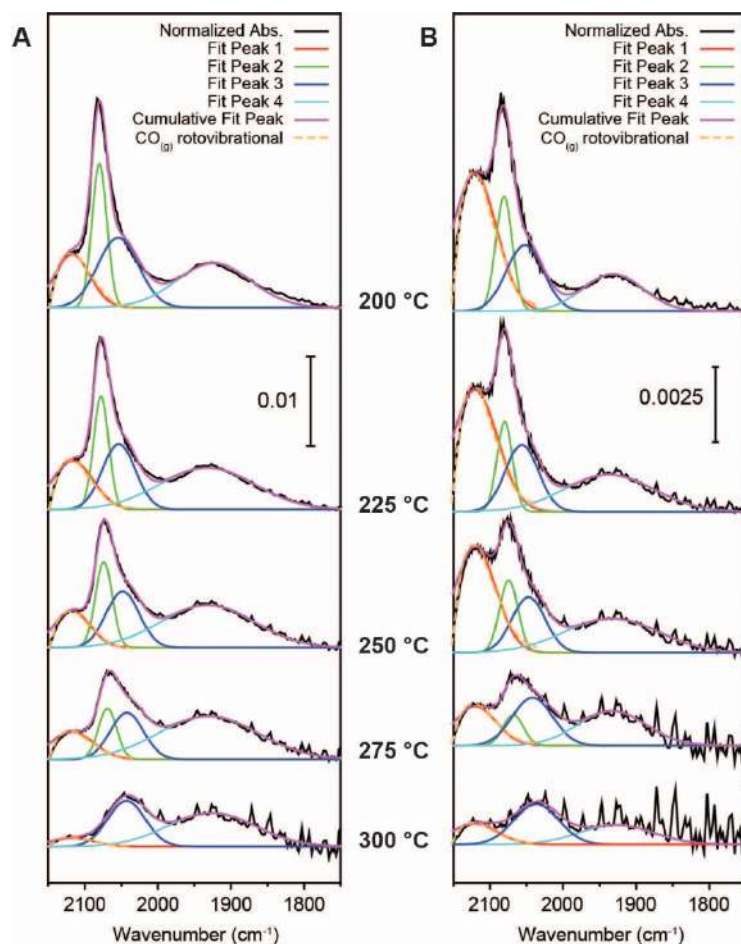


**Fig. S48.** Fitted CO region of the operando FT-IR spectra collected at 200–300 °C under CO<sub>x</sub> hydrogenation conditions (CO<sub>2</sub>:CO:H<sub>2</sub>:He = 3:1:7:16, 5 bar, GHSV = 80,000 h<sup>-1</sup>) over Ni (6 wt.%)/TiO<sub>2</sub> reduced at 400 °C (A) and 600 °C (B), showing Ni availability on both catalysts.

**Table S10:** Carbon mass balance under CO–CO<sub>2</sub> hydrogenation conditions (CO:CO<sub>2</sub>:H<sub>2</sub>:He = 1:3:7:16, 5 bar, GHSV = 80,000 h<sup>-1</sup>) over Ni (6 wt.%)/TiO<sub>2</sub>.

Catalyst Temperature (°C)	C balance over Ni/TiO <sub>2</sub> reduced at 400 °C (%)	C balance over Ni/TiO <sub>2</sub> reduced at 600 °C (%)
200	88.1	93.7
250	99.9	96.5
300	99.9	100.0
400	100.5	98.2

The carbon balance was higher than 95% in all cases, except at 200 °C, at which the carbon balance for the 400 °C reduced catalysts was 88 %, suggesting favored C deposition due to the Boudouard reaction.

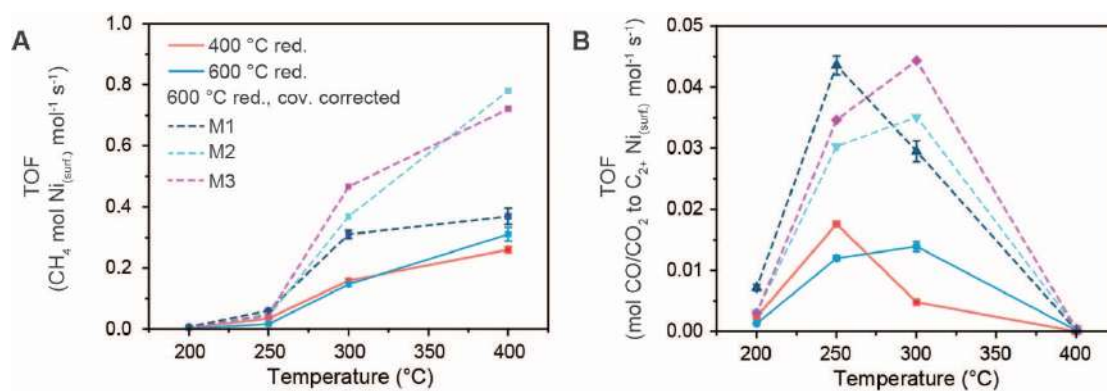


**Fig. S49:** Turnover Frequency (TOF) for (A) methane production and (B) C–C coupling products under CO<sub>x</sub> hydrogenation conditions (CO<sub>2</sub>:CO:H<sub>2</sub>:He = 3:1:7:16, 5 bar, GHSV = 80,000 h<sup>-1</sup>) over Ni (6 wt.%)/TiO<sub>2</sub> after reduction at 400 °C (red) and 600 °C (light blue). The dashed lines shows the TOF corrected for the ratio of exposed Ni surface in the 600 °C vs. 400 °C reduced catalysts calculated by the three methods described in the text (M = method).

**Table S11:** Ni coverage for the 600 °C reduced sample, calculated based on the three methods, and the average of the three methods.

Temperature (°C)	Sites ratio M1	Coverage M1	Sites ratio M2	Coverage M2	Sites ratio M3	Coverage M3	Average Coverage
200	0.11	81%	0.23	61%	0.22	64%	69%
250	0.17	72%	0.26	57%	0.25	66%	66%
300	0.29	53%	0.21	66%	0.18	69%	63%
400	0.51	16%	0.24	56%	0.26	57%	43%

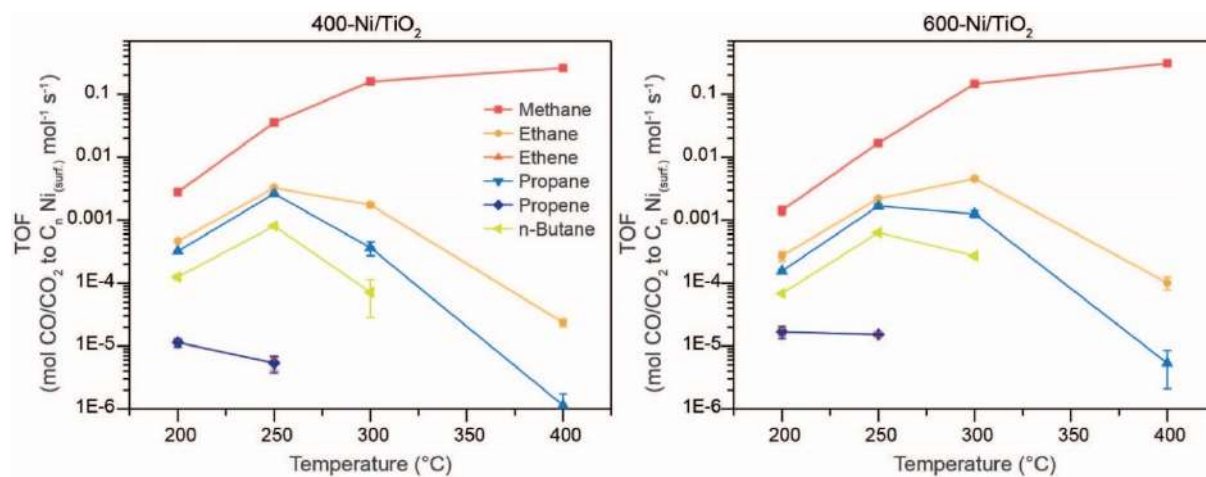


Fig. S50. Turnover Frequency (TOF) for all observed products under CO<sub>x</sub> hydrogenation conditions (CO<sub>2</sub>:CO:H<sub>2</sub>:He = 3:1:16, 5 bar, GHSV = 80,000 h<sup>-1</sup>) over Ni (6 wt.%)/TiO<sub>2</sub> after reduction at 400 °C (left) and 600 °C (right), based on nanoparticles dimensions calculated from Scanning Transmission Electron Microscopy High-Angle Annular Dark-Field (STEM-HAADF) analysis.